

# Electromagnetic Field Controlled Domain Wall Displacement for Induced Strain Tailoring in Batio<sub>3</sub>-Epoxy Nanocomposite: Development of A Contact-Less Active Toughening Mechanism

**Danning Li**

Cranfield University

**James Barrington**

Cranfield University

**Stephen James**

Cranfield University

**David Ayre**

Cranfield University

**Marcin Sloma**

Warsaw University of Technology

**Meng-Fang Lin**

Ming Chi University of Technology

**Hamed Yazdani Nezhad** (✉ [hamed.yazdani@city.ac.uk](mailto:hamed.yazdani@city.ac.uk))

City, University of London

---

## Research Article

**Keywords:** Dielectric nanocomposites, active toughening, Ferroelectrics, Barium titanate, Domain wall movement, Extrinsic strain, Microwave radiation

**Posted Date:** January 3rd, 2022

**DOI:** <https://doi.org/10.21203/rs.3.rs-1214694/v1>

**License:**  This work is licensed under a Creative Commons Attribution 4.0 International License.

[Read Full License](#)

---

# Electromagnetic Field Controlled Domain Wall Displacement for Induced Strain Tailoring in BaTiO<sub>3</sub>-Epoxy Nanocomposite: development of a contact-less active toughening mechanism

Danning Li<sup>1,\*</sup>, James Barrington<sup>2</sup>, Stephen James<sup>2</sup>, David Ayre<sup>1</sup>, Marcin Sloma<sup>3</sup>, Meng-Fang Lin<sup>4</sup>, Hamed Yazdani Nezhad<sup>1,5,\*</sup>

<sup>1</sup>Enhanced Composites and Structures Centre, School of Aerospace, Transport and Manufacturing, Cranfield University, Cranfield, UK

<sup>2</sup>Centre for Engineering Photonics, School of Aerospace, Transport and Manufacturing, Cranfield University, Cranfield, UK

<sup>3</sup>Faculty of Mechatronics, Warsaw University of Technology, Warsaw, Poland

<sup>4</sup>Department of Materials Engineering, Ming Chi University of Science and Technology, New Taipei, Taiwan

<sup>5</sup>Aeronautics and Aerospace Research Centre, Department of Mechanical Engineering and Aeronautics, City, University of London, London, UK

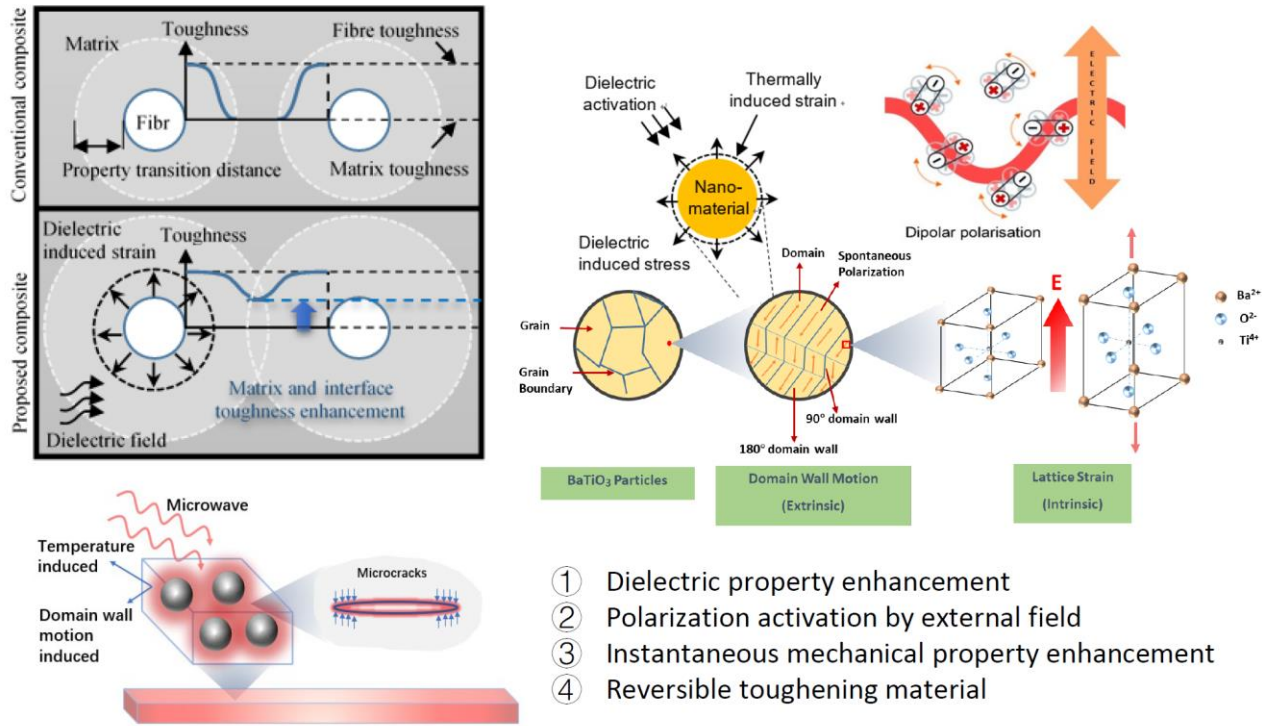
*\*Corresponding authors: danning.li@cranfield.ac.uk and hamed.yazdani@city.ac.uk*

## ABSTRACT

Failure in an epoxy polymer composite material is prone to initiate by the coalescence of microcracks in its polymer matrix. As such, matrix toughening via addition of a second phase as rigid or/and rubber nano/micro-particles is one of the most popular approaches to improve the fracture toughness across multiple scales in a polymer composite, which dissipates fracture energy via deformation mechanisms and microcracks arrest. Few studies have focused on tailorable and variable toughening, so-called 'active toughening', mainly suggesting thermally induced strains which offer slow and irreversible toughening due to polymer's poor thermal conductivity. The research presented in the current article has developed an instantaneous, reversible active toughening composite based upon contact-less introduction of a microscopic compressive extrinsic strain field via remote electromagnetic radiation. Quantification of the extrinsic strain evolving in the composite with the microwave energy has been conducted using in-situ real-time fibre optic sensing. A theoretical constitutive equation correlating the exposure energy to micro-strains has been developed, with its solution validating the experimental data and describing their underlying physics. The research has utilised functionalised dielectric ferroelectric nanomaterials, barium titanate (BaTiO<sub>3</sub>), as a second phase dispersed in an epoxy matrix, able to introduce microscopic electro-strains to their surrounding rigid epoxy subjected to an external electric field (microwaves, herein), as result of their domain walls dipole displacements. Epoxy Araldite LY1564, a diglycidyl ether of bisphenol A (DGEBA) associated with the curing agent Aradur 3487 were embedded with the BaTiO<sub>3</sub> nanoparticles. The silane coupling agent for the nanoparticles' surface functionalisation was 3-glycidoxypropyl trimethoxysilane (3-GPS). Hydrogen peroxide (H<sub>2</sub>O<sub>2</sub>, 30%) and acetic acid (C<sub>2</sub>H<sub>4</sub>O<sub>2</sub>, 99.9%) used as functionalisation aids, and the ethanol (C<sub>2</sub>H<sub>6</sub>O, 99.9%) used for BaTiO<sub>3</sub> dispersion. Firstly, the crystal microstructure of the functionalised nanoparticles and the thermal and dielectric properties of the achieved epoxy composite materials have been characterised. It has been observed that the addition of the dielectric nanoparticles has a slight impact on the curing extent of the epoxy. Secondly, the surface-bonded fibre bragg grating (FBG) sensors have been employed to investigate the real-time variation of strain and temperature in the epoxy composites exposed to microwaves at 2.45 GHz and at different exposure energy. The strains developed due to the in-situ exposure at composite, adhesive and their holding fixture material were evaluated using the FBG. The domain wall induced extrinsic strains were distinguished from the thermally induced strains, and found that the increasing exposure energy has an instantaneously increasing effect on the development of compressive strains. Post-exposure Raman spectra showed no residual field in the composite indicating no remnant strain field examined under microwave powers < 1000 W, thus suggesting a reversible strain introduction mechanism, i.e. the composite retaining its nominal properties post exposure. The dielectric composite development and quantifications presented in this article proposes a novel active toughening technology for high-performance composite applications in numerous sectors.

**Keywords:** Dielectric nanocomposites; active toughening; Ferroelectrics; Barium titanate; Domain wall movement; Extrinsic strain; Microwave radiation.

## Graphical Illustration of The Research Presented in Article



## 1 INTRODUCTION

Among their high-performance engineering applications, fibre-reinforced polymer (FRP) composite materials have extensively been used with advantages of high specific strength and modulus, facile fabrication, considerable thermal resistance, and economic efficiency [1]. High-performance FRP composites have two major damage initiation modes when exposed to dynamic events; intra-laminar damage (e.g., matrix cracking, fibre fracture and fibre-matrix debonding) and inter-laminar damage (e.g., delamination). The intra-laminar damage is mainly dominated by matrix, fibre, and fibre-matrix interphase properties. However, it is challenging to tailor the properties of the fibre during composite's fabrication process. Therefore, the most widely adopted approach is matrix toughening owing to the diverse feasibility of its manufacturing. A FRP composite is mainly made of thermoset resins such as epoxy with a highly cross-linked structure to achieve optimal mechanical properties and thermal stability. Despite its advantageous properties, epoxy has its drawbacks of having inherent brittleness that tends to fail at relatively low fracture energy, especially under transversal direction or when subjected to high strain rate or impact loading [2-4]. Alternatively, thermoplastic-based FRPs could hinder microcracks coalesce and growth owing to their relatively higher toughness and semi-crystalline structures in variants such as poly-ether-ether-ketone (PEEK) [5], widely used for engineering applications in the aeronautical and automotive sectors [6], however, exhibiting a softening behaviour under elevated temperatures.

To overcome these property-driven drawbacks, numerous researches have been carried out for property enhancement via modifying epoxy with the inclusion of various micro- and nano-fillers as a second phase, such as rubber tougheners [7], silica particles [8], carbon nanoparticles [9, 10], clay [11] and fibre coating [12]. There are also various methods developed such as inter-penetrating network [13], polymer plasticisation [14], the addition of rubber [15] and/or rigid inorganic particles like glass [16], self-healing [17] and volume dilation [18]. It has been observed that the rubber tougheners are the most effective ones, having substantial increase in the fracture toughness [19] of a brittle epoxy by multiple orders of magnitude, though reduction in strength and stiffness are also observed [20]. An increase in fracture toughness of the glass/epoxy composites up to 82% is achieved by incorporating both core-shell rubber particles and silica nanoparticles [21]. It is also observed by many studies that a threshold exists and above which the particles tend to agglomerate and cause a degradation in mechanical properties [22-25]. The quality of particle/matrix interfacial bonding is another crucial factor that determines the mechanical properties of a

modified epoxy matrix. Thus the application of coupling agents for surface treatment of particles is introduced to achieve a better interfacial bonding between particles and matrix [26]. Despite the excellent performance of particle-toughened epoxy composites, loss in elastic modulus, tensile strength, and glass transition temperature are also reported by other studies [27]. The addition of particles into the epoxy matrix often leads to a higher viscosity, and shear thinning behaviour [28, 29]. Optimal uniform particles dispersion in epoxy resin is also a critical factor that requires to be achieved for a smooth load transfer between epoxy and fillers [28]. Although the modified epoxy with particles exhibits a promising future with excellent toughening performance, microcracks still formed in FRPs when subjected to varying or extreme operating conditions or during the manufacturing [30], indicating an inherent level of uncertainty in the material's response that will require active toughness enhancement across the material. However, the toughness enhancement via second phase inclusion is only performed before service. When the epoxy matrix is exposed to varying mechanical loading during fabrication, storage, and service, microcracks are formed that are extremely difficult to detect and repair due to techniques limitation. Consequently, these internal micro-defects reduce the composite's performance, and their propagation may result in disastrous structural failure. Apart from such 'one-off' and irreversible toughening, a few studies focused on enabling the toughening effect by introducing an internal residual compressive stress field in the epoxy resin as a result of heating, offering 'active' and reversible toughening [31]. Such compression mechanism mainly relies upon the discrepancy in filler/matrix thermal expansion. However, the drawback of this approach is that the control of the toughening process is extremely challenging due to the poor thermal conductivity of polymer which slows down the material's response, mechanically. The toughening via volume dilation of embedded fillers is first proposed in a study by Ho Sung *et al.* It is achieved by pre-stressing the epoxy matrix via the expandable hollow microspheres under heating [32]. This concept was based on mimicking the toughening effect of the phase changing ceramics in the vicinity of the crack. Phase-transition toughening is extensively studied in the past years as one of the most effective toughening mechanisms for ceramics [33]. It has been observed experimentally that the stress-induced martensitic phase transition of a second phase at a crack tip, such as a tetragonal Zirconium dioxide change to a monoclinic phase, can result in volume expansion and forming a compressive stress field around the crack tip to prevent its propagation [34]. Thus far, there are no attempts made to date to investigate the strain behaviour of embedded fillers in rigid polymer composites under an electromagnetic field. Therefore, a novel active toughening effect based on radiation field induced strains has been investigated and presented, by incorporating ferroelectric crystals that demonstrates an electro-strain under an applied electric field.

## 2 Research Hypothesis

Dielectric nanomaterials exhibit electric field induced strain which is attributed to intrinsic mechanisms from lattice deformation and extrinsic mechanisms due to domain wall (DW) movement [35], extensively used as actuators and transducers. The inclusion of such material within a rigid epoxy FRP materials can impose a compressive stress field in its surrounding epoxy matrix when activated its DW movements by external electric field stimulation. As result of the DW movements, a microwave stimulation at GHz frequencies induces effective dipolar displacement (leading to intrinsic strains) to the nanomaterial's molecules that, at the interface with their surrounding rigid polymer, is converted to compressive mechanical strain. The hypothesis of this research was based upon suggesting that microcrack propagation during dynamic and impact events would be suppressed under such microwave induced compressive stress-strain field, i.e. higher strain energy would be required to create new fracture surfaces. Also, it would provide the interphase with self-adjusting properties, i.e. enhanced mechanical properties e.g. Young's moduli, while improving the stress transfer by constraining microcracks. Therefore, the study focused on: 1- development of a modified epoxy with uniformly distributed dielectric nanomaterials that exhibit electro-strain, 2- in-situ quantification of its strain response under an electromagnetic field (e.g. microwave), and 3- establishment of a theoretical constitutive equation underpinning the correlation between the induced mechanical field and the microwave field.

To investigate the microstructural response of such dielectric nanomaterial embedded nanocomposite under an electromagnetic field, firstly, we developed a modified epoxy system with uniformly distributed barium titanate (BaTiO<sub>3</sub>) nanoparticles. Materials' properties, functionalisation and fabrication methods developed in the research are described in section 6.1. Newly established constitutive equations underpinning the multi-physics field induced strain and temperature have been provided in section 5. With a

second phase added to the epoxy system, the dielectric properties have been improved. Meanwhile, it also has effects on the curing extent of the epoxy system. Basic dielectric and cure state characterisation methods and their results are presented and described in sections 6.2.1 and 7.1, respectively. To experimentally measure the perceivable strain effect induced by the stimulation of embedded BaTiO<sub>3</sub> particles' strains under microwave stimulation, fibre optic sensors utilising fibre Bragg grating (FBG) technique have been employed. The instrumented nanocomposite samples have been placed in a temperature-power controlled microwave oven cavity where their in-situ real-time strain-temperature evolution has been examined with the increasing microwave power and energy at constant 2.45 GHz frequency. The experiment set-up and procedure have been described in section 6.2.2. The results of the in-situ measurements have been presented in section 7.2. Raman spectroscopy was employed to observe residual internal stresses post microwave exposure. Its results are presented and discussed in section 7.3. The theoretical solution from the newly established constitutive expressions have been presented, where their ability to underpin the experimental data have been assessed.

### 3 Electric Field Induced Strain in Ferroelectric Materials

BaTiO<sub>3</sub> like other ferroelectric materials exhibit spontaneous polarisation at its polar phase that could be switched by applying an external electric field [36, 37], containing crystals having a net permanent polarisation which is the vector sum of all the dipole moments in a unit cell [38, 39], due to the absence of a centre of symmetry. It belongs to the perovskite oxides group, cubic form above 120°C with the Ba<sup>2+</sup> ions at the corners, the Ti<sup>4+</sup> ion at the cube centre and the O<sup>2-</sup> ions at the face centres [40]. Below 120°C (the current research), the cubic structure deforms into a tetragonal polar structure with a shifting centre atom Ti<sup>4+</sup>. A dipole moment is created by the displaced Ti<sup>4+</sup> ion, and hence the spontaneous polarisation. The Ti<sup>4+</sup> ion can be displaced to six different directions therefore the corresponding dipole moment can have six directions along these crystallographic axes. When an electric field is applied, while the strength of the field increases, the polarisation increases and reaches a saturation state where all dipoles are aligned with the field direction. When the external field is removed, the polarisation may not return back to zero, i.e. displaying a remnant polarisation  $P_r$  [41].

BaTiO<sub>3</sub> domain wall is characterised by the angle of polarisation axes between two adjacent domains, such as 180° and 90° domain walls [42]. The 90° and 180° domain walls exist in a tetragonal phase of BaTiO<sub>3</sub> [43]. Generally speaking, 180° domain walls are only responsive under electric fields while the other non-180° domain walls are responsive under both electric and mechanical stress fields [42]. Therefore, the DW configuration of BaTiO<sub>3</sub> is defined by its own structure, and it changes by dipole displacements under an electric field or mechanical loading [44]. When an electric field is applied to the BaTiO<sub>3</sub> crystals with a perovskite structure, three main representative deformations contribute to its mechanical strain response [45], the intrinsic strain is induced by its electrostriction and piezoelectric effects while the extrinsic strain is attributed to the domain wall movement in the polydomain materials as presented in Figure 1.

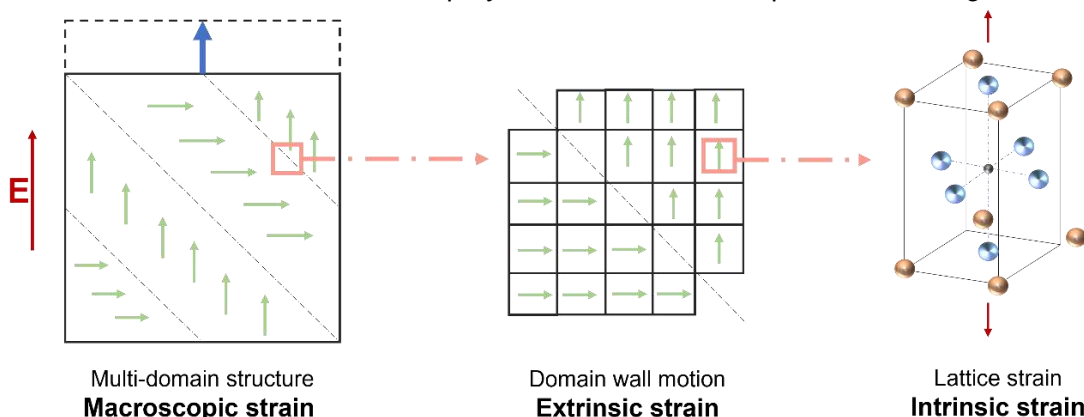


**Figure 1** Schematic diagram of the extrinsic strain and intrinsic strain that contributes to macroscopic strain in a tetragonal crystal (red, green and blue arrows represent electric field induced intrinsic strain, extrinsic strain and macroscopic strain, respectively).

In a mono-domain ferroelectric crystal, the electric field-induced strain is generated by the intrinsic electrostriction and piezoelectric effect. In both poly-domain single crystal and polycrystalline ferroelectric materials, the domains that contain spontaneous polarisation in various directions can be aligned to the same direction by applying an external electric field. In a poly-domain ferroelectric crystal, the macroscopic strain is significantly dominated by the contribution of extrinsic strain [46]. Extrinsic effects occur at longer length-scales and the main contributor is domain wall motion, a major motivation for the hypothesis behind the development of the current research. The non-180° domain wall motion is the primary but not the only contribution of the extrinsic strain effect. Furthermore, the 90° domain wall movement also contributes to enhanced electromechanical performance in tetragonal BaTiO<sub>3</sub> single crystals with nanodomain configurations [47, 48]. The 90° domain switching in BaTiO<sub>3</sub> introduces a large electro-strain due to the exchange of two different crystallographic axes, and the field induced strain is one or two orders of magnitude larger than the linear electro-strain of piezoelectric materials. After the removal of the electric field, the domain structure cannot be restored to its original form due to lack of energy and remnant polarisation in each domain. Therefore, the 90° domain switching is theoretically a one-time process [47]. Due to the lack of driving force to restore the original domain configuration after removing the field, the domain wall movement is irreversible and consequently the macroscopic strain [49]. BaTiO<sub>3</sub> crystals, however, exhibit more complex domain structures due to different crystallographic axes in the tetragonal phase. Apart from the normal parallel 180° domains, there also exist adjacent domains that are polarised at 90° to each other. It is observed by Hsiang *et al.* [50] that the 40-80 nm BaTiO<sub>3</sub> powders exhibit a single-domain structure while powders with sizes larger than 80 nm are polydomain tetragonal structures (the case examined by this research). Moreover, Dudhe *et al.* observed the 90° and 180° nano-domains of 80 nm BaTiO<sub>3</sub> nanoparticles. Other studies focused on the polydomain structure of BaTiO<sub>3</sub> nanoparticles with the grain size of 50-70 nm found that the domain size is 10-12 nm [51]. The 90° domains in BaTiO<sub>3</sub> crystals are capable of introducing a large strain that is attributed to the crystallographic axes exchange under alternating electric field [49]. However, it is difficult to distinguish the contributions from intrinsic and extrinsic (domain wall movement) contributions and conventionally, the single-domain crystals are considered to be only affected by the intrinsic properties while the contributions of the extrinsic domain wall movement are investigated in the polydomain crystals, as observed in [42]. Therefore, in this research, polydomain BaTiO<sub>3</sub> nanoparticles is employed to achieve the field-induced strain effect.

#### 4 Interaction of Ferroelectric Materials with the Microwave Field

The mechanism of the material and microwave interaction is particularly complex and it involves the orientation of dipoles, free-to-move electrons, domain wall movement and electron spins, which are activated by the electric and/or magnetic field components [52]. The essence of the interaction between the dielectric material and the electromagnetic field is energy transformation at the molecular level. Therefore, the dielectric properties of a material, which is measured as the complex permittivity quantifies the ability of a dielectric material to absorb and store electrical potential energy when exposed to a microwave field [53]. The complex permittivity that represents the microwave-material interactions are expressed by:

$$\varepsilon = \varepsilon' - j\varepsilon'' \quad 1$$

where  $\varepsilon'$  is the real parts of the permittivity that indicating the ability to store microwave energy of the material while  $\varepsilon''$  is the imaginary part of the permittivity that indicating the ability to dissipate the microwave energy [53]. The dielectric loss tangent is expressed by:

$$\tan \delta = \frac{\varepsilon''}{\varepsilon'} \quad 2$$

The loss tangent is the measure of the material to convert absorbed energy into other forms of energy such as heat [54]. The dipoles in an alternating electric field will reorient themselves to align with the new field direction. However, this process cannot occur instantaneously due to inherent non-zero inertia, and thus some time is required to fulfil the reorientation of the dipoles. At microwave frequencies, dipole polarisation is assumed to be the most dominant one for energy transfer at the molecular level.

## 5 Theoretical Multi-physics Constitutive Equations

In this section, the theoretical analysis of the strain field induced in BaTiO<sub>3</sub> nanoparticles embedded epoxy under microwave exposure is established. Firstly, the theory of dynamic elastic response of tetragonal BaTiO<sub>3</sub> nanoparticles under alternating electric field at the microwave exposure is presented and discussed [55]. The displacement of the DWs is utilised as the eigenstrain for the estimation of the strain field in the BaTiO<sub>3</sub>-epoxy nanocomposite. A novel approach based on the principle of virtual work of the equivalent eigenstrain is incorporated in the calculation of the inhomogeneous inclusion [56]. Based on this approach, a theoretical framework of microwave activated dynamic elastic response of the nanocomposite has been established. Finally, the non-uniform distribution of the microwave field and the interaction with the samples have been incorporated in the framework.

### 5.1 Deformation in a Representative Crystallite of BaTiO<sub>3</sub> under the Microwave Field

The 90° DW movement is considered to have the major contribution to the extrinsic field-induced strain. Therefore, the tetragonal BaTiO<sub>3</sub> nanoparticle is assumed to be formed by several multi-domain crystallites that contain a laminar 90° domain structure. A conceptual schematic of a crystallite is shown in Figure 2. The domain wall movement in such crystallite is assumed to be not affected by that in other crystallites.

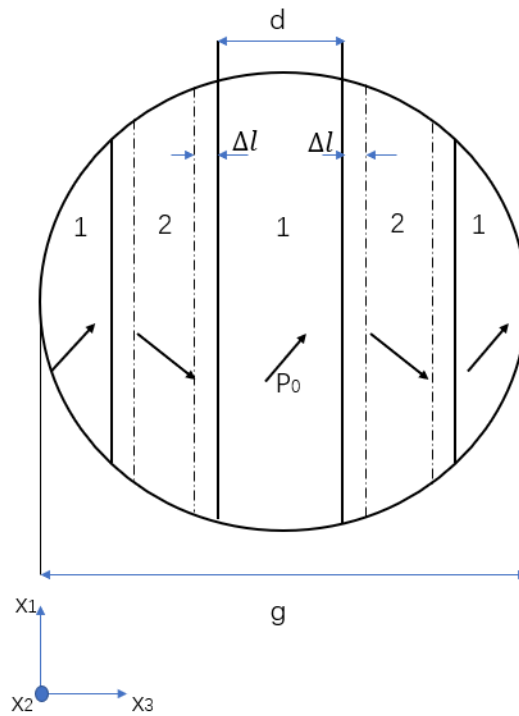


**Figure 2** Schematic illustration of a spherical nanoparticle (simplified as a crystallite) with a laminar 90° domain structure with spontaneous polarisation  $P_0$  and domain size  $d$ , recreated from [57].

Before the application of the microwave field, it is assumed that the DWs are in an equilibrium state, and all the domains are of an identical size, dielectric properties and elastic properties. Therefore, the interactions between adjacent domains are not included as it is assumed negligible compared with other factors as suggested in a previous study [58]. Moreover, the internal electric and mechanical fields are assumed to be negligible, hence no forces acting on the DWs prior to the microwave exposure [59]. When the microwave field is applied, the interactions with the magnetic component are negligible since BaTiO<sub>3</sub> is non-ferrite. The alternating electric component of the microwave field is assumed to be homogenous across the whole nanoparticle in this research. It is assumed that the spontaneous polarisations in the 90° domains re-orient themselves with the direction of an applied alternating electric field. Consequently, a driven force  $f_A(t)$  as the function of time is introduced on the DWs that enables the DW motion due to polarisation change [60]. The displacement of the DW movement is denoted as  $\Delta l$  in Figure 2. Due to the BaTiO<sub>3</sub> ferroelectricity, such movement introduces an internal electric field  $E$  in the nanoparticle due to the change in the

polarisation direction. As a result, the internal stress field is also no longer negligible due to the newly developed internal electric field and DW movement from its equilibrium position. An additional force  $f_I$  on the DWs is developed subsequently due to the change in the internal electric and stress fields from zero state. Due to the displacements in DWs, the electric dipole moment  $\Delta p$  induced by the internal electric field, and the elastic dipole moments  $\Delta v$  induced by the internal mechanical stress field are given by [61] :

$$\Delta p = \sqrt{2}P_0\Delta l \quad 3$$

$$\Delta v = 2S_0\Delta l \quad 4$$

where  $P_0$  is the spontaneous polarisation, and  $S_0$  is the spontaneous deformation. The correlation between  $\Delta l$  and the dipole moments is assumed to be linear, and their internal energy  $W_{electric}$  under the internal electric field  $E$ , and  $W_{elastic}$  under mechanical stress field  $T_{13}$  are:

$$W_{electric} = -\sqrt{2}P_0\Delta l E \quad 5$$

$$W_{elastic} = -2S_0\Delta l T_{13} \quad 6$$

where  $E$  is the internal electric field, and  $T_{13}$  is the internal mechanical stress  $T_{ij}$  ( $i, j=1,2,3$ ) as illustrated in a cartesian coordinate system ( $x_1, x_2, x_3$ ) in Figure 2.

The expression for the DW motion is [60]:

$$kA_{DW}\Delta l = -\left(\frac{\partial W_{electric}}{\partial \Delta l} + \frac{\partial W_{elastic}}{\partial \Delta l}\right) \quad 7$$

By the derivation of Equation 5 and Equation 6, the force  $f_I$  due to the internal fields per unit area  $k\Delta l$  is obtained from

$$k\Delta l = \sqrt{2}P_0E + 2S_0T_{13} \quad 8$$

where  $k$  is the force constant per unit DW area, and  $A_{DW}$  is the area of the DW. The displacements for the DWs from their equilibrium state under the microwave field are assumed to have the same magnitude,  $|\Delta l(t)|$ . The force  $f_I$  per unit DW area at a random point  $r$ , and time  $t$  can then be expressed by Equation 8:

$$f_I(r, t) = \sqrt{2}P_0E_1(r, t) + 2S_0T_{13}(r, t) \quad 9$$

The DWs motion is then described by the Newton's second law of motion:

$$m\Delta \ddot{l} = \bar{f}_I(t) + f_A(t) \quad 10$$

where  $m$  is the mass of a DW per unit area,  $\bar{f}_I(t)$  is the mean value of the DWs driven force  $f_I$  from the internal fields,  $f_A(t)$  is the aforementioned exerted force on the DWs by the applied microwave field. The  $\bar{f}_I(t)$  is then calculated by averaging the  $f_I(r, t)$  over the summation of the DWs surfaces ( $d\Sigma$ ) in a nanoparticle, as presented below [55].

$$\bar{f}_I(t) = \frac{1}{\Sigma} (2S_0 \int_{\Sigma} T_{13}(r, t) d\Sigma + \sqrt{2}P_0 \int_{\Sigma} E(r, t) d\Sigma) \quad 11$$

The DW displacements induced internal electric field  $E(r, t)$  and internal mechanical field  $T_{13}(r, t)$  in Equation 11 must firstly be calculated prior to the  $\bar{f}_I(t)$  calculation. The internal electric field was evaluated in a quasi-static approximation for a given microwave field, and  $E(r, t)$  is considered to be proportional to the DW displacement  $\Delta l(t)$ . The internal mechanical stress field  $T_{ij}$  was considered as a dynamic problem as the DW motions lag behind the 2.45 GHz microwave frequency [55]. In this study, only the extrinsic

effect, i.e. the DW motions, is considered as they are commonly accepted to be the primary contributor to the electro-strain compared with the intrinsic effect such as piezoelectric effect and electrostriction.

To obtain the value of the internal mechanical stress field, the change of the spontaneous deformation  $S_0$  introduced by the DW displacements in Equation 11 was calculated, thus the  $\Delta S_{13}^0(r, t)$  and  $\Delta S_{31}^0(r, t)$  were approximated by [55]:

$$\Delta S_{13}^0(r, t) = \Delta S_{31}^0(r, t) = S_0 \frac{\Delta l(t)}{w} \delta(V_{DW}) \quad 12$$

where  $w$  is the thickness of a 90° DW,  $V_{DW}$  is the volume of DWs without an applied microwave field, and  $\delta(V_{DW})$  is the Dirac delta function for  $V_{DW}$ .

The thickness  $w$  is approx. 100 Å, much smaller compared with the domain width  $d$  and the particle size [57], therefore, Equation 12 was simplified to Equation 13 [55].

$$\Delta S_{13}^0(r, t) = \Delta S_{31}^0(r, t) = S_0 \Delta l(t) \delta(\Sigma) \quad 13$$

where  $\Sigma$  represents the midplanes of DWs when  $\Delta l = 0$ ,  $\delta_3(\Sigma)$  is the Dirac delta function of the  $\Sigma$  with a unit normal directed along the  $x_3$  axis [62].

The internal mechanical stress field which introduces the change of  $\Delta S_{mn}^0(r, t)$  was then approximated as follows [55]:

$$p_k = -c_{klmn} \Delta S_{mn,l}^0 \quad 14$$

where  $c_{klmn}$  is the elastic constant tensor of the nanoparticle, and the index  $l$  in the subscript denotes the differentiation with respect to the coordinate  $x_l$  ( $l = 1, 2, 3$ ). Based on the dynamic elasticity theory [63], the total displacement  $u_i^T(r, t)$  ( $i = 1, 2, 3$ ) of a unit cell is expressed as [55]:

$$u_i^T(r, t) = \int dV' \int_{-\infty}^t G_{ik}(r - r', t - t') p_k(r', t') dt' \quad 15$$

Where  $G_{ik}$  is the dynamic Green's tensor,  $V'$  represents the overall surfaces of the nanoparticle, the  $r'$  and  $t'$  is the original equilibrium position and time before the microwave field is applied. Equation 14 is then substituted into Equation 15:

$$u_i^T(r, t) = -2GS_0(\delta_{k1}\delta_{l3} + \delta_{k3}\delta_{l1}) \int_{\Sigma} d\Sigma' \times \left( \int_{-\infty}^t G_{ik}(r - r', t - t') \Delta l(t') dt' \right)_{,l} \quad 16$$

where  $G$  is the shear modulus of the nanoparticle,  $\delta_{km}$  is the Kronecker delta, and the expression of  $G_{ik}$  used in this calculation was taken from [63]. The total deformation was expressed as [55]:

$$S_{ij}^T(r, t) = \frac{1}{2} [u_{i,j}^T(r, t) + u_{j,i}^T(r, t)] \quad 17$$

The electric component of the oscillating microwave field is a sinusoidal function of time and the DW displacement  $\Delta l(t)$  is written as

$$\Delta l(t) = \Delta l_m \sin \omega t \quad 18$$

where  $\Delta l_m$  is the maximum displacement of the DWs under the microwave field. Substituting Equation 16 and the expression of  $G_{ik}(r, t)$  into Equation 17, the internal mechanical stress field  $T_{13} = T_{31} = G(S_{13} + S_{31})$  is obtained with dimensionless functions  $h_s(r)$  and  $h_c(r)$  (presented at the end of this section due to the lengthiness of the equations) as [55]:

$$T_{13}(r, t) = T_{31}(r, t) = -GS_0 \frac{\Delta l_m}{d} [h_s(r) \sin \omega t + h_c(r) \cos \omega t] \quad 19$$

The nanoparticle is assumed to be a homogeneous and isotropic dielectric medium, and the internal electric field  $E(r, t)$  is proportional to  $\Delta l(t)$ ,

$$E(r, t) = -\frac{P_0}{\epsilon_0} \frac{\Delta l_m}{d} h_e(r) \sin \omega t \quad 20$$

where  $\epsilon_0$  is the permittivity of the free space ( $\epsilon_0 = 8.8542 \times 10^{-12}$  F/m),  $d$  is the width of the DW, and  $h_e(r)$  are approximated as [55]:

$$h_e(r) = \frac{\sqrt{2}}{\epsilon_{11} + 2\epsilon^*} \quad 21$$

where  $\epsilon_{11}$  is first component of the dielectric permittivity tensor  $\epsilon_{ij}$  ( $i, j = 1, 2, 3$ ) that represents the dielectric permittivity of the crystallite as illustrated in Figure 2, and  $\epsilon^*$  is the dielectric permittivity of the nanoparticle. The force  $\bar{f}_I$  was then calculated with the internal mechanical stress field  $T_{13}(r, t)$  from Equation 19, and the internal electric field  $E(r, t)$  from Equation 20 and Equation 21. The field-induced force  $f_A$  is due to the effective electric field in the  $x_1$  direction of the applied microwave field as illustrated in Figure 2. The electric field component  $E_{A1}$  is a function of time as follows:

$$E_{A1}(t) = E_m \sin(\omega t + \phi) \quad 22$$

where  $E_m$  is the amplitude of the electric component of the microwave field, and  $\phi$  is the phase lag of the DW motion relative to the oscillatory microwave field. Equation 22 is then substituted into Equation 8 with the second part equalling zero as  $f_A(t)$  is only introduced by an electric field:

$$f_A(t) = \sqrt{2}P_0E_m \sin(\omega t + \phi) \quad 23$$

Finally Equation 11, Equation 19, Equation 20, and Equation 23 are substituted into Equation 10, giving:

$$\begin{aligned} \frac{\Delta l_m}{d} \left[ \left( 2GS_0^2 \bar{h}_s(\omega) + \sqrt{2} \left( \frac{P_0^2}{\epsilon_0} \right) \bar{h}_e - md\omega^2 \right) \sin \omega t + 2GS_0^2 \bar{h}_c(\omega) \cos \omega t \right] \\ = \sqrt{2}P_0E_m(\cos\phi \sin \omega t + \sin\phi \cos \omega t) \end{aligned} \quad 24$$

where  $\bar{h}_s$ ,  $\bar{h}_c$ , and  $\bar{h}_e$  are the average of  $h_s(r)$ ,  $h_c(r)$  and  $h_e(r)$  over DW surface  $\Sigma$ . From Equation 24, it could be seen that the DW displacement  $\Delta l_m$  is correlated with the properties and strength of the electric component of the microwave field  $E_m$  and the dielectric permittivity of the nanoparticle. The value of the DW displacement  $\Delta l_m(\omega)$  could be obtained by numerical computations of the  $\bar{h}_s(\omega)$  and  $\bar{h}_c(\omega)$ .

To get an approximate estimate, a further simplification was made that the nanoparticles are sufficiently small to be considered as a multi-domain single crystal, namely a crystallite. Therefore, the crystallite as illustrated in Figure 2 could be considered as a single BaTiO<sub>3</sub> nanoparticle without any adjacent crystallite, and hence no corresponding internal electric and stress field. Consequently, Equation 10 is simplified to:

$$m\Delta\ddot{l} = f_A(t) = \sqrt{2}P_0E_m \sin(\omega t + \phi) \quad 25$$

It is assumed that the DW movement under the oscillatory microwave field is a simple harmonic motion with a driven force of  $f_A(t)$ . Neglecting the lag in the dipoles reorientation, the DW motion becomes in phase with the oscillating field. The driving force at the maximum electric field strength  $f_m$  is then obtained by:

$$f_m = \sqrt{2}P_0E_m, \quad 26$$

and the amplitude  $\Delta l_m$ :

$$\Delta l_m = \frac{\sigma L}{Y} = \frac{f_m L}{AY} = \frac{f_m L}{d^2 Y} \quad 27$$

where  $Y$  is the young's modulus of the BaTiO<sub>3</sub> nanoparticle and  $d$  is the domain width where the area of the domain is approximated to be  $d^2$ .

**Dimensionless functions of  $h_s(\mathbf{r})$ ,  $h_c(\mathbf{r})$ :**

The internal stresses  $T_{13}$  and  $T_{31}$  induced by DW displacements in a crystallite, is determined by the functions  $h_s(\mathbf{r})$  and  $h_c(\mathbf{r})$ . The dynamic Green's function  $G_{ik}(\mathbf{r}, t)$  of an isotropic elastic medium is employed in the study and the analytical expression is presented below [55].

$$G_{ik}(\mathbf{r}, t) = \frac{1}{4\pi\rho r} \left[ \frac{n_i n_k}{c_t^2} \delta\left(t - \frac{r}{c_l}\right) + \frac{\delta_{ik} - n_i n_k}{c_t^2} \delta\left(t - \frac{r}{c_t}\right) \right] + \frac{t - (\delta_{ik} - 3n_i n_k)}{4\pi\rho r^3} \left[ \Theta\left(t - \frac{r}{c_t}\right) - \Theta\left(t - \frac{r}{c_l}\right) \right] \quad 28$$

$$\Theta(x) = \begin{cases} 0, & x < 0 \\ 1, & x > 0 \end{cases} \quad 29$$

The  $h_s(\mathbf{r})$  and  $h_c(\mathbf{r})$  functions are expressed as follows:

$$h_s(\mathbf{r}) = \frac{d}{2\pi} \left\{ \oint_L \frac{\Delta x_2}{R^3} dL'_1 + 2 \oint_L \frac{\Delta x_1}{R^3} \left[ \cos \frac{\omega R}{c_t} - 1 + \frac{\omega R}{c_t} \sin \frac{\omega R}{c_t} + 2 \frac{\Delta x_3^2}{R^2} \frac{\omega R}{c_t} \left( \frac{c_t^3}{c_l^3} \sin \frac{\omega R}{c_l} - \sin \frac{\omega R}{c_t} \right) - 2 \left( 1 - 6 \frac{\Delta x_3^2}{R^2} \right) \left( \frac{c_t^2}{c_l^2} \cos \frac{\omega R}{c_l} - \cos \frac{\omega R}{c_t} \right) + 6 \left( 1 - 5 \frac{\Delta x_3^2}{R^2} \right) \left( \frac{\omega R}{c_t} \right)^{-2} \left( \cos \frac{\omega R}{c_l} - \cos \frac{\omega R}{c_t} + \frac{\omega R}{c_l} \sin \frac{\omega R}{c_l} - \frac{\omega R}{c_t} \sin \frac{\omega R}{c_t} \right) \right] dL'_2 + \int_{\Sigma} \frac{(\Delta x_3^2 - \Delta x_1^2)}{R^5} \left[ 3 \left( \cos \frac{\omega R}{c_t} - 1 + \frac{\omega R}{c_t} \sin \frac{\omega R}{c_t} \right) - \left( \frac{\omega R}{c_t} \right)^2 \sin \frac{\omega R}{c_t} \right] d\Sigma' \right\} \quad 30$$

$$h_c(\mathbf{r}) = \frac{d}{2\pi} \left\{ \oint_L \frac{\Delta x_1}{R^3} \left[ -\sin \frac{\omega R}{c_t} + \frac{\omega R}{c_t} \cos \frac{\omega R}{c_t} + 2 \frac{\Delta x_3^2}{R^2} \frac{\omega R}{c_t} \left( \frac{c_t^3}{c_l^3} \cos \frac{\omega R}{c_l} - \cos \frac{\omega R}{c_t} \right) + 2 \left( 1 - 6 \frac{\Delta x_3^2}{R^2} \right) \left( \frac{c_t^2}{c_l^2} \sin \frac{\omega R}{c_l} - \sin \frac{\omega R}{c_t} \right) + 6 \left( 1 - 5 \frac{\Delta x_3^2}{R^2} \right) \left( \frac{\omega R}{c_t} \right)^{-2} \left( -\sin \frac{\omega R}{c_l} + \sin \frac{\omega R}{c_t} + \frac{\omega R}{c_l} \cos \frac{\omega R}{c_l} - \frac{\omega R}{c_t} \cos \frac{\omega R}{c_t} \right) \right] dL'_2 + \int_{\Sigma} \frac{(\Delta x_3^2 - \Delta x_1^2)}{R^5} \left[ 3 \left( -\sin \frac{\omega R}{c_t} - 1 + \frac{\omega R}{c_t} \cos \frac{\omega R}{c_t} \right) + \left( \frac{\omega R}{c_t} \right)^2 \sin \frac{\omega R}{c_t} \right] d\Sigma' \right\} \quad 31$$

where,  $R = |\mathbf{r} - \mathbf{r}'| = (\Delta x_1^2 + \Delta x_2^2 + \Delta x_3^2)^{\frac{1}{2}}$ ,  $\Delta x_i = x_i - x'_i$ ,  $d$  is the domain width,  $\omega_{DW}$  is the frequency of DW vibrations,  $c_t$  and  $c_l$  are the phase velocities of transverse and longitudinal DW vibrations generated in the nanoparticle.

## 5.2 Epoxy Embedded with a BaTiO<sub>3</sub> Nanoparticle

Eshelby's inclusion approach has been employed in this study to compute the effective stress field within an epoxy matrix with the embedded BaTiO<sub>3</sub> nanoparticle. General Eshelby's inclusion problem involves ellipsoidal inclusions in an infinite linear elastic medium [64, 65]. Therefore, the embedded BaTiO<sub>3</sub> nanoparticle is an inhomogeneous spherical inclusion as it has different elastic properties compared with the surrounding epoxy matrix. This method is widely accepted by many studies to solve problems involving thermal expansion, reinforced composite materials, phase transformation, etc. [66, 67]. For an inhomogeneous spherical inclusion that displays non-uniform eigenstrain, a generalised adaption of Eshelby's inclusion method proposed based on the principle of virtual work is employed in this study and presented below [56]: First, equations based on the elastic theory to solve the eigenstrain of Eshelby's inclusion have been utilised, in which the total strain of infinitesimal deformations is expressed as:

$$\varepsilon_{ij} = e_{ij} + \varepsilon_{ij}^* \quad 32$$

where  $e_{ij}$  is the elastic strain, and  $\varepsilon_{ij}^*$  is the eigenstrain. The compatibility condition of total strain  $\varepsilon_{ij}$  is expressed in terms of displacement  $u_i$ , i.e.

$$\varepsilon_{ij} = \frac{u_{i,j} + u_{j,i}}{2}. \quad 33$$

The stress  $\sigma_{ij}$  is then expressed by the Hooke's Law,

$$\sigma_{ij} = C_{ijkl}e_{kl} = C_{ijkl}(\varepsilon_{kl} - \varepsilon_{kl}^*) = C_{ijkl}(u_{k,l} - \varepsilon_{kl}^*), \quad 34$$

where  $C_{ijkl}$  is the effective stiffness tensor,  $C_{ijkl} = C_{ijlk}$  and  $C_{ijkl}u_{k,l} = C_{ijkl}u_{l,k}$ . In the region where  $\varepsilon_{kl}^* = 0$ , Equation 34 is re-arranged to:

$$\sigma_{ij} = C_{ijkl}\varepsilon_{kl} = C_{ijkl}u_{k,l} \quad 35$$

The inversed Equation 34 is then expressed by:

$$\varepsilon_{ij} - \varepsilon_{ij}^* = C_{ijkl}^{-1}\sigma_{kl} = S_{ijkl}\sigma_{kl}, \quad 36$$

where  $S_{ijkl}$  is the compliance tensor that has the same symmetries as the stiffness tensor. The equation of equilibrium is then expressed as follows:

$$\sigma_{ij,j} + f_i = 0, (i = 1,2,3), \quad 37$$

where  $f_i$  is the body force, and the boundary condition is:

$$T_i = \sigma_{ij}n_j, \quad 38$$

where  $n_j$  is the outward unit normal vector to the boundary. The corresponding stress and strain field of a homogeneous inclusion in an infinite medium could be obtained using Green's function method with the profile of the inclusion [68]: The Eshelby inclusion's problem is applied as illustrated in Figure 3. It is assumed that the inclusion has a dynamic deformation of the eigenstrain  $\varepsilon(t)$  as a function of time under the microwave field. A fictitious load  $T$  is applied to the inclusion to maintain the original shape. The inclusion is then placed back into the hole within the infinite epoxy matrix with the original shape and size. After removing the applied  $T$ , the inclusion exerts a traction force  $F$  on the matrix, which equals  $-T$ .

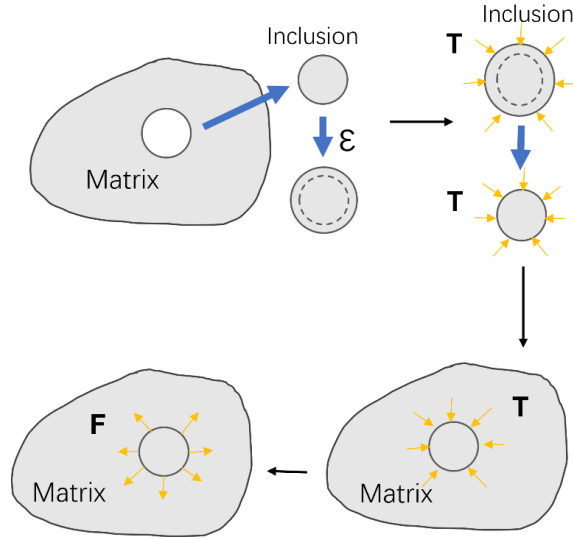


**Figure 3** Schematic diagram of Eshelby's inclusion utilised in our analysis.

It is assumed that the inclusion is in ellipsoids shape and have identical elastic properties with the matrix. Furthermore, the eigenstrain in the inclusion is assumed uniform. Therefore, the inhomogeneous inclusion of embedded BaTiO<sub>3</sub> nanoparticles has been solved by transforming the inhomogeneous inclusion into a homogenous inclusion. The nanoparticle with residual strain embedded within the epoxy was transformed into a homogenous inclusion problem with a distribution of equivalent eigenstrain.

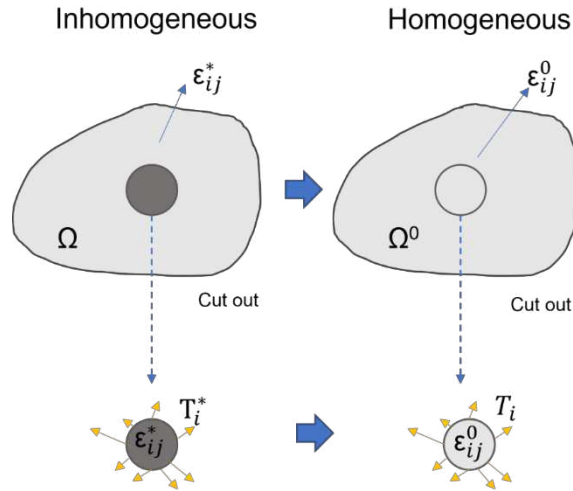


**Figure 4** Schematic diagram of the principle of equivalent eigenstrain of transforming inhomogeneous problem to a virtual homogeneous problem.

The transformation illustrated in Figure 4 was based on the principle of virtual work [56]. Firstly, the inclusions in both inhomogeneous and homogeneous cases in Figure 4 are imaginarily cut-sectioned from the matrix, and the virtual works are expressed in Equation 39, over the  $\Omega$  region of the inhomogeneous problem, and Equation 40 over the  $\Omega^0$  region of the virtual homogeneous problem.

$$\int_v f_i^* \delta u_i dv + \int_s T_i^* \delta u_i ds = \int_v \sigma_{ij}^* \delta \epsilon_{ij} dv \quad 39$$

$$\int_v f_i \delta u_i dv + \int_s T_i \delta u_i ds = \int_v \sigma_{ij} \delta \epsilon_{ij} dv, \quad 40$$

where  $\delta u_i$  is the virtual displacement,  $\delta \epsilon_{ij}$  is the virtual strain,  $f_i$  is the body force,  $T_i$  is the traction force on the boundary, and  $\sigma_{ij}$  is the stress field in the nanoparticle. Equation 40 minus Equation 39 gives:

$$\int_v (f_i - f_i^*) \delta u_i dv + \int_s (T_i - T_i^*) \delta u_i ds = \int_v (\sigma_{ij} - \sigma_{ij}^*) \delta \varepsilon_{ij} dv. \quad 41$$

As the stress state in both conditions are identical, therefore,  $f_i = f_i^*$ , and  $T_i = T_i^*$ . The  $\delta \varepsilon_{ij}$  can take any arbitrary value, and Equation 41 is then expressed as follows:

$$\sigma_{ij} = \sigma_{ij}^* \quad 42$$

From the stress expression in Equation 34, the stress state is obtained as Equation 43 over  $\Omega$ , and Equation 44 over  $\Omega^0$ :

$$\sigma_{ij}^* = C_{ijkl}^* (\varepsilon_{kl} - \varepsilon_{kl}^*) \quad 43$$

$$\sigma_{ij} = C_{ijkl} (\varepsilon_{kl} - \varepsilon_{kl}^0) \quad 44$$

where  $C_{ijkl}$  and  $C_{ijkl}^*$  are the elastic constant tensors of the homogeneous and inhomogeneous inclusion, respectively,  $\varepsilon_{kl}$  is the total strain,  $\varepsilon_{kl}^*$  is the real residual strain in the inhomogeneous  $\Omega$ , and  $\varepsilon_{kl}^0$  is the equivalent eigenstrain in the homogeneous  $\Omega^0$ . Since  $f_i = f_i^*$  and  $T_i = T_i^*$ , the deformation of the nanoparticle in epoxy in  $\Omega$  is equivalent to that of the virtual homogeneous inclusion in  $\Omega^0$  by incorporating an equivalent eigenstrain  $\varepsilon_{kl}^0$ . The substitution of Equation 42 with Equation 43 and Equation 44 gives:

$$C_{ijkl}^* (\varepsilon_{kl} - \varepsilon_{kl}^*) = C_{ijkl} (\varepsilon_{kl} - \varepsilon_{kl}^0) \quad 45$$

The equivalent eigenstrain in  $\Omega^0$  is then expressed by:

$$\varepsilon_{kl}^0 = (1 - C_{ijkl}^* S_{ijkl}) \varepsilon_{kl} + C_{ijkl}^* S_{ijkl} \varepsilon_{kl}^* \quad 46$$

Therefore, with the equivalent eigenstrain  $\varepsilon_{ij}^0$ , the stress and strain field in the nanoparticle over  $\Omega$  could be calculated using Green's function method as follows [56, 68], accounting for the displacement field for a 3D inclusion:

$$u_i(\mathbf{X}) - \int_{-\infty}^{\infty} C_{jlmn} \varepsilon_{mn}^* (\mathbf{X}') G_{ij,l}(\mathbf{X} - \mathbf{X}') d\mathbf{X}', \mathbf{X}, \mathbf{X}' \in \Omega \quad 47$$

where  $G_{ij,l}(\mathbf{X} - \mathbf{X}')$  is the Green's function, and

$$G_{ij,l}(\mathbf{X} - \mathbf{X}') = \frac{\partial}{\partial x_l} G_{ij}(\mathbf{X} - \mathbf{X}') - \frac{\partial}{\partial x_l'} G_{ij}(\mathbf{X} - \mathbf{X}') \quad 48$$

The strain field is then obtained from Equation 47, i.e.

$$\varepsilon_{ij}(\mathbf{X}) = -\frac{1}{2} \int_{-\infty}^{\infty} C_{klmn} \varepsilon_{mn}^* (\mathbf{X}') \{G_{ik,lj}(\mathbf{X} - \mathbf{X}') + G_{jk,li}(\mathbf{X} - \mathbf{X}')\} d\mathbf{X}' \quad 49$$

The total strain in Equation 46 is then expressed equivalent to the eigenstrain  $\varepsilon_{ij}^0$  given by Equation 49, which gives:

$$\varepsilon_{pq}(\mathbf{X}) = -\frac{1}{2} \int_{-\infty}^{\infty} C_{kl ij} \varepsilon_{ij}^0 (\mathbf{X}') \{G_{pk,lq}(\mathbf{X} - \mathbf{X}') + G_{qk,lp}(\mathbf{X} - \mathbf{X}')\} d\mathbf{X}' \quad 50$$

Therefore, the corresponding deformation field in the inclusion and the matrix can be calculated using Green's function method with the equivalent eigenstrain  $\varepsilon_{ij}^0$ . As illustrated in Figure 5, a BaTiO<sub>3</sub> nanoparticle is embedded in the epoxy matrix, assumed to be in full bonding with the epoxy (i.e. no disbond or interfacial defect) and the epoxy is assumed to be infinite. The BaTiO<sub>3</sub> nanoparticle and the epoxy are assumed to be isotropic. A nominal eigenstrain  $\varepsilon_{ij}^*$ , due to the DW movement is prescribed as shown in the figure. It is assumed that the eigenstrain is the collective displacements of all the domains that may exhibit different polarisation in all possible directions.

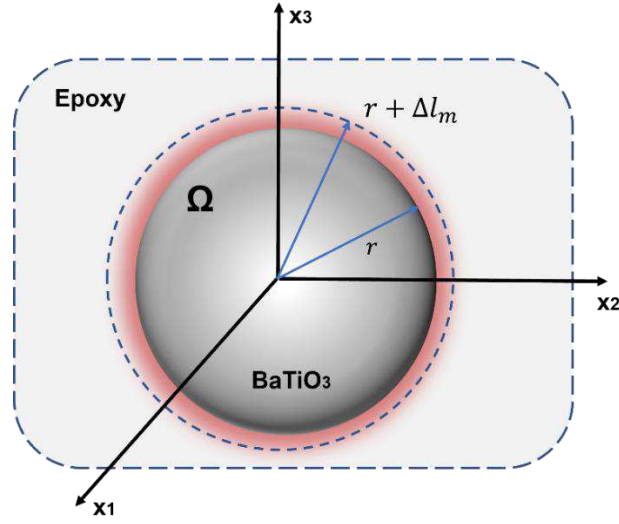


**Figure 5** Schematic view of a BaTiO<sub>3</sub> nanoparticle with radius ( $r$ ) embedded in the epoxy matrix with eigenstrain ( $\Delta L_m$ ).

The nominal eigenstrain is denoted as  $\varepsilon_{ij}^*$ :

$$\varepsilon_{ij}^* = \Delta L_m / r \quad 51$$

The anisotropic elastic constants of isotropic materials are  $C_{ijkl}$ , and  $C_{ijkl}^*$  for Epoxy and BaTiO<sub>3</sub> respectively:

$$C_{ijkl} = \lambda \delta_{ij} \delta_{kl} + \mu (\delta_{ik} \delta_{jl} + \delta_{il} \delta_{jk}) \quad 52$$

$$C_{ijkl}^* = \lambda^* \delta_{ij} \delta_{kl} + \mu^* (\delta_{ik} \delta_{jl} + \delta_{il} \delta_{jk}) \quad 53$$

$$\lambda = \frac{Y}{2(1 + \nu)} \quad 54$$

$$\mu = \frac{Y\nu}{(1 + \nu)(1 - 2\nu)} \quad 55$$

where  $\lambda(\lambda^*)$  and  $\mu(\mu^*)$  are Lamé constants [69],  $\nu$  is the Poisson ratio, and  $\delta_{ij}$  is the Kronecker delta. Inserting Equation 52 Equation 53 into Equation 46:

$$\lambda \delta_{ij} \varepsilon_{kk}^0 + 2 \mu \varepsilon_{ij}^0 = [(\lambda - \lambda^*) \delta_{ij} \varepsilon_{kk} + 2(\mu - \mu^*) \varepsilon_{ij}] + (\lambda^* \delta_{ij} \varepsilon_{kk}^* + 2\mu^* \varepsilon_{ij}^*) \quad 56$$

The equivalent eigenstrain  $\varepsilon_{kl}^0$  and total strain can then be re-written as  $\varepsilon_{kl}$ :

$$\varepsilon_{kl}^0 = \delta_{kl} \varepsilon_0, \quad \varepsilon_{kl} = \delta_{kl} \varepsilon \quad 57$$

where  $\varepsilon$  is a function of  $\varepsilon_0$  [68]:

$$\varepsilon = \frac{1 + \nu}{3(1 - \nu)} \varepsilon_0 = \alpha \varepsilon_0. \quad 58$$

Therefore, Equation 56 is:

$$(3\lambda + 2\mu) \varepsilon_0 = [3(\lambda - \lambda^*) + 2(\mu - \mu^*)] \varepsilon + (3\lambda^* + 2\mu^*) \varepsilon^* \quad 59$$

And the equivalent eigenstrain  $\varepsilon_0$  is solved by Equation 59:

$$\varepsilon_0 = \frac{3\lambda^* + 2\mu^*}{(3\lambda + 2\mu)(1 - \alpha) + (3\lambda^* + 2\mu^*)\alpha} \varepsilon^* \quad 60$$

Therefore, the strain  $\varepsilon_{kl}$  in the epoxy is expressed by:

$$\varepsilon_{kl} = \frac{(3\lambda^* + 2\mu^*)\alpha}{(3\lambda + 2\mu)(1 - \alpha) + (3\lambda^* + 2\mu^*)\alpha} \varepsilon^* \quad 61$$

### 5.3 Interaction theory of BaTiO<sub>3</sub>-epoxy nanocomposite and microwave field

The major interaction between the dielectric material and the microwave field is the polarisation of the dipoles, i.e. under an oscillatory microwave field, the dipoles re-orient themselves with the external electric field component of the microwave field. Therefore, the BaTiO<sub>3</sub> nanoparticles interact with the electric field component of the microwave field, and the magnetic field effect is considered negligible. The main contribution of microwave power loss in the multi-domain BaTiO<sub>3</sub> nanoparticles originates from the piezoelectric domain wall movement [70]. A significant dielectric loss of the BaTiO<sub>3</sub> nanoparticles occurs at the frequency range of GHz to terahertz (THz) [71]. Compared with the BaTiO<sub>3</sub> nanoparticles, the dielectric loss tangent of epoxy represents the ability to dissipate the absorbed energy is relatively smaller (in the range of 10<sup>-3</sup> to 10<sup>-4</sup>) [72]. The origin of the power loss in most polymers are associated with the dipolar loss due to polar segments of the polymer chain, and it is highly dependent upon the temperature and the frequency [72]. The mobility of the polar segments decreased significantly when the frequency reaches the GHz range [73]. Therefore, the dielectric loss in BaTiO<sub>3</sub>/Epoxy nanocomposites observed at a higher frequency (e.g. microwave at 2.45 GHz) is mainly attributed to the BaTiO<sub>3</sub> nanoparticles.

The behaviour of the electric and magnetic components of the microwave field is governed by Maxwell's equations coupled with boundary conditions [74].

$$\nabla \times \mathbf{H} = j\omega\varepsilon\mathbf{E} \quad 62$$

$$\nabla \times \mathbf{E} = j\omega\mu\mathbf{H} \quad 63$$

$$\nabla \cdot \mu\mathbf{H} = 0 \quad 64$$

$$\nabla \cdot \varepsilon\mathbf{E} = \rho \quad 65$$

where  $\mathbf{H}$  and  $\mathbf{E}$  are the varying magnetic (A/m) and electric field strength (V/m), respectively,  $\omega$  is the angular frequency (rad/s),  $\varepsilon$  is the complex relative permittivity,  $\mu$  is the complex relative permeability, and  $\rho$  is the charge density. The first two equations, so-called Ampere's law and Faraday's law, correlate the changes in the electric or magnetic field. The last two equations are Gauss's laws, which represents the net magnetic flux out of a region. It must be zero while the net electric flux out of a region is related to the charge density within the region [75]. The power absorbed by the material in the microwave field is dependent on many factors such as shape, size, and location of the material. For a relatively thin material that fully penetrated by the microwave field, the power dissipated  $P$  (W/m<sup>3</sup>) as heat in the material under microwave field is expressed based on Maxwell's Equation as follows [76]:

$$P = \omega(\mu_0\mu''H_{rms}^2 + \varepsilon_0\varepsilon''E_{rms}^2), \quad 66$$

where the first term  $\mu_0\mu''H_{rms}^2$  describes the dissipation of power due to magnetic field and can be neglected for a non-ferrite material, e.g. BaTiO<sub>3</sub>,  $\omega = 2\pi f$ ,  $f$  is the frequency of the applied microwave field (= 2.45 GHz),  $\varepsilon_0$  is the dielectric permittivity of the free space,  $\varepsilon''$  represents the imaginary part of the complex dielectric permittivity, and  $E_{rms}$  is the root-mean-square value of the local electric field strength (V/m). Therefore, Equation 67 is simplified to:

$$P = \omega\varepsilon_0\varepsilon''E_{rms}^2 \quad 67$$

However, the explicit evaluation of the absorbed power by the material inside the oven cavity is difficult to obtain due to the non-uniformity of the microwave distribution, and hence a varying electric field strength. The power absorbed by the material  $P_{absorb}$ , is expressed as follows:

$$P_{absorb} = P_{input} - P_{reflected} - P_{oven}, \quad 68$$

where  $P_{input}$  is the input power from the magnetron,  $P_{reflected}$  is the power reflected and attenuated, and  $P_{oven}$  is the power absorbed by the cavity wall, waveguide, and magnetron. The increased temperature due to microwave heating also has a significant impact on the dielectric properties of the material, which in turn affect the degree of interaction of the nanocomposite with the microwave field. In previous studies, an empirical approach has been proposed to estimate the absorbed power. It is assumed that the amount of microwave energy absorbed by the material/field interaction is converted into heat during the exposure, and is expressed as follows [77, 78]:

$$\sum mC\Delta T = 2\pi f \varepsilon_0 \varepsilon'' E_{rms}^2 Vt \quad 69$$

where  $m$  is the mass of the material,  $C$  is the specific heat capacity of the material,  $\Delta T$  is the temperature change,  $V$  is the volume of the material, and  $t$  is the microwave exposure time.

The energy transferred into the material is also significantly determined by the depth up to which the microwave field travels into it. The degree of microwave penetration in the material is defined by a factor, Penetration depth ( $d_p$ ) [79, 80], which is the distance between the surface of the material and the place inside the material where the magnitude of the field strength drops to  $e^{-1}$  (36.8%) of that at the surface. The penetration depth  $d_p$  neglecting the effects from the magnetic field for a non-ferrite material is expressed as follows [78]:

$$d_p = \frac{c}{\omega \sqrt{2\varepsilon'} \left[ \left( \sqrt{1 + (\tan \delta)^2} - 1 \right) \right]^{1/2}} \quad 70$$

where  $c$  is the velocity of light,  $\varepsilon'$  is the real part of the complex dielectric permittivity, and  $\tan \delta$  is the tangent loss of the material,  $\tan \delta = \varepsilon'' / \varepsilon'$ . Generally speaking, the microwave power decays more quickly in lossy materials with higher  $\tan \delta$  due to energy dissipation hence a lower penetration depth.

From Maxwell's equation, it is noted that the energy of the microwave field is proportional to the square of the amplitude, which represents the maximum strength of its electric and magnetic components. For a continuous sinusoidal microwave field in the air of an empty cavity, the average intensity  $I$  is the power carried by the microwave field per unit area, and is expressed as follows [81]:

$$I = \frac{c \varepsilon_0 E_m^2}{2}, \quad 71$$

where  $E_m$  is the maximum electric field strength, and the root-mean-square value of the electric field is:

$$E_{rms} = \sqrt{E_m^2/2}. \quad 72$$

Equation 71 and Equation 72 above could only be used to calculate the electric field strength in an empty oven. When a sample is placed in the multimode microwave oven (our case), the electromagnetic field is considered to be a superposition of multiple plane waves penetrate the material from different directions. Regardless of the differences in each mode, the superposition of all the waves could be assumed to have an approximately uniform and constant distribution pattern in the material within the localised region [82]. Assumptions are made that the absorbed microwave energy is converted to heating in the material with neglected surface heat loss, thermal diffusion, and energy absorbed by the oven (e.g. magnetron and cavity wall). Therefore, the energy absorbed by the material is corresponding to the temperature rise of the material, and it is expressed by re-arranging Equation 69:

$$E_{internal} = \sqrt{\frac{mC\Delta T}{2\pi f \epsilon_0 \epsilon'' \Delta t}} \quad 73$$

It should be noted that the internal electric field is only localised in the material and is different from that in the surrounding cavity. Under the same assumptions that the material is surrounded by a uniform microwave field, incident microwaves are mostly transmitted and absorbed by the material while some are reflected. It is also assumed no reflected wave at the interface. An expression is presented as follows [83]:

$$Q_{absorb}V = P_{absorb} = \rho C \frac{\Delta T}{\Delta t} V = \epsilon_0 \cdot E_{rms,external}^2 \cdot c \cdot A \cdot \xi \cdot \Gamma \quad 74$$

Where  $V$  is the volume of the material,  $\rho$  is the density of the materials,  $c$  is the phase velocity of the microwave ( $3 \times 10^8$  m/s) [84],  $A$  is the surface area,  $\xi$  is the absorption coefficient that represents the fraction of the absorbed power that generates heat, and  $\Gamma$  is the transmission coefficient. Solving the equation, the time-averaged strength of the external electric field  $E_{rms,external}$  obtained by:

$$E_{rms,external} = \sqrt{\frac{\rho C a \Delta T}{3 \Delta t c \epsilon_0 \xi \Gamma}} \quad 75$$

The power absorption coefficient  $\xi$  is expressed as follows [85]:

$$\xi = \frac{P_{absorb}}{P_0} = 1 - e^{-2a/d_p} \quad 76$$

Where  $P_0$  is the incident power at the surface, and  $a$  is the thickness of the BaTiO<sub>3</sub>-epoxy sample. The transmission coefficient,  $\Gamma$ , is the energy fluxes per unit time and unit area at the interface. It is assumed that the microwave incident is normal to the material surface as the energy flux comes from all directions within the cavity, and the transmission coefficient  $\Gamma$  is simplified as [84]:

$$\Gamma = \frac{4(n_1/n_2)}{[(n_1/n_2) + 1]^2} \quad 77$$

where  $n_1$  and  $n_2$  are the refraction index of air and the material, respectively. The above equations are employed to theoretically obtain an estimate of the average and peak electric field strengths of the incident microwave with a given cavity size. Subsequently, the absorbed microwave power by the nanocomposite has been estimated.

## 6 MATERIALS AND EXPERIMENTS

### 6.1 Materials and Fabrication

The epoxy used in this study was Araldite LY1564, a diglycidyl ether of bisphenol A (DGEBA) and the curing agent was Aradur 3487, an amine hardener, supplied by Huntsman, UK. This epoxy resin system has relatively low viscosity and high flexibility mainly for aerospace and industrial structural composites parts. It is widely observed that when the nanoparticles are added to the polymer, the nanofillers cluster and aggregate due to the “nano” effect [86]. Lijima et al. [87] successfully achieved a uniform dispersion by improving the interfacial bonding between BaTiO<sub>3</sub> nanoparticles and the epoxy matrix with the aid of 3-GPS. The coupling agent for surface functionalisation selected in this study was 3-glycidoxypropyl trimethoxysilane (3-GPS) supplied by Sigma-Aldrich, US. Hydrogen peroxide (H<sub>2</sub>O<sub>2</sub>, 30%) and acetic acid (C<sub>2</sub>H<sub>4</sub>O<sub>2</sub>, 99.9%) used as functionalisation aids were supplied by Sigma-Aldrich, US, and the ethanol (C<sub>2</sub>H<sub>6</sub>O, 99.9%) used for BaTiO<sub>3</sub> dispersion by Fisher Scientific International, Inc., UK. BaTiO<sub>3</sub> powders were supplied from Nanostructure & Amorphous Materials Inc., US. The general properties of the powders measured by the manufacture, detailed in Table 1, below [88]. All the chemicals except BaTiO<sub>3</sub> powders were used as received without further treatment.

**Table 1 General properties of BaTiO<sub>3</sub> nanoparticles [88].**

<b>Size</b>	200 nm
<b>Phase</b>	Tetragonal
<b>Specific surface area (SSA)</b>	6-7 m <sup>2</sup> /g Spherical
<b>Density</b>	5.85 g/cm <sup>3</sup>

The phase composition of BaTiO<sub>3</sub> powders has been confirmed by X-Ray diffraction (XRD) using a Siemens D5005 X-Ray Diffractometer with Cu-K $\alpha$  radiation (wavelength  $\lambda$  of 1.54 Å, at 40 kV and 30 mA). The scanning speed was 0.5°/s in the range of 20° to 90°. The peaks analysis was performed by data analysis software Origin using a Lorentzian curve fit function. Figure 6 shows a well-defined perovskite structure of BaTiO<sub>3</sub> without a noticeable second phase. The split peaks between 44°-46° of the 2 $\theta$  angle correspond to reflections (002) and (200) confirms the tetragonal phase of BaTiO<sub>3</sub> [89].

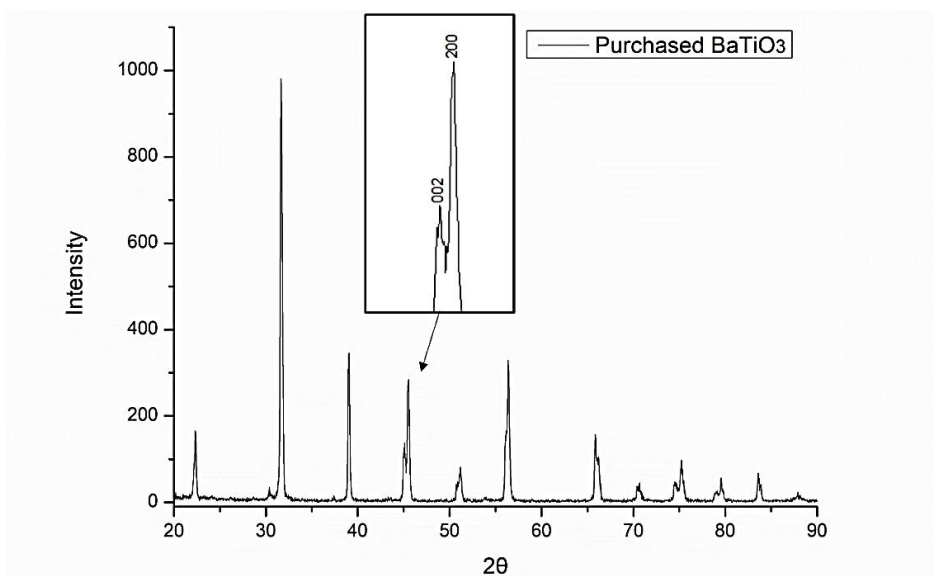


**Figure 6** X-ray diffraction patterns of purchased BaTiO<sub>3</sub> powders. The inset shows the split peaks of (002) and (200) indicating the tetragonal phase.

### 6.1.1 Surface Functionalisation of BaTiO<sub>3</sub> and Characterisation

The BaTiO<sub>3</sub> powders were prepared using combustion method, therefore, firstly they were pre-treated in H<sub>2</sub>O<sub>2</sub> for hydroxylation process to add hydroxyl group (-OH) to the surface [90]: 10g BaTiO<sub>3</sub> nanoparticles were added into a 230mL solution of H<sub>2</sub>O<sub>2</sub> in a round bottom flask. The mixture was then sonicated in an ultrasonic bath for 30 min and then refluxed at the boiling temperature of 30% H<sub>2</sub>O<sub>2</sub> solution at 108°C [91] at 100 rpm using a mechanical stirrer for six hours to facilitate the process by heating without losing H<sub>2</sub>O<sub>2</sub>. The nanoparticles were retrieved by centrifuging the resulting solution at 4500 rpm for 15 min, and washed three times with deionized water. The achieved BaTiO<sub>3</sub> nanoparticles were dried in an oven at 80°C for 24 hours. The reflux and particle retrieving processes were similar as in the surface functionalisation with 3-GPS as shown in Figure 7. 3-GPS was then applied to BaTiO<sub>3</sub> nanoparticles to improve the processability and filler dispersion in nanocomposites; the solution of 1 wt.% of 3-GPS with respect to BaTiO<sub>3</sub> was prepared. 150mL aqueous solution of ethanol and deionized water (9:1) was firstly mixed in a beaker. Adding the acetic acid drops using a pipette and stir vigorously after each drop until the pH value of 3.5-4 measured by a METTLER TOLEDO pH meter was reached, stirred vigorously again for 3mins to form a clear solution. The low pH values of the solution facilitate the silane functionalisation process [92]. After the addition of the 0.1g 3-GPS solution to the acidified solution using a pipette, the mixture was left in an ultrasonic bath for 30mins to form a homogenous solution. 10g hydroxylated BaTiO<sub>3</sub> powders was then added to the silane solution, and mixed under ultrasonic bath for 10mins for better filler wetting. Finally, the mixture was refluxed at the boiling temperature of ethanol, 78°C [93], at 100 rpm using a mechanical stirrer for six hours using a silicone oil bath over a hotplate. After refluxing, the BaTiO<sub>3</sub> was washed three times with deionized water and retrieved using centrifugation at 4500 rpm. The silane treated BaTiO<sub>3</sub> (Si-BaTiO<sub>3</sub>)

powders were dried at 110°C for 24 hours to avoid any condensation of silanol groups at the surface. In the end, the powders were crushed in a mortar and pestle for the nanocomposites preparation. The size distribution of Si-BaTiO<sub>3</sub> particles was analysed in its epoxy nanocomposite form.

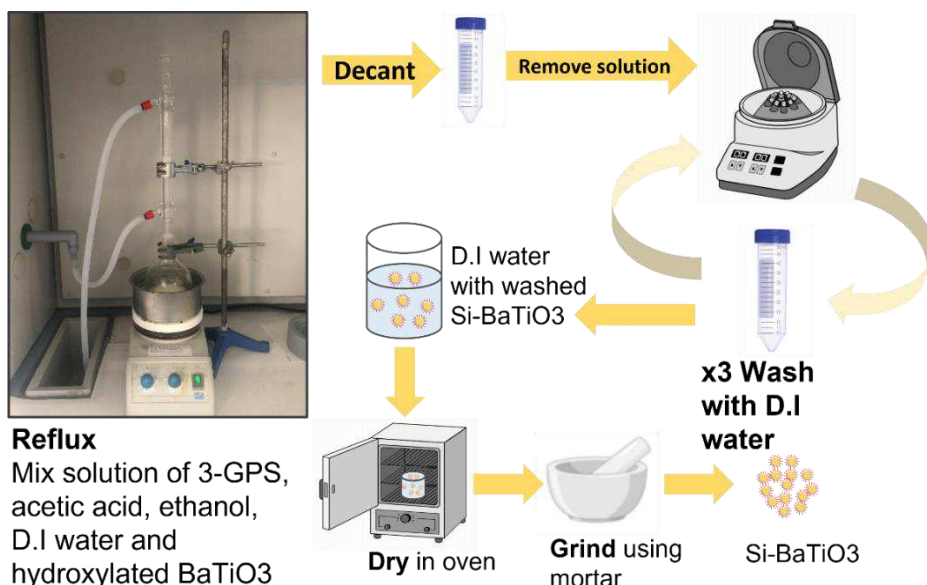


**Figure 7** Schematic diagram of the functionalisation process of BaTiO<sub>3</sub> with 3-GPS.

The silane-treated powders were characterised by Thermogravimetric analysis (TGA) and Fourier transform infrared (FTIR) spectrometry to confirm the presence of the functional group in the following sections.

#### 6.1.1.1 Fourier Transform Infrared (FTIR) Spectrometry

FTIR is performed to detect the silane functional groups on the modified BaTiO<sub>3</sub> powders in transmission mode using a Jasco FT/IR-6200 in the range of 400-4000 cm<sup>-1</sup> with a resolution of 2 cm<sup>-1</sup> at room temperature. The FTIR spectra of Si-BaTiO<sub>3</sub> and untreated powders are presented in Figure 8. The peaks at 1437 cm<sup>-1</sup> and 1630 cm<sup>-1</sup> are due to the small trace of BaCO<sub>3</sub>, and physically absorbed water on BaTiO<sub>3</sub> powders from the combustion fabrication process according to the manufacturer [94]. The bands at 3200-3700 cm<sup>-1</sup> are attributed to hydroxyl groups OH (from Si-OH group) stretching vibrations. The bands between 850 cm<sup>-1</sup> and 1250 cm<sup>-1</sup> are representations of Si-O, Si-O-C<sub>2</sub>H<sub>5</sub>, and Si-O vibrations. These new peaks confirm that the silane group are successfully grafted onto the surface of BaTiO<sub>3</sub> powders [95].

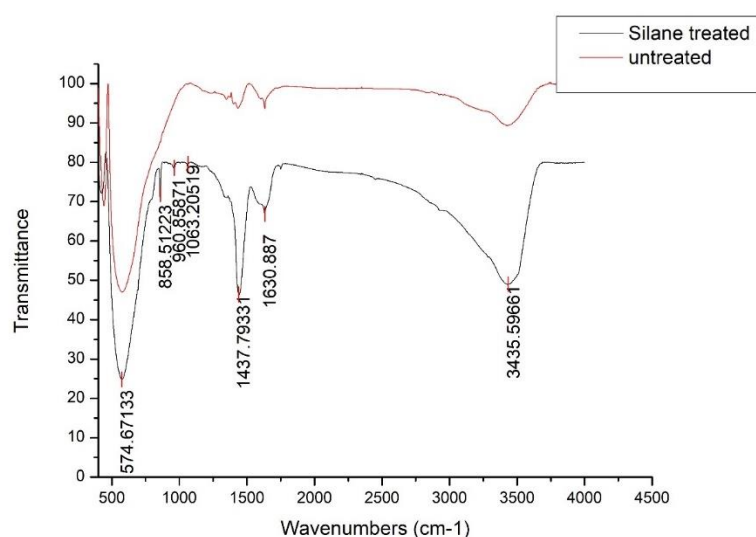


**Figure 8** FTIR spectra of Si-BaTiO<sub>3</sub> (black) and untreated (red) BaTiO<sub>3</sub> powders.

### 6.1.1.2 Thermogravimetric Analysis (TGA)

The amount of organic silane group grafted onto the surface of BaTiO<sub>3</sub> powder was obtained by TGA using a TA instruments Q-500 at a rate of 20°C/min under a dry nitrogen gas flow rate of 100 ml/min to 700°C, shown in Figure 9 for untreated and Si-BaTiO<sub>3</sub> powders. The weight loss percentage indicated as the lowest point of the green line is 0.35% of untreated BaTiO<sub>3</sub> and 1.2% for treated. Therefore, the amount of 3-GPS grafted onto the BaTiO<sub>3</sub> surface was calculated to be approx. 0.85%, which is close to the previously designed 1% in the surface functionalisation process. The weight curve of 3-GPS treated BaTiO<sub>3</sub> powders showed three well-defined degradations as labelled in the figure. Based on the FTIR results, the absorbed water is removed between 50°C to 150°C, 1 and 2 in the figure. The degradation step from 240°C to 450°C represents the free hydroxyl groups (-OH) and/or silane molecules that remained on the surface, labelled as 3. The pyrolysis of surface silane compounds was observed at around 565°C, labelled as 4 [94, 96].

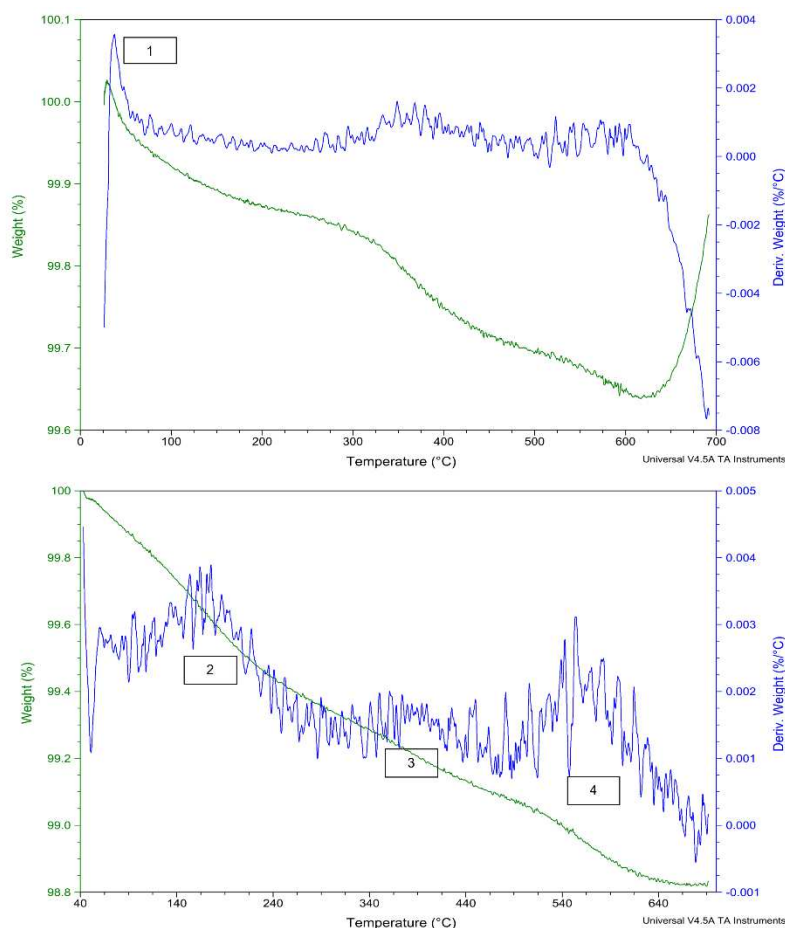


**Figure 9** TGA curves of untreated and Si-BaTiO<sub>3</sub> powders. Green lines indicate the weight percentage of the powders versus temperature, and blue lines the rate of change of the weight percentage versus temperature.

### 6.1.2 Fabrication of BaTiO<sub>3</sub> Nanocomposites

The epoxy nanocomposite fabrication process including Si-BaTiO<sub>3</sub> functionalisation is schematically illustrated in Figure 10. The epoxy resin nanosuspension with 1, 5, 10, 15 wt.% Si-BaTiO<sub>3</sub> nanoparticles and 5, 10, 15 wt.% untreated BaTiO<sub>3</sub> nanoparticles are prepared as follows: Firstly, the weighed amount of BaTiO<sub>3</sub> powders was added to ethanol and sonicated with an ice water bath for 2 min with a 10s pulse to form a homogenous solution. Then a weighed amount of epoxy and the previous mixed solution were blended in a beaker using a mechanical stirrer at 300 rpm and 80°C overnight under the fume hood to gradually remove the ethanol without precipitation of the particles. The mixture was weighed before and after the previous step to ensure the complete removal of ethanol. The curing agent was then added to the mixture with a weight ratio recommended by the company and stirred for a further 3mins. Finally, the

mixture was placed in the vacuum oven at 30°C for 1 hour to remove bubbles at 29 inHg and achieve complete removal of ethanol. The whole mixture was poured into a mould made of two pieces of glass clamped with a 3 mm silicone gasket in-between, as shown in Figure 11. A uniform thickness of each sample was achieved with the assistance of this type of glass mould. They were then cured in the oven for 8 hours at 80°C as prescribed by the manufacturer, then cooled down to room temperature. The final samples were of size 160×140×3 mm<sup>3</sup>, and cut to different sizes using a precision cut-off machine BRILLANT 220.

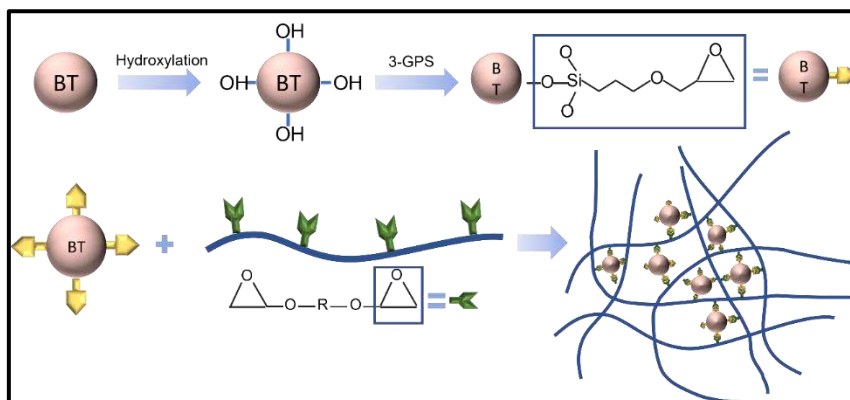


**Figure 10** Schematic illustration of the hydroxylation and silane functionalisation process for the BaTiO<sub>3</sub> nanoparticles.

	Epoxy/g Hardener/g	Ethanol/mL	BaTiO <sub>3</sub> /g
Neat Epoxy	40 13.6	/	/
1 wt.% Si-BT		15	0.536
5 wt.% Si-BT		15	2.68
10 wt.% Si-BT		15	5.36
15 wt.% Si-BT		15	8.04
10 wt.% BT		15	5.36
15 wt.% BT		15	8.04

**Figure 11** Glass mould used for nanocomposite fabrication and the cured nanocomposite samples.

## 6.2 Field Induced Experimental Methods

### 6.2.1 General Material Characterisations

The morphological characterisation of the nanocomposites, post cure, with different weight loading between 0wt.% and 15wt.% were carried out using a field emission scanning electron microscope TESCAN Vega 3. A thin layer of gold is coated to each sample before testing to enable better conductivity. The thermal characterisation of the cured nanocomposites was studied using a differential scanning calorimeter (DSC Q200, TA Instruments). The DSC measurements were performed in a nitrogen flow (50 mL/min). Samples

5×3×1 mm<sup>3</sup> were prepared using a Buehler ISOMAT low speed saw. The samples were first heated from 40°C to 220°C at 20°C/min. The measured DSC curves of all epoxy nanocomposites presented a distinct exotherm peak. Thereafter, the second run at a heating rate of 20°C/min was conducted up to 220°C after cooling down from the first scan. The glass-transition temperature ( $T_g$ ) was determined using the inflection-point method following the IS/DIS 11357-2. A tangent was drawn at the point of inflection in the DSC spectra from the second run, and the  $T_g$  was the midpoint between onset and end-set of the drawn tangent.

The complex relative permittivity and permeability of the neat epoxy and the nanocomposites at different weight loading were measured with increasing frequency from 0.25 GHz to 4.50 GHz at a 0.25 step increment using a vector network analyser (VNA) with microstrip methods [97]. Flat plates samples of size 50×50×3 mm<sup>3</sup> were prepared as substrates for conductive lines as shown in Figure 12. They were then attached to a ground metal plate at the bottom. The dielectric constants of the samples were then measured using the VNA. The resonant approach can provide a more accurate values of the dielectric properties compared with the transmission line method. However, the resonant methods could only measure the dielectric properties at a single frequency instead of measuring in the frequency range [98].



**Figure 12** Schematic illustration of the layout of sample for microstrip line methods.

### 6.2.2 Field-induced Strain Measurements

The microwave field was selected to be the external stimulator as BaTiO<sub>3</sub> exhibit a peak in a dielectric loss at the microwave frequency range. Most importantly, the design of the experiment becomes more feasible with remote stimulation from the microwave field owing to the spacious cavity. The mechanical strain evolution in the nanocomposite was investigated under a microwave field within a temperature-controlled microwave cavity Panasonic NN-SF464MBPQ running at 2.45 GHz and cavity size of 354×338×230 mm<sup>3</sup>. In contrast with the conventional one, this oven, equipped with inverter technology, has a circuit board that replaces the transformer, hence the output power can be adjusted linearly by varying the pulse width to ensure a more precise and continuous microwave exposure [99]. The unique flat-bed design of this model is equipped with a stationary ceramic plate that allowed more space to place the sample and its holder.

The strain field introduced by the BaTiO<sub>3</sub> nanoparticles to the surrounding epoxy, activated by microwave field, was studied by real-time strain measurements on the surface of the nanocomposite samples with the incorporation of Fibre optic sensors utilising fibre Bragg gratings (FBG) technique. The sensors were placed apart in equal distance from one another within a 90mm straight line. This is theoretically aligned with the microwave's half wavelength (~60mm) as also was experimentally observed during real-time temperature measurements. The sensors were located to ensure overlapping with at least three nodes and antinodes of the microwave cycle. The FBG sensors were fabricated by a periodic intense laser light applied onto the core of an optic fibre. The laser light exposure introduced a permanent increase in the refractive index of the fibre's core and a fixed modulation was created subsequently. Each FBG was approx. five mm long with a grating period of one micron. Two arrays with three FBGs for each sample were fabricated. FBG arrays were then adhesively bonded to the surface of two geometrically identical 135×10×3 mm<sup>3</sup> samples made of Si-BaTiO<sub>3</sub> epoxy nanocomposites. The strain array was bonded to the surface by adhesives at the FBG regions while the temperature array is firstly packaged into a capillary glass tube, and then bonded parallel to the strain array. The arrays were placed at the same location with the same distance in-between. The strain experienced by the samples was transferred to the FBG sensors, and the

measurements were also affected by the temperature. Therefore, the temperature array only measured the temperature change, and compensated the strain measurements accordingly.

A preliminary test via a FLIR One Pro LT Thermal Camera was carried out to inspect the temperature change in different samples under different microwave power levels. Samples were placed at a designed location as shown in Figure 13. The exposure time was then carefully selected based on the heating profiles of each sample to control the temperature of samples well below  $T_g$  during the exposure to avoid any interference in strain measurements from the post-cure shrinkage. The sample was clamped on one end by a designed sample holder made of polytetrafluoroethylene (PTFE) to ensure minimum interaction with the microwave field owing to its extremely low dielectric loss. The size and location of the load inside the cavity were two primary factors that affect the microwave field distribution [99]. To control the microwave field distribution, the sample and the holder were placed at the designed location shown in the figure, for all tests. The power level of 100W and 440W were initially selected to avoid temperature surges in samples within a short period of time. Exposure time was set to be 650s for 100W and 148s for 440W to limit the temperature below  $T_g$  (80°C) based on the preliminary results obtained by the thermal camera.

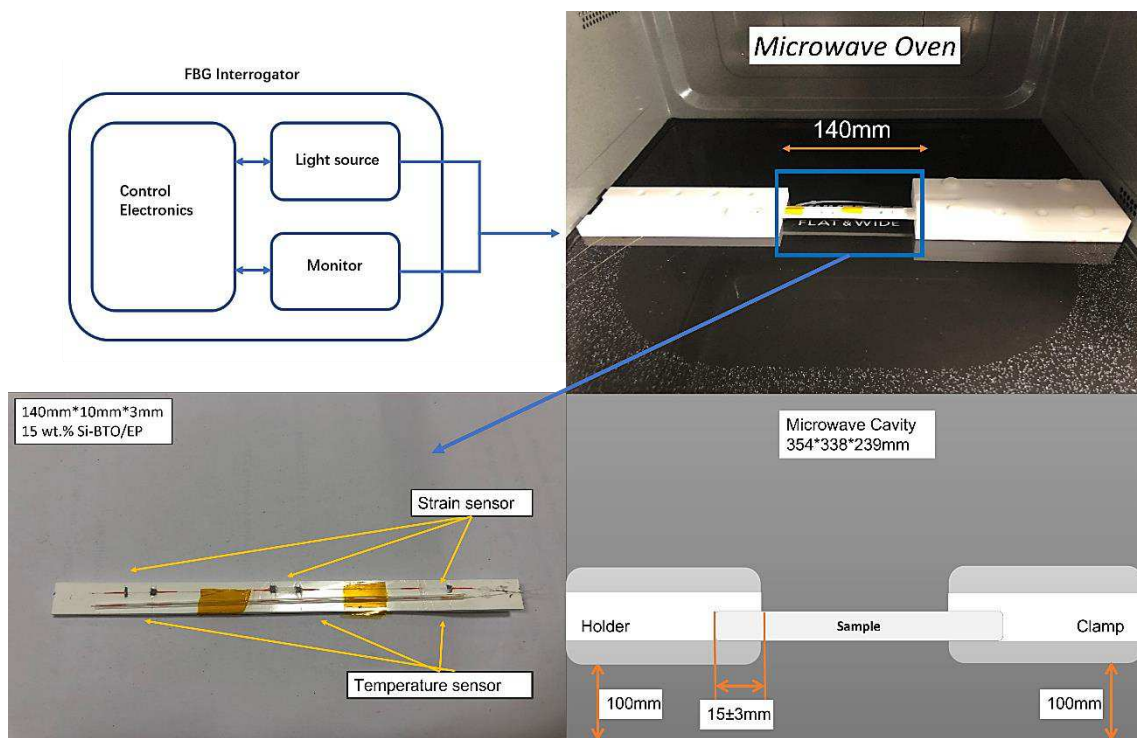


**Figure 13** Schematic illustration of the sample of epoxy nanocomposite with BaTiO<sub>3</sub> on the PTFE holder in the microwave oven with surface bonded FBG arrays connected to an interrogator.

Neat epoxy, BaTiO<sub>3</sub> nanoparticles, and adhesive used for bonding FBGs possess different thermal expansion coefficients (CTE) and microwave heating patterns. Microwave field interaction with the neat epoxy and adhesive have been investigated, thereafter. Two arrays with five FBGs of five mm long and one micron grating period were fabricated for each test. First, the adhesive response under microwave radiation was studied by two arrays of FBGs adhesively bonded to the surface of a PTFE block. It is assumed that measured strain and temperature change are solely due to the microwave heating of adhesive as PTFE has neglectable thermal response (temperature rise) under the microwave. The PTFE block is placed in the microwave oven at the designed location to locate the first FBG sensor on the left end at the same location as the one in the previous exposure on the nanocomposites. The tests have been performed under 100W for 650s and 440W for 110s. Data was recorded on the interrogator 10s prior to the microwave exposure for each run to ensure no data is missing after the microwave starts. The effect of neat epoxy with the FBG sensors bonded to its surface was investigated as a controlled group to the test of 15 wt.% nanocomposites at 10 W for 600s and 440W for 60s. Neat epoxy sample geometrically identical with 15 wt.% nanocomposites in the nanocomposite's exposure test was placed in the designed location with surface-

bonded arrays of FBGs. The whole measurements from adhesive and the neat epoxy were compared with the results from the previously performed test on the nanocomposites for better distinguishing the BaTiO<sub>3</sub>-epoxy nanocomposite's response to the microwave exposure.

### 6.2.3 Raman Spectroscopy

Raman characterisation was carried out to investigate residual stress, any indication of remnant strain field or crystal structure change in BaTiO<sub>3</sub> nanoparticles embedded epoxy post microwave exposure. Neat epoxy samples and 15 wt.% BaTiO<sub>3</sub> epoxy nanocomposites with the identical geometric dimension of 135×10×3 mm<sup>3</sup> were characterised before and after 440W microwave radiation of 110s. The Raman spectra were obtained using a Raman spectroscope Horiba Scientific LabRAM HR with a 514 nm excitation wavelength laser for all samples.

## 7 RESULTS

### 7.1 General Material Characterisations

#### 7.1.1 Scanning Electron Microscope (SEM)

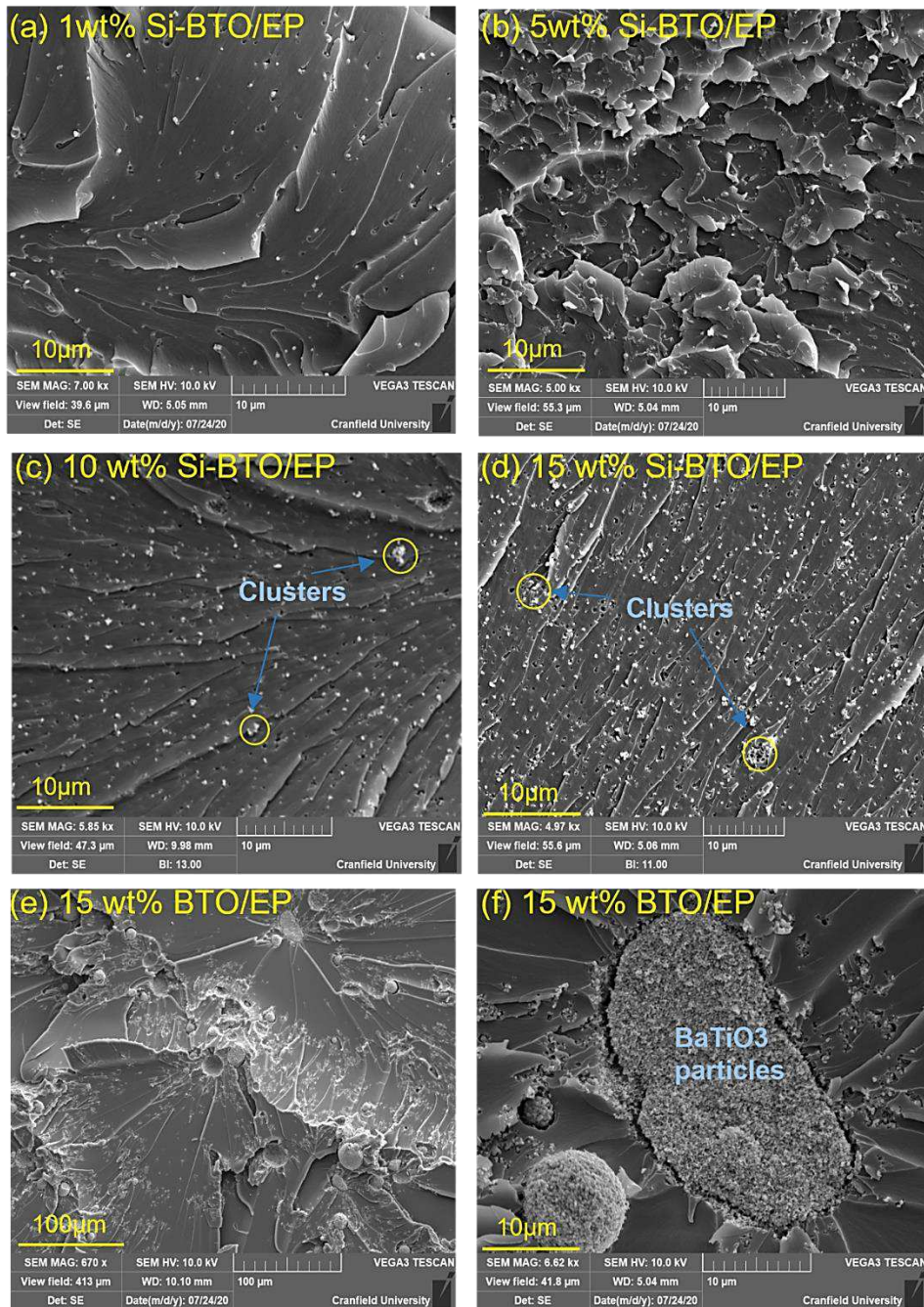
A silane coupling agent 3-GPS was introduced to modify the BaTiO<sub>3</sub> particles in this work to achieve a finer dispersion in epoxy. To examine its effectiveness, the dispersion and distribution of the nanoparticles at epoxy with different loadings have been characterised using the SEM. Different levels of aggregation events due to increased weight fraction of particles and enhancement of distribution due to surface functionalisation were present:

Figure 14(a)-(f) presents the SEM images of the fractured cross-section of the silane functionalised and non-functionalised BaTiO<sub>3</sub> epoxy composites at various wt.%. It is shown that the nanoparticles are uniformly dispersed with the aid of surface functionalisation. As shown in Figure 14(a), the silane-treated particles are of the similar size of 200 nm as pristine BaTiO<sub>3</sub> particles. There is no apparent aggregation of Si-BaTiO<sub>3</sub> particles until small-scale clusters become visible in Figure 14(c) and Figure 14(d) when the loading of BaTiO<sub>3</sub> reaches 10 wt.% and over, due to nanofillers agglomeration as circled in Figure 14(c) and Figure 14(d). Overall, the majority of the Si-BaTiO<sub>3</sub> particles were finely dispersed compared with the untreated ones. Figure 14(e) and Figure 14(f) show images of the composites with 15 wt.% non-functionalised BaTiO<sub>3</sub> particles at different magnification. In contrast with the functionalised BaTiO<sub>3</sub> at the same weight loading 15 wt.% shown in Figure 14(d), the 15 wt.% untreated BaTiO<sub>3</sub> exhibit severe agglomeration to form large clusters that have left large-scaled lamellar structures. The efficacy of the silane functional group is in good agreement with works conducted by others [87, 100, 101].

#### 7.1.2 DSC

The DSC was conducted to examine the effect on curing extent and  $T_g$  of cured epoxy nanocomposites with varying weight fractions of Si-treated and untreated BaTiO<sub>3</sub> nanoparticles.

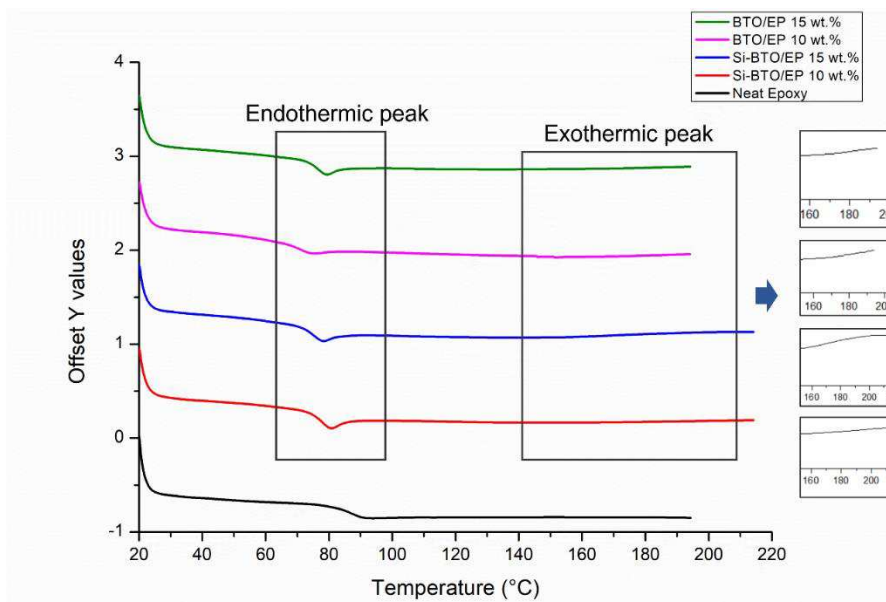
Figure 15 shows the DSC spectra of the neat epoxy and nanocomposites at various BaTiO<sub>3</sub> content. As observed from the insets, the DSC spectra of epoxy nanocomposites exhibit small *bumps* denoted as exothermic peaks representing the post-curing process due to the impeded curing by the existence of BaTiO<sub>3</sub> nanoparticles. The  $T_g$  transition for the coloured lines that represent nanocomposites are shifted slightly to lower temperatures compared with the black line of neat epoxy which is evidence of reduced  $T_g$  as the nanoparticles hindered the curing process of the epoxy resin [102]. Furthermore, the weak endothermic peaks that emerge on the spectra represent the relief of the stress introduced during processing and handling or the thermal history. The thermal history and residual stress were removed from the first run of heating and the samples were post-cured during the first DSC analysis up to 200°C. The true  $T_g$  of each cured nanocomposite sample was calculated based on the DSC spectra of a second run under the same condition.



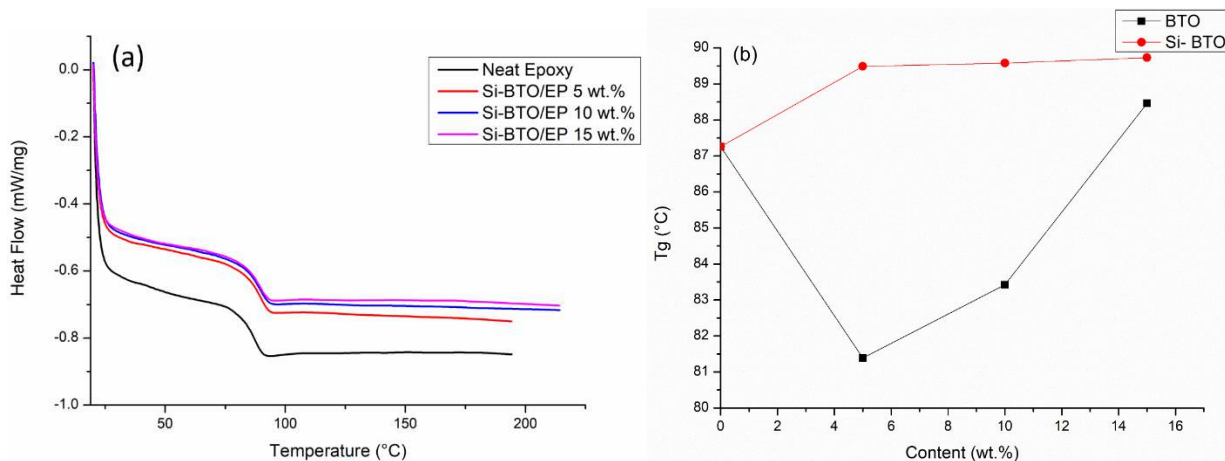
**Figure 14** SEM images of fracture cross of epoxy nanocomposites with BaTiO<sub>3</sub> at different weight loading, (a)-(d) images of 1 wt.%, 5 wt.%, 10 wt.% and 15 wt.% Si-BaTiO<sub>3</sub>/Epoxy nanocomposite samples. (e) and (f) 15 wt.% untreated-BaTiO<sub>3</sub>-epoxy nanocomposite at lower (670x) and higher (6620x) magnification.

Figure 16(a) presents the DSC spectra of a second heating scan for each epoxy nanocomposite with functionalised BaTiO<sub>3</sub> after cooling down from the 220°C previous runs. It can be observed that epoxy nanocomposites are well cured without any perceptible exothermal peak. The red and black lines are drawn as a demonstration of  $T_g$  variation along with the weight fraction of the nanofiller. The red line shows a gradual increase of  $T_g$  with the increasing Si-BaTiO<sub>3</sub> content. The  $T_g$  has increased up to 90°C compared with that of the neat epoxy, 87°C, as shown in Figure 17. The increased  $T_g$  represents that more energy is needed from higher temperatures to complete the glass transition process, which indicates that the movement of polymer chains is inhibited by the functionalised BaTiO<sub>3</sub> nanoparticles due to improved interfacial bonding. However, by adding the non-functionalised BaTiO<sub>3</sub>, the  $T_g$  shows a remarkable drop at 5wt.% at the beginning as marked by a black line in Figure 16(b). When the weight loading reaches 10wt.%,

the  $T_g$  shows an increment surge from 81°C to 84°C. The  $T_g$  of the nanocomposites reaches 89°C at 15wt.%. Although the particles obstruct the formation of the cross-linking structure of epoxy during the curing process [103, 104], the increased  $T_g$  of Si- BaTiO<sub>3</sub>/Epoxy nanocomposites at higher weight loading (5 wt.% and over) are attributed to the better interfacial bonding and enhanced mobility of the segment due to increased free volume between the BaTiO<sub>3</sub> particles and the epoxy matrix [104, 105]. For the case of non-treated BaTiO<sub>3</sub>, it is noted that the  $T_g$  results follow a similar pattern with increasing loading of the particles despite the overall values are below the neat epoxy's  $T_g$ . This result also supports the proposed explanation of enlarged free volume surrounding the particles. Non-treated nanoparticles tend to agglomerate as shown previously in the SEM images. These large-scale aggregations further inhibit the cross-linking polymer, having led to a reduced  $T_g$  below the epoxy one.



**Figure 15** DSC spectra of neat epoxy and nanocomposites with 10 wt.% and 15 wt.% of untreated BaTiO<sub>3</sub> (pink and green) and Si-BaTiO<sub>3</sub> (red and blue). Weak endothermic peak around  $T_g$  and weak exothermic peak from 160°C - 220°C are identified.



**Figure 16** (a) DSC spectra of the neat epoxy (black) and Si-BaTiO<sub>3</sub>/Epoxy nanocomposite samples at 5 wt.% (Red), 10 wt.% (Blue), and 15 wt.% (Pink), (b)  $T_g$  temperature as a function of weight loading of Si-BaTiO<sub>3</sub> (Red) and untreated BaTiO<sub>3</sub> (Black) of the epoxy nanocomposites samples.

Glass Transition Temperature (T <sub>g</sub> )/°C	
Neat Epoxy	87
1wt. % Si-BT	84
5wt. % Si-BT	89
10wt. % Si-BT	90
15wt. % Si-BT	90
5wt. % BT	81
10wt. % BT	84
15wt. % BT	89

**Figure 17** Glass transition temperatures of silane treated and untreated BaTiO<sub>3</sub>/Epoxy nanocomposites.

### 7.1.3 Dielectric Properties of BaTiO<sub>3</sub>/Epoxy Composites

The microwave dielectric properties of the epoxy nanocomposites were investigated from 0.25 GHz to 4.50 GHz at a 0.25 step increment using a VNA PNA-X N5245A via a stripline technique at room temperature. The real permittivity  $\epsilon'$  and dielectric loss tangent  $\tan \delta$  at room temperature are shown in Figure 18.

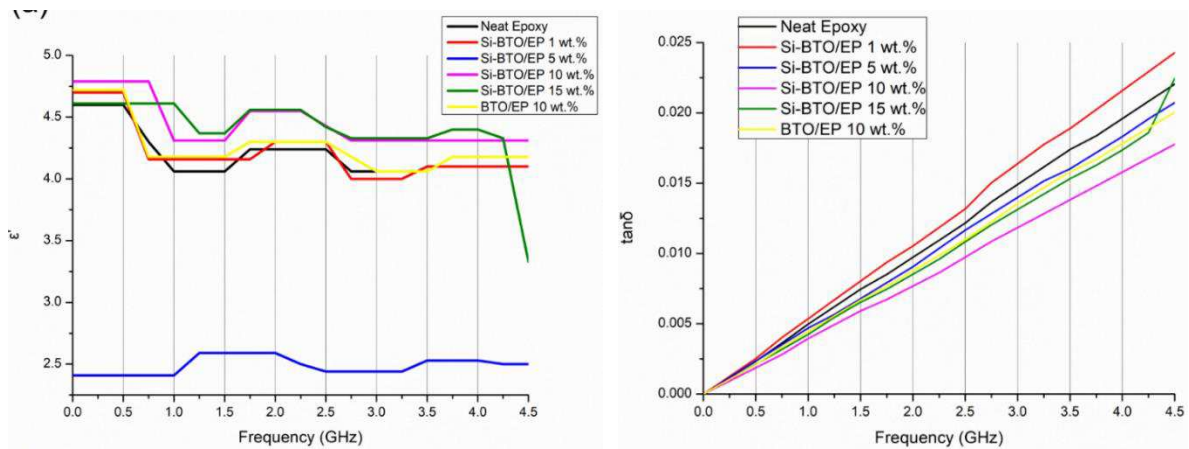


**Figure 18** Dielectric measurements (a) real permittivity  $\epsilon'$ , (b) loss tangent  $\tan(\delta)$  from 0 to 4.5 GHz at room temperature of neat epoxy and BaTiO<sub>3</sub>-Epoxy nanocomposites at different weight loading.

The  $\epsilon'$  of all samples over the measured frequency range have slight reduction trends with increasing frequency due to the dipoles in the material that cannot follow the speed of the alternating field and reorient themselves with the field direction [104]. Compared with neat epoxy, the inclusion of Si-BaTiO<sub>3</sub> nanoparticles at 10 wt.% and 15 wt.% give a perceptible rise to the value of  $\epsilon'$  through the frequency range, which are similar results as reported in other studies [106-108]. In the meantime, the 1 wt.% and non-treated 10 wt.% BaTiO<sub>3</sub>/Epoxy samples present similar values of  $\epsilon'$  with the neat epoxy due to little amount of BaTiO<sub>3</sub> of 1 wt.% and aggregations of unfunctionalized 10 wt.% [108]. The silane treated samples have higher values in  $\epsilon'$  due to a more uniform dispersion of BaTiO<sub>3</sub> nanoparticles [106, 107, 109]. However, there aren't huge differences between the values of  $\epsilon'$  at 10 wt.% and 15 wt.%. As discussed formerly, the ferroelectricity character of tetragonal BaTiO<sub>3</sub> enables a spontaneous polarisation that can be reversed by an applied field [110]. Therefore the  $\epsilon'$  of epoxy is enhanced due to the addition of BaTiO<sub>3</sub> nanoparticles, which agrees with the findings from other researches [106, 107, 109, 111]. Generally speaking, a substantial increase in the dielectric properties of modified epoxy is only achieved by a generous amount of BaTiO<sub>3</sub> content as high as 90 wt.% [112]. The blue line that represents the dielectric response of 5 wt.% silane-treated BaTiO<sub>3</sub> epoxy nanocomposites, presents a significantly lower value of real permittivity  $\epsilon'$  below the neat epoxy's. This drastic decline in the value of  $\epsilon'$  could be attributed to testing errors from air gaps between the sample and conductive line [113]. Figure 18(b) illustrates that the loss tangent in all samples increases with increasing frequency. On the contrary with the real permittivity, the loss tangent has slightly decreased with adding BaTiO<sub>3</sub> powders except from 1wt.% content. The loss tangent of a composite system has contributions from dipole orientation, conduction loss and interfacial polarisation [114]. Silane treatment of the BaTiO<sub>3</sub> powders introduce a reduction of the concentration of ionizable

hydroxyl groups (-OH) on the BaTiO<sub>3</sub> surface and hinders the mobility of the charge carriers on the surface. The lowered conduction loss could be the primary reason for lowered loss tangent [95].

## 7.2 In-situ Strain Response under Microwave at Different Power Levels.

### 7.2.1 100W and 440W Microwave Exposure Power

Labelling for strain and temperature FBG arrays is illustrated in Figure 19. Field-induced strains in the nanocomposites with 15 wt.% BaTiO<sub>3</sub> (the highest wt.% examined) has been investigated within a microwave exposure at 100W and 440W (Figure 20 and Figure 21, respectively) in the three specimens which exhibited nearly similar trends and magnitude (one data presented in the figures in the interests of clarity). The evolution of strain and temperature have been measured *in situ* by the two arrays; one array measures the strain while the other one measures the temperature. Sudden drastic fluctuations and absent data presented in Figure 20 and Figure 21 are due to Bragg wavelengths moving into adjacent spectral windows that were set up on the sensor interrogator.

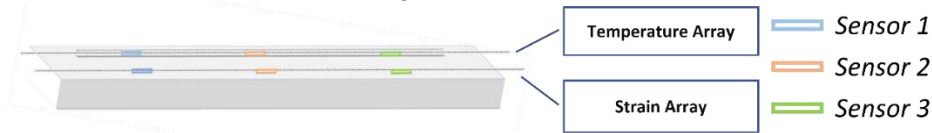


**Figure 19** Schematic illustration of surface-bonded FBG arrays measuring in-situ temperature and strain.

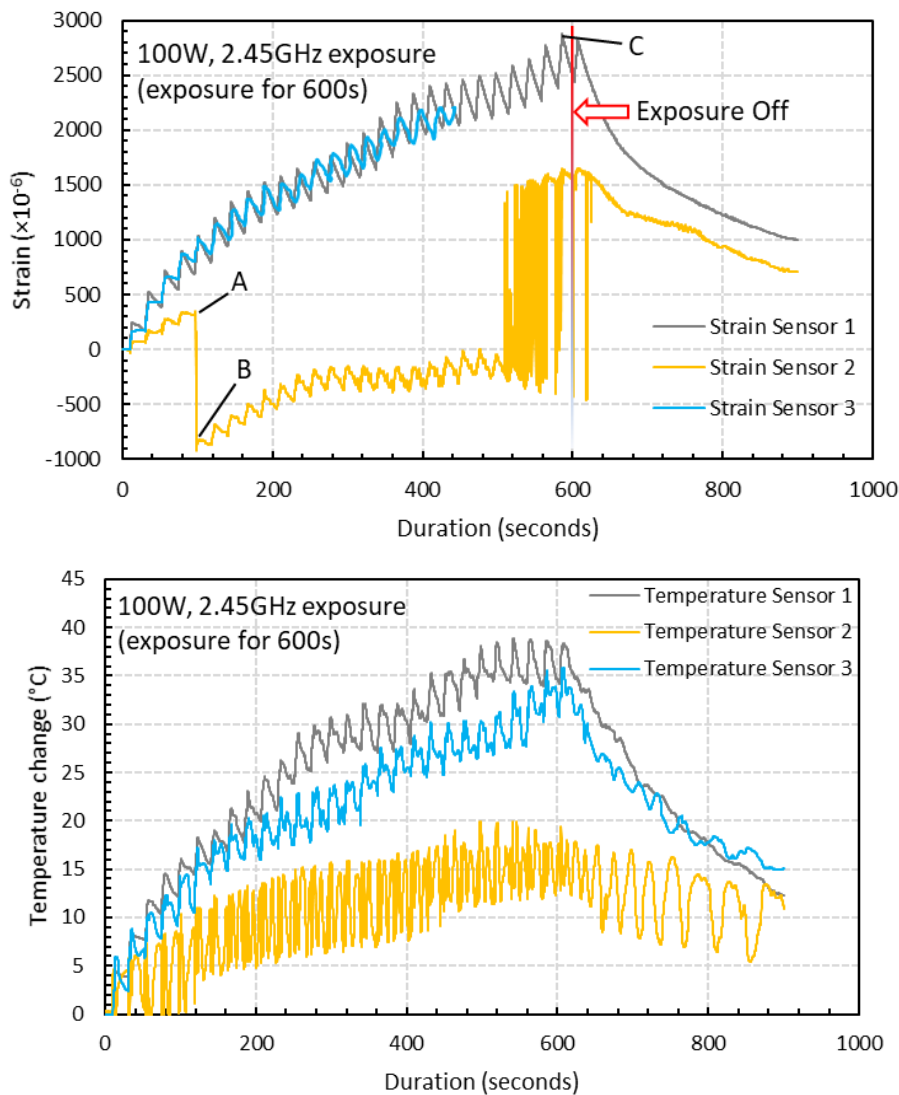


**Figure 20** Strain and temperature change measurements of 15 wt.% silane-treated BaTiO<sub>3</sub>/Epoxy samples under 100W for 600s.

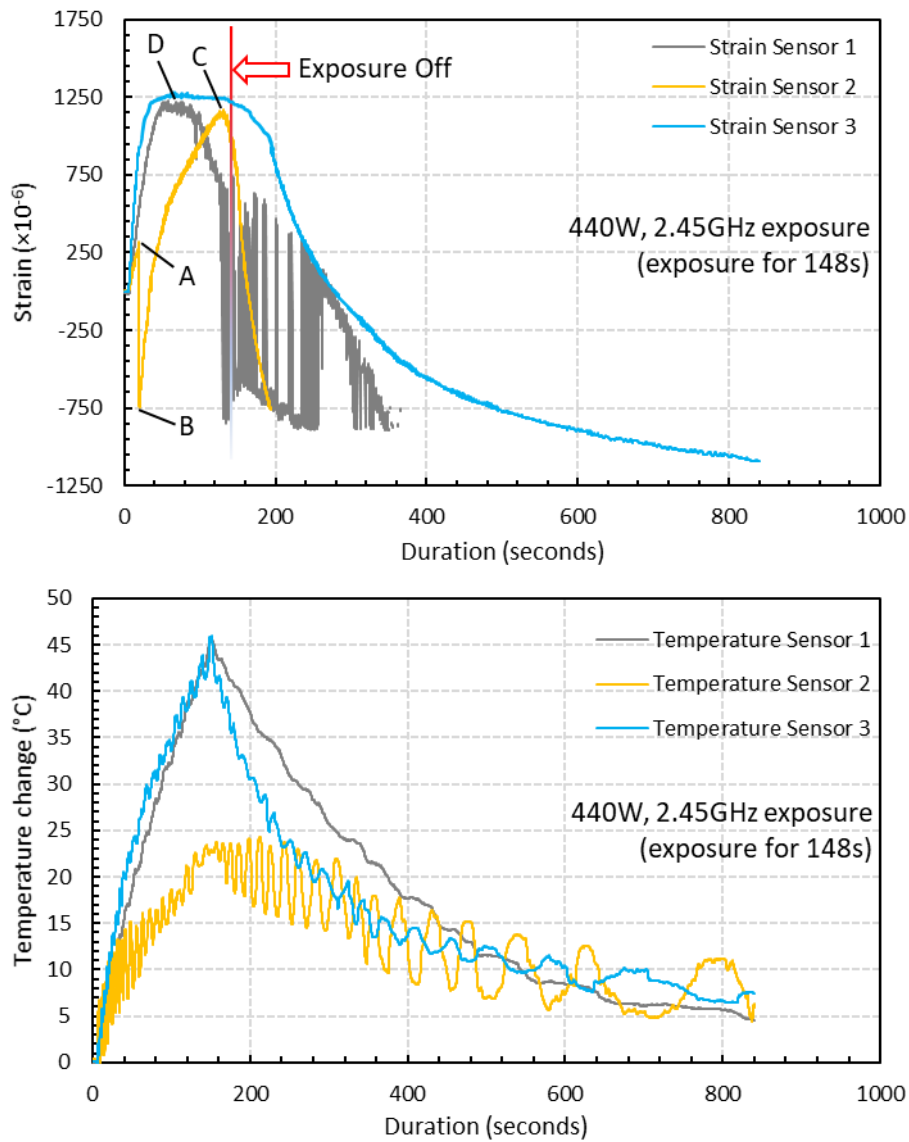


**Figure 21** Strain and temperature change measurements of 15 wt.% silane-treated BaTiO<sub>3</sub>/Epoxy samples under 440W for 148s.

The strain and temperature data exhibit a general increasing trend with the exposure. They drop gradually, immediately, after the microwave stopped. The temperature appeared to be higher at both ends of the specimen (sensor 1 and 3, located left and right respectively) compared to the middle (sensor 2), which is in accordance with the 'hot spot' theory due to microwave nonuniformity as illustrated in Figure 22. Sensors 1 and 3 data also follows more similar temperature increasing trend (magnitude and rate). The microwave oven cavity is designed to be a multimode resonant cavity, similar to a closed waveguide. The microwaves generated by the magnetron are reflected back and forth by the metal walls inside the cavity and eventually forms standing waves throughout the cavity's volume as illustrated in Figure 22 [115]. The illustration is accompanied by a thermal image captured from the sample under the microwave, showing the approximate locations of the nodes and anti-nodes. As seen, the anti-nodes (hot spots) are located at or surrounding the sensors. Under microwave exposure, the distance between the area with higher temperature (antinodes) and the cold spot with lower temperature (nodes) is a quarter of the wavelength, which is approximately 31 mm [116]. The sensors have been positioned equal distances apart, and accordingly, they fell in different temperature zones under the standing waves, identified schematically in the figure (assuming that the far-left edge of the sample represents a node).

The strain measured from a FBG sensor is derived from the change in the wavelength of reflected ultraviolet light due to grating period change. The change with strain and temperature is expressed by [117]:

$$\frac{\Delta\lambda}{\lambda_0} = k \cdot \varepsilon + \alpha_\delta \cdot \Delta T \tag{78}$$

where  $\Delta\lambda$  is wavelength shift,  $\lambda_0$  is the base wavelength,  $k = 1 - p$ ,  $p$  is the photo-elastic coefficient,  $p = 0.22$ ,  $\varepsilon$  is the strain due to both mechanical and thermal factors,  $\Delta T$  is the temperature change, and  $\alpha_\delta$  is the change of the refractive index. As expressed in Equation 78, the measured data from the strain sensor are a combination of two factors. The first part is the actual strain of the material including any mechanical strain and strain due to temperature changes. The second part is the wavelength shift due to a change in the glass-refractive index of optical fibre with temperature. According to the FBG sensors manufacturer, 1°C temperature variation induced strain of optical fibre itself is approximately equivalent to eight micro-strain. Under the 100W and 440W, the strain measured at the beginning of the microwave radiation in strain sensors 1 and 3 have similar trends of increasing as predicted when the temperature sensors 1 and 3 measurements have close gradients, having higher temperatures than that measured by sensor 2. A sudden drop in the strain measurements of the middle sensors (strain 2) can be observed in both cases soon after the initial surge, labelled as A-B. It instantaneously alters the strains by nearly identical 1162 and 1008 micro-strains (difference between A and B) under 100W and 440W, respectively. Such decline in the strain measurements is the evidence of an immediate development of a compressive strain in response to the microwave exposure, as hypothesised in section 2. Note that sensor 2 temperature is the lowest amongst the three sensors, in which the thermally induced strain is negligible. Such phenomenon could not be associated with the temperature rise since the temperature change is approximately 12°C and 5.7°C from room temperature 19°C when the sudden drop occurs at point A, which is remarkably lower than 170°C when post-curing shrinkage is introduced as indicated by the exothermic peak in the DSC spectra in Figure 15, and lower than the  $T_g$  to have any detrimental effect. Moreover, it is observed that unloading the specimen from the 440W exposure results in a residual compressive strain in all sensors' locations. This occurs after the high non-linear variation of strains in the case of 440W, unlike the linear strain behaviour under 100W. This is analogous to mechanical field introduction in which unloading an elastic-plastic specimen beyond its elastic regime under tensile loading may introduce a compressive residual strain distribution depending on the hardening behaviour (i.e. kinematic or isotropic). Further investigation was conducted on the phenomena observed, described as follows:

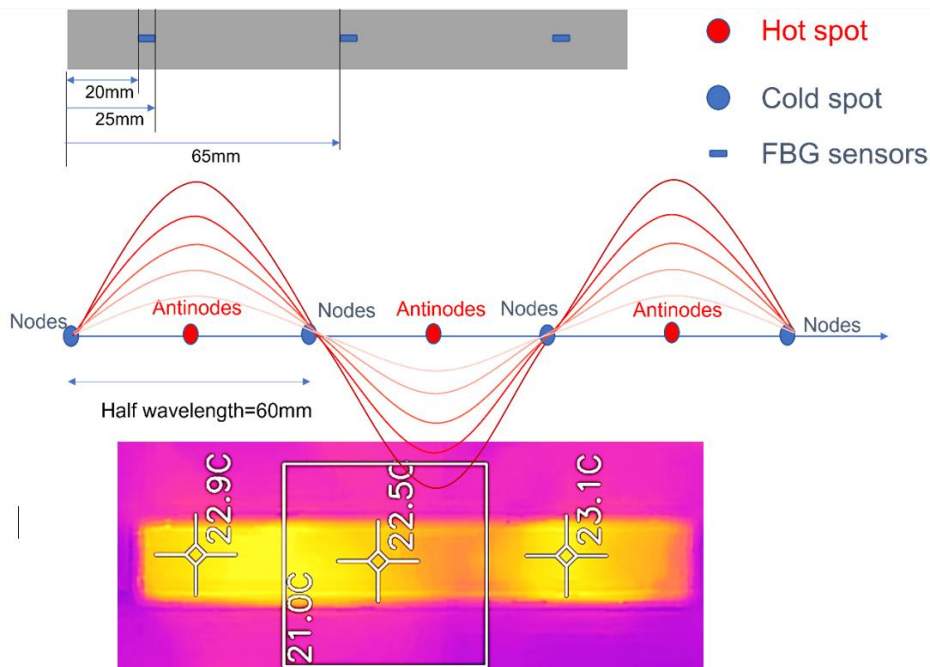


**Figure 22** Schematic illustration of (above) the location of FBGs on the sample surface, and (below) standing waves formed in a microwave oven showing hot spots (antinodes) and cold spots (nodes).

Different FBG arrays have been adhesively bonded at the same location on the surface of two specimens made of 15 wt.% with identical geometric dimensions and the location of the two specimens are placed at the exact location inside the microwave cavity. Accordingly, the distribution of microwaves in both cases is considered to be identical, also verified using thermal camera. The strain and temperature change measurements of sensor 2 under 100W and 440W before and after the 'sudden drop' is presented in Figure 23(a)-(d). It can be observed from Figure 23(a) and Figure 23(b) that the measured strains demonstrated a steady step-wise increase with the increasing temperature that fluctuated within a constant range of approximately 8°C. The fluctuations in temperature change exhibit a periodic pattern that is approximately in phase with every step of the increment in strain. Under 440W as shown in Figure 23(c) and Figure 23(d), the increase in the strain and temperature data follow a similar trend as that under 100W but at a higher rate.

In contrast with the middle sensors, the strain and temperature increments from sensor 1 under 100W and 440W are predominately synchronized as presented in Figure 24. It could be observed from Figure 24(a) and Figure 24(c) that the cycle time for each step is approximate 20s and each step is approximately 100 micro-strain. A similar trend is also observed in the first 50s of the microwave exposure under 440W from Figure 24(b). However, the cycle time for each step shown in Figure 24(d) falls sharply to 2s accompanying a higher increment of 300 micro-strain compared with the 100W data which are attributed to the increased heating rate at higher microwave power.

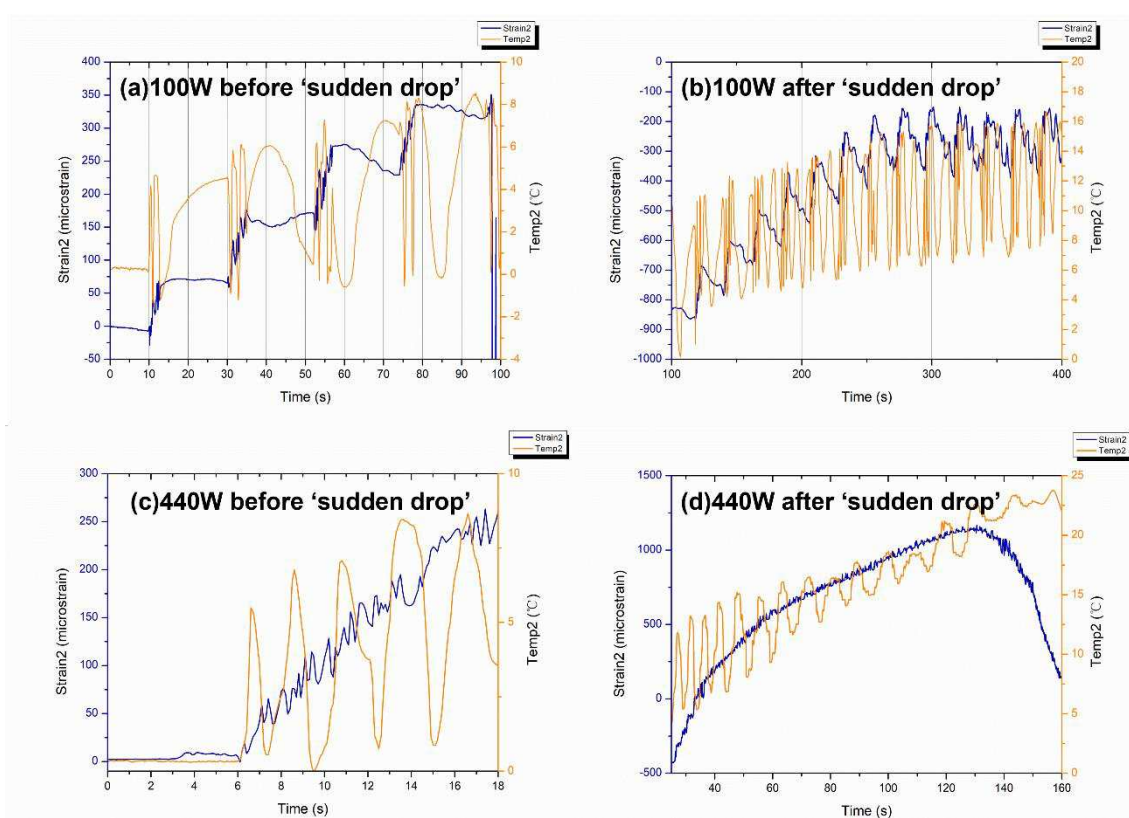


**Figure 23** Strain and temperature variations measured by sensor 2 before and after the 'sudden drop' at 100W (a,b) and 440W (c,d).

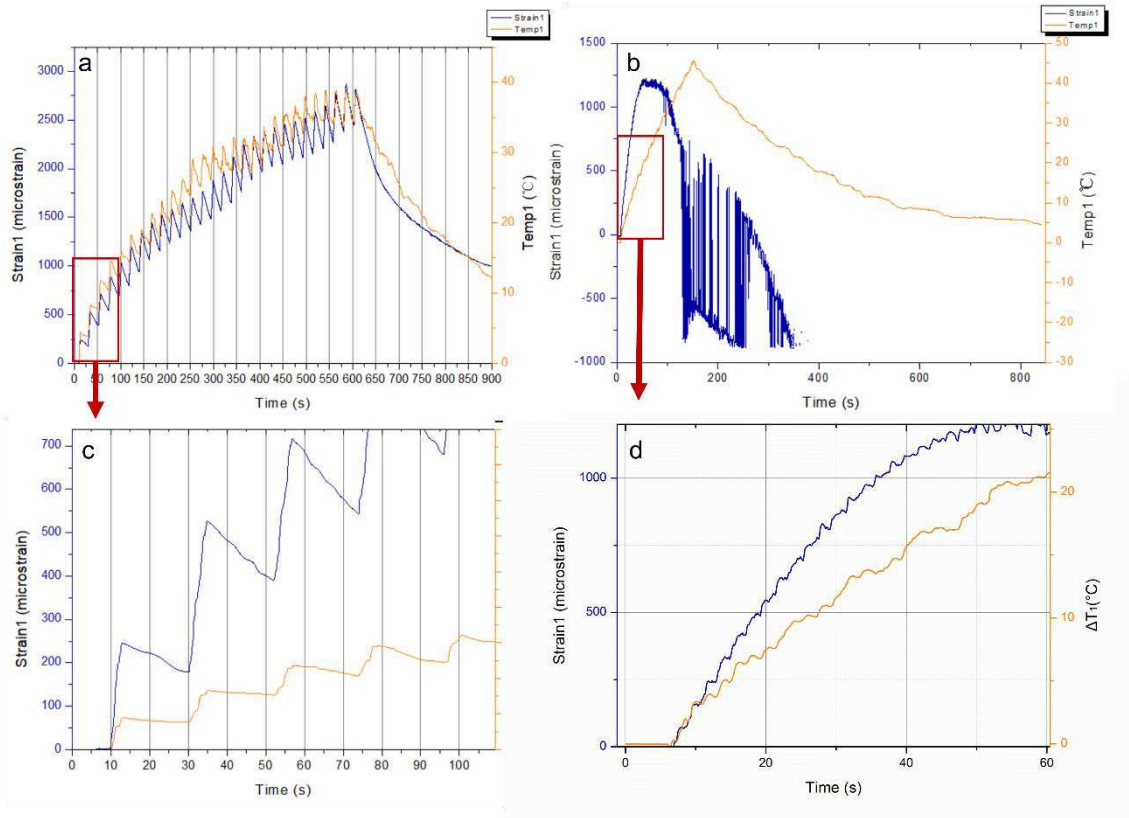


**Figure 24** Strain and temperature measurements of FBG sensor 1 of (a) and (c) 15 wt.% BaTiO<sub>3</sub>/Epoxy nanocomposite sample under 100W for 600s, (b) and (d) 15 wt.% BaTiO<sub>3</sub>/Epoxy nanocomposite sample under 440W for 148s.

**Adhesive FBG data:**

Despite the widely known utilisation of FBG strain sensors, there exists a layer of adhesive and protective coating that may affect the data from the nanocomposite [118]. The FBG sensors are adhesively bonded to the surface of specimens by PERMABOND 920 Cyanoacrylate. The dielectric and thermal properties of the adhesive and neat epoxy are presented in Table 2.

**Table 2** Dielectric properties and coefficient of thermal expansion of PTFE, Adhesive and neat epoxy.

	Real Permittivity	Loss Tangent	Coefficient of Linear Thermal Expansion (CTE) microstrain/°C
PTFE	2.1[119]	0.0004[119]	124[120]
Adhesive	2.5[121]	<0.02[121]	90[121]
Epoxy	4.25	0.01	75[122]

Five FBG sensor arrays, 20mm apart, were utilised to quantify the adhesive’s response distribution. Figure 25 presents the strain and temperature change measured via sensors bonded to a PTFE block with adhesive under 100W and 440W. It can be observed from Figure 25 that temperature increases in the adhesive with microwave exposure time at both power levels as predicted while the temperature rise has a higher rate under 400W. The maximum temperature changes are around 7°C and 4.5°C for 100W and 440W, respectively. The insignificant amount of temperature rise is the direct evidence of relative less interaction of adhesive and microwave. The strain values steadily increase with the temperature rise in both cases due to the thermal expansion of PTFE and adhesive. The calculated thermal strain of PTFE based on Figure 25 and Table 2 under 100W is approx. 868 micro-strain at 7°C temperature change. The calculated value is almost consistent with the measured value of strain sensor 1 which is approx. 960 micro-strain at similar temperature variation range. Unlike 100W, the measured strain of sensor 1 in 440W shown as the blue line (when microwaves are removed) is approximately 10 micro-strain, which is much lower than 458 microstrain, the calculated thermal strain of PTFE at the same temperature change (3.7°C).

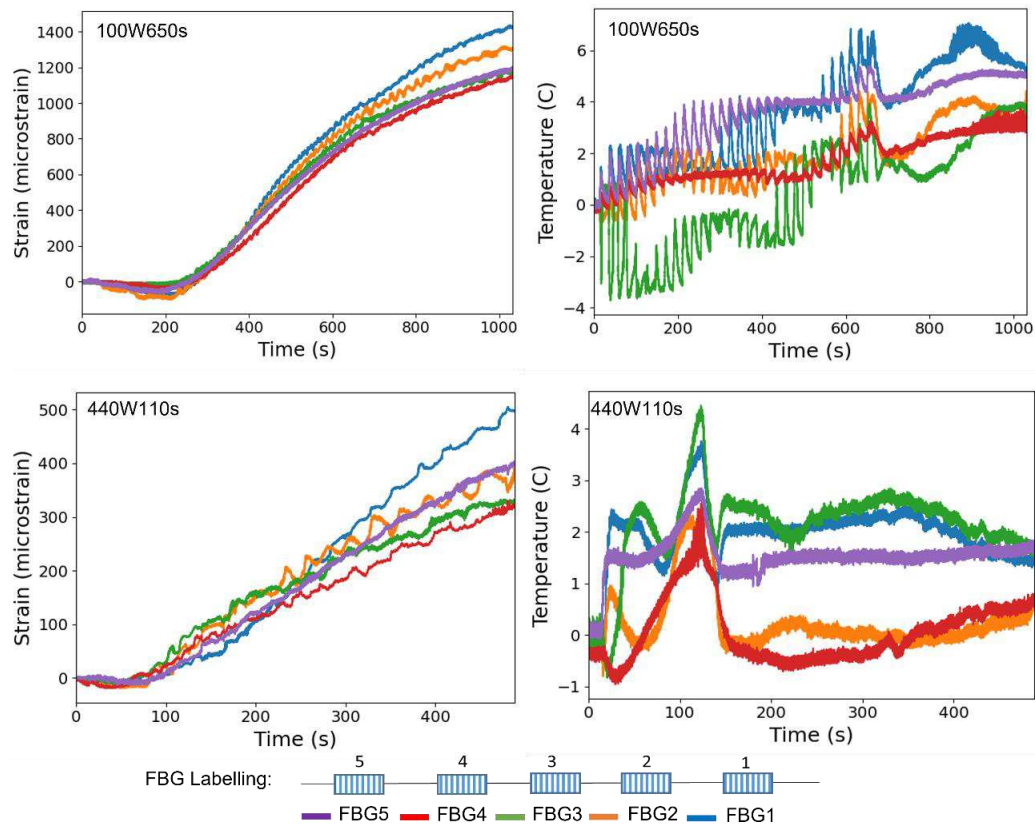


**Figure 25** Strain and Temperature evolution measurements via FBG sensors in adhesive (Permagbond 50) bonded on the surface of the PTFE holder under 100W for 650s and 440W for 110s.

At the microwave exposure, the adhesive solely interacts with the microwave, and is heated up owing to its higher dielectric loss compared with the PTFE. However, the PTFE has a higher CTE than the adhesive. Consequently, the measured strain under 100W is mainly attributed to the thermal expansion of PTFE from the conduction of heat. The strain sensors under 100W showed strain increase initiated after 200s, indicating that a substantial amount of time is required to trigger the heating conduction between the adhesive and PTFE. On the contrary, 440W has a higher rate of temperature rise within 110s exposure. Based on the analysis of the calculated and measured strain, the strain under 100W is mainly attributed to PTFE thermal expansion while the strain under 440W is dominated by the thermal expansion of adhesive. Under 440W, a similar trend in temperature rise is noted between sensors 1 and 3, as well as sensor 2 and 4, which is described by the 'hot spot' theory due to non-uniform microwave field.

#### **Neat Epoxy FBG data:**

Strain and temperature evolution of the neat epoxy with adhesively bonded arrays together under microwave are presented in Figure 26. The microwave running time has been estimated to maintain the temperature well below the  $T_g$  of the BaTiO<sub>3</sub>-epoxy nanocomposite. The temperature increases as a function of the exposure duration (equivalently, microwave energy). Sensor 5 data present a higher rate of temperature variation compared with the other sensors conforming to the 'hot spot' theory. The region in which sensor 5 is located within the zone with a higher rate of temperature rise that is denoted as a 'hot spot' zone presented in Figure 27, hence the next hot spot shown in Figure 27 (red square symbol) is half (60 mm) of the microwave wavelength (120 mm) is located between sensors 3 and 2. As schematically demonstrated, the rest of the FBG sensors are located out of the hot spot region, and therefore they develop similar rates of temperature under microwave.

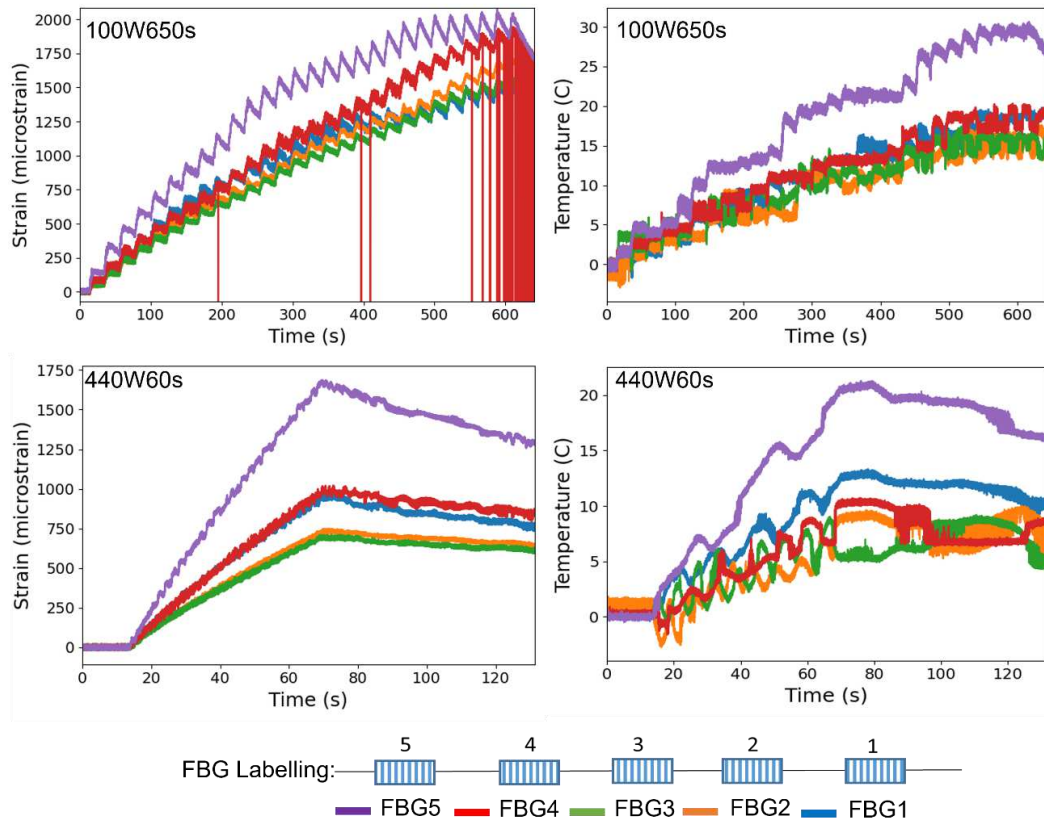


**Figure 26** Strain and temperature evolution of the neat epoxy sample under 100W and 440W.

Strain and temperature response of the neat epoxy with bonded sensor arrays is investigated under microwave (Figure 26). The temperature increases as a function of microwave exposure time and starts to drop as soon as the microwave stops as predicted. No sudden drop such as that observed in the nanocomposite is observed for the neat epoxy which indicates the phenomenon linked with the embedded BaTiO<sub>3</sub>. Sensor 5 presents a higher rate of temperature change compared with the other sensors, corresponding to the ‘hot spot’ theory discussed formerly, and illustrated in Figure 27. As schematically shown in Figure 27, the other FBG sensors are located out of the hot spot region, and therefore develop similar rates of temperature variation under microwave.

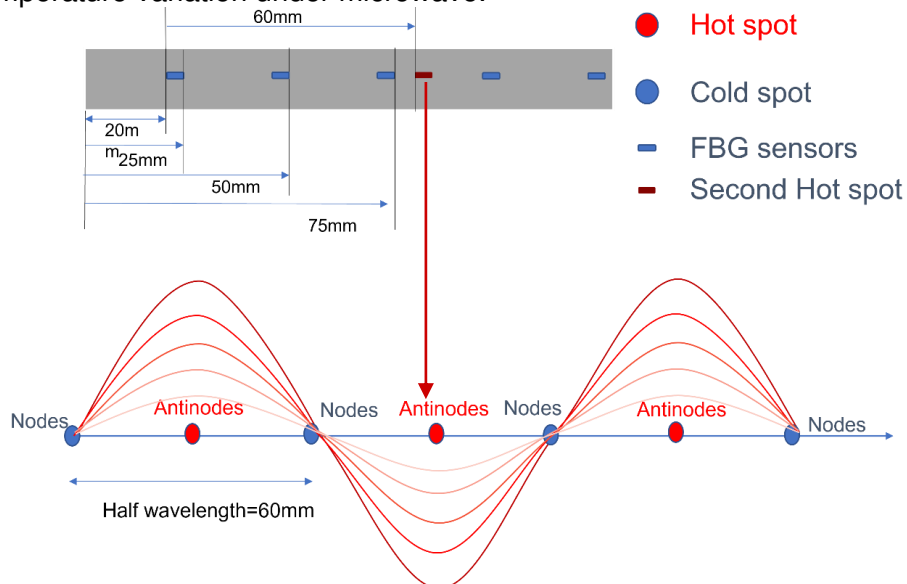


**Figure 27** Schematic illustration of the location of FBG sensors on the neat epoxy surface, 20 mm apart, and standing waves formed in a microwave oven showing hot spots (antinodes) and cold spots (nodes).

The temperature change in both cases reached the highest value of 30°C compared with that measured for the adhesive only. The measured strain follows an increasing trend with the temperature change, which is a resultant of the thermal expansion from the adhesive and neat epoxy. Maximum strain and temperature values measured by left-side sensor for adhesive on PTFE (sensor 5), adhesive on epoxy (sensor 5), and adhesive on nanocomposite (sensor 1) are tabulated in Table 3, summarised from the data shown in Figure 20 and Figure 21, under 100W and 440W exposure.

**Table 3** Strain and temperature change measurements under 100W and 440W of three categories: FBG sensors bonded by adhesive to PTFE, FBG sensors bonded by adhesive to the neat epoxy, and FBG sensors bonded by adhesive to the epoxy nanocomposite with BaTiO<sub>3</sub>

100W			440W		
Strain/*10 <sup>-6</sup>	ΔT/°C	Time/s	Strain/*10 <sup>-6</sup>	ΔT/°C	Time/s
Adhesive+PTFE					
790	5.0	650	70	2.8	110
Adhesive+epoxy					
375	5.0	40	320	5.0	14
2080	30.0	600	1700	21.0	60
BaTiO <sub>3</sub> -epoxy nanocomposite+ Adhesive					
243	5.0	31	330	5.0	15
2230	30.0	445	1225	21.0	58

The measured strain of the first two categories (adhesive on PTFE and adhesive on the neat epoxy) are temperature compensated which means the effect of thermal expansion from the optical fibre itself is eliminated. Approximately 8 micro-strain is achieved by a 1°C change in temperature according to the manufacture. The true strain of the epoxy nanocomposites samples is then lower than the measured strain from sensor 1:

For the case of 100W exposure, the measured strain of adhesive on PTFE is mainly attributed to the thermal expansion of the PTFE, as formerly discussed. When the FBG arrays are adhesively bonded to a neat epoxy sample, the measured strain drops by approx. 52% compared to that (790 micro-strain) from the sensor adhesively bonded on PTFE at the same temperature variation of 5°C. It is due to the lower CTEs of epoxy and adhesive compared to that of the PTFE. Furthermore, at this temperature change (5°C), the measured strain without temperature compensation of epoxy nanocomposites loaded with BaTiO<sub>3</sub> drops 35% compared with the neat epoxy. However, as temperature change rises to 30°C, the measured strain in both cases tends to be similar. Under 440 W, the value of strain is mostly dominated by adhesive as described earlier. When the temperature change firstly reaches 5°C at the beginning of the microwave exposure, the neat epoxy and nanocomposites have similar strain (320 and 330 micro-strain, respectively).

### 7.3 Raman Characterisation

Raman spectroscopy was utilised to examine any residual/remnant strain induced by the particles to the surrounding epoxy matrix, or any crystal structure transformation of BaTiO<sub>3</sub> particles that might be introduced by the microwave exposure. The middle region of the samples where the 'sudden drop' in strain occurred was of particular interest, hence it was the region where the laser was focused to obtain the Raman spectra. Another run at microwave power of 1000W for 50s was performed for such effect.

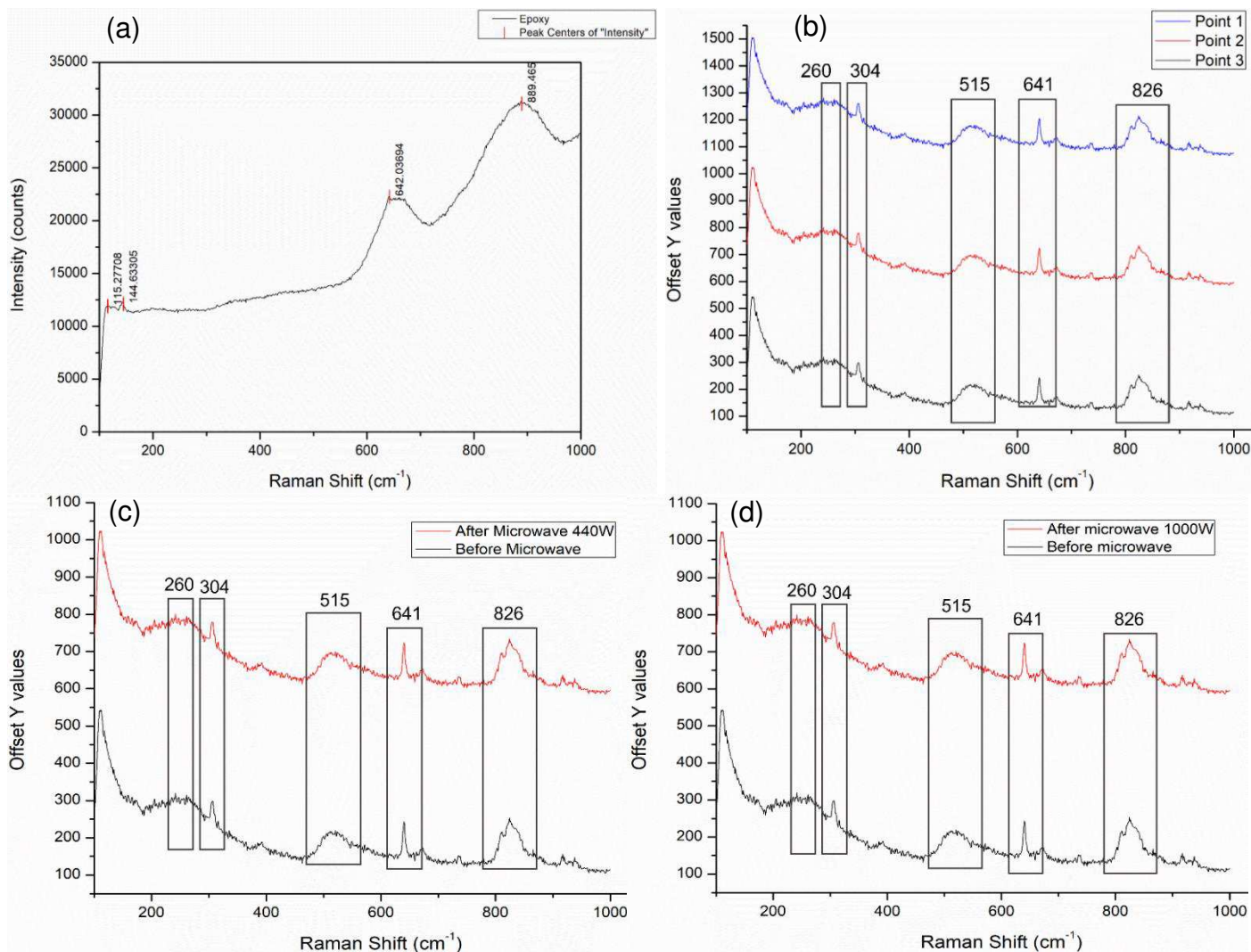


**Figure 28** Raman spectra of (a) neat epoxy, (b) three random points of 15 wt.% epoxy nanocomposites with Si-BaTiO<sub>3</sub> before microwave exposure, (c) 15 wt.% epoxy nanocomposites with Si-BaTiO<sub>3</sub> before and after microwave exposure of 440W for 150s (d) 15 wt.% epoxy nanocomposites with Si-BaTiO<sub>3</sub> before and after microwave exposure of 1000W for 60s.

Raman characterisations have initially been performed on the neat epoxy and BaTiO<sub>3</sub>-epoxy nanocomposite samples with 15 wt.% prior to microwave to establish baseline curves for identification of possible change in the position of Raman peaks for the samples post microwave exposure. Raman spectra of the epoxy are shown in Figure 28(a). Broader peaks at 600-800 cm<sup>-1</sup> and 800-1000 cm<sup>-1</sup> are presented in Figure 28(a) for the neat epoxy indicating an amorphous structure. The Raman spectra on three random points within the region of interest of the 15 wt.% Si-BaTiO<sub>3</sub> epoxy nanocomposite (Figure 28(b)) present a good consistency with 260 cm<sup>-1</sup> and 515 cm<sup>-1</sup> as characteristic peaks of BaTiO<sub>3</sub>, and 304 cm<sup>-1</sup> indicating the tetragonal phase of BaTiO<sub>3</sub> representing the out-of-phase and axial motion of the two oxygen atoms facing oppositely [123, 124]. The stretching mode of Si-O from silane functionalisation on the particle surface is presented as peaks at 641 cm<sup>-1</sup> and 826 cm<sup>-1</sup> [125]. Raman spectra of the samples before and after microwave exposure at 440 W at room temperature are shown in Figure 28(c). Another run at 1000W for 50s was performed with Raman performed at the same location as that at 440W, presented in Figure 28(d). No conspicuous differences are observed, and it could be noticed that the 304 cm<sup>-1</sup> still emerges without recognizable changing in peak height, which implies no changes in the crystal structure of BaTiO<sub>3</sub> after the microwave exposure, and no or slight remnant strain field.

## 8 DISCUSSION

### 8.1 Compressive strain field induced in BaTiO<sub>3</sub>-epoxy nanocomposite under microwave exposure

The strain measured by the FBG sensors is a resultant from coupling fields between the stress field, the electric component of microwave and thermal field due to microwave dielectric heating as illustrated in Figure 29. A small change in one of the fields introduces a corresponding change in others via dielectric heating, thermal expansion, and electromechanical effects. The aim of the research has been to obtain the compressive electro-induced strain in the surrounding matrix of the BaTiO<sub>3</sub> particles under microwave. The dielectric heating process begins instantaneously, and the temperature starts to increase as labelled process '2'. Consequently, the thermal expansion of the sample introduces a thermal strain labelled as process '3' and contribute to the total strain measurements from the FBG results. In the meantime, another contributor is the microwave triggered compressive stress field within the elastic limit labelled as process '1'. The objective of this test was to find a prominent difference between the FBG measured strain results and the calculated strain induced by linear thermal expansion of samples to confirm the presence of a compressive stress field introduced by the BaTiO<sub>3</sub> particles, elaborated as follows:

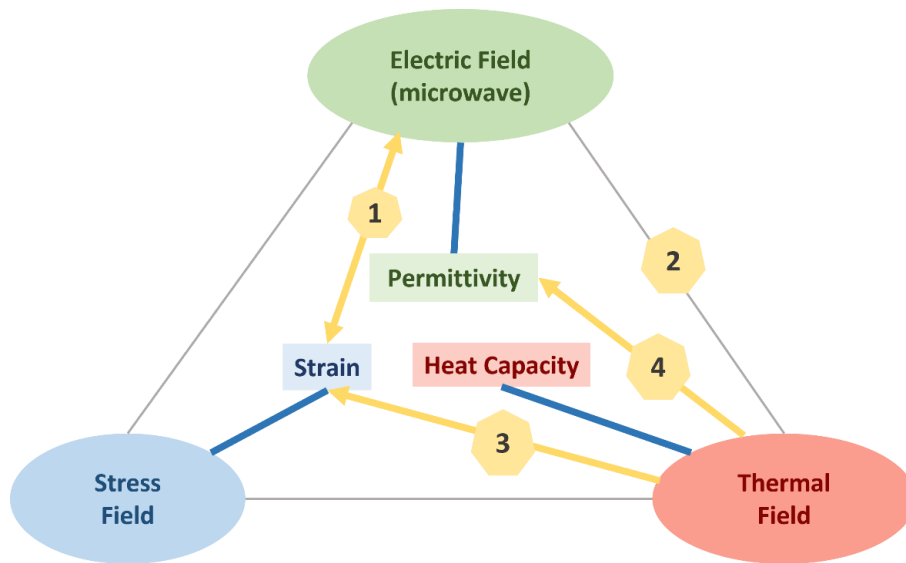


**Figure 29** Heckmann diagram, schematically depicting the coupled electric, mechanical, and thermal field of ferroelectric crystals, recreated from [126].

It was observed from the FBG test results that the overall strain measurements of the 15 wt.% BaTiO<sub>3</sub>-epoxy nanocomposites are relatively smaller compared to those of the neat epoxy under 100W and 440W. The strain measurements of the nanocomposites from the beginning of the microwave exposure ( $\Delta T=5^{\circ}\text{C}$ ) to a later stage (100W:  $\Delta T=30^{\circ}\text{C}$  440W:  $\Delta T=21^{\circ}\text{C}$ ) from sensor 1 data are presented as blue triangle marks in Figure 30 and Figure 31. The strain measurements of the nanocomposites shown in Figure 20, Figure 21, and Table 3 have not been corrected to account for the temperature effect of fibre refraction index, while the results presented as blue triangle symbols in Figure 30 and Figure 31 are corrected values accounting for such effect. Strain measurements of the neat epoxy are also presented as red circle symbols to evaluate the mechanical strain induced by dielectric heating under the exposure.

It could be observed from the figures that the measured strain of the nanocomposite (blue triangles) are generally smaller than that of the neat epoxy (red circles). Notably, the difference increases with increasing temperatures under 440W.

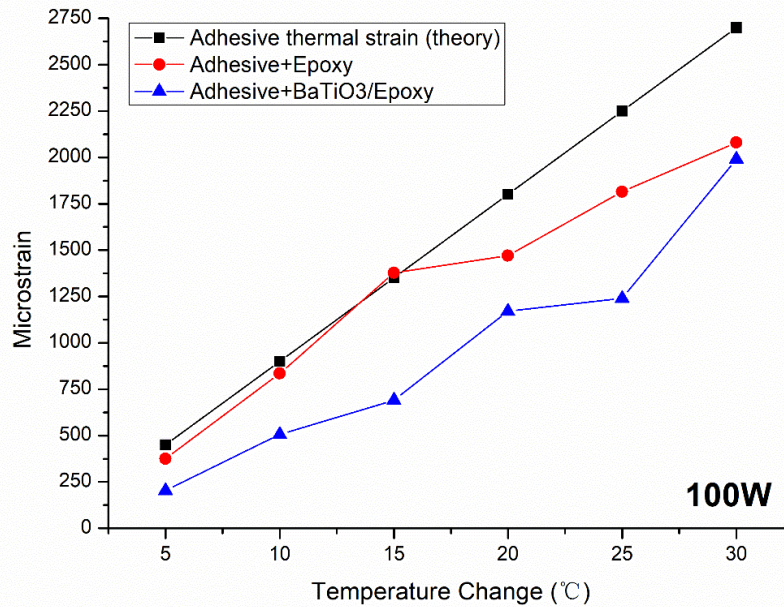


**Figure 30** Evolution of micro-strain with temperature rise – theoretically calculated thermal expansion of adhesive (black), actual strain data from sensor 5 of adhesive bonded onto neat epoxy (red), and actual strain data from sensor 1 of adhesive bonded to 15 wt.% BaTiO<sub>3</sub>-epoxy nanocomposite (blue) under 100W at 5°C, 10°C, 15°C, 20°C, 25°C, and 30°C.

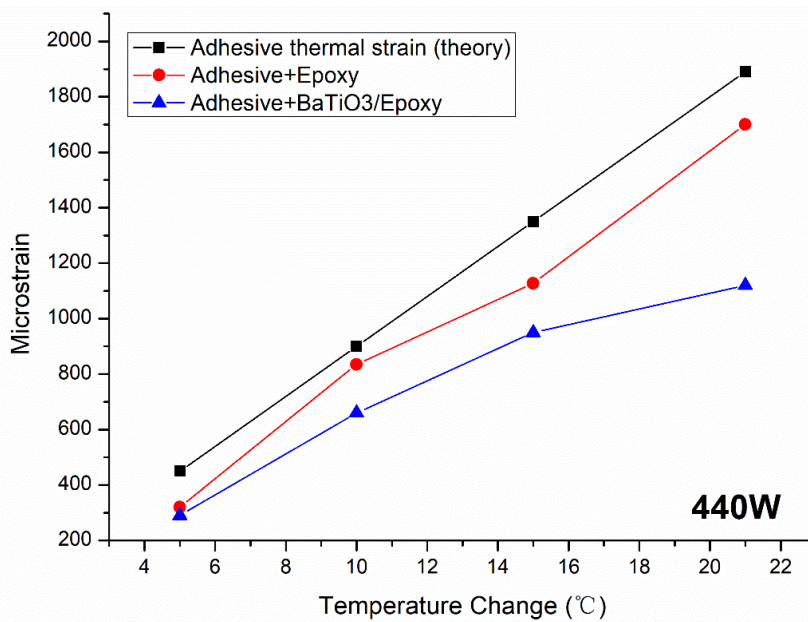


**Figure 31** Evolution of micro-strain with temperature rise – theoretically calculated thermal expansion of adhesive (black), actual strain data from sensor 5 of adhesive bonded onto neat epoxy (red), and actual strain data from sensor 1 of adhesive bonded to 15 wt.% BaTiO<sub>3</sub>-epoxy nanocomposite (blue) under 440W at 5°C, 10°C, 15°C, and 21°C.

It is well known that the mechanical properties such as elastic modulus, Poisson's ratio, and shear modulus [127-129] and the CTE [130-133] are strongly dependent upon the microcracks in the matrix. Camahort *et al.* [134] correlated a reduction of the CTEs of thermal cycled composite laminates in the specimens with microcracks identified under the microscope. A theoretical study of the CTEs in cracked laminates demonstrated that CTEs change as a function of the internal stress field [132]. This discrepancy in CTEs under different internal stress fields is due to the fact that the internal stresses induced by thermal cycling could be either tensile or compressive. When the stress field is tensile, the microcracks further opened up and cause a reduction in the value of CTE. Therefore, this correlation between the microcracks and CTEs

might provide an explanation of the reduced strain measurements presented previously. Under microwave, domain wall movements are triggered in the BaTiO<sub>3</sub> nanoparticles, hence stress fields around the microcracks might be changed and lead to a different CTE of the nanocomposite as illustrated in Figure 32.

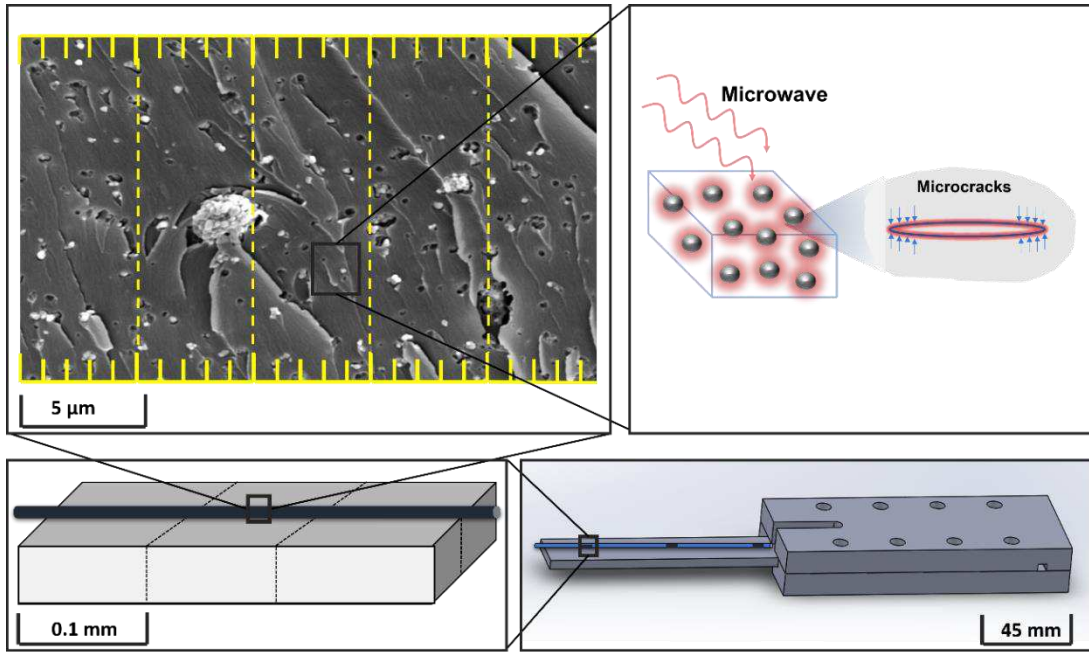


**Figure 32** Schematic of the 15 wt.% BaTiO<sub>3</sub>-epoxy nanocomposite under exposure at different scales.

It is found by many studies that the CTE of composite material is highly dependent upon its constituents [135, 136]. However, it still remains unclear that to which degree the mismatch in CTEs is attributed to the reduced strain measurements of the nanocomposite compared with the neat epoxy. The average crystallite size of the purchased BaTiO<sub>3</sub> nanoparticles are determined by XRD results using Scherrer's equation [137]:

$$\text{Crystallite size} = \frac{k\lambda}{B(2\theta)\cos(\theta)} \quad 79$$

where  $k$  is the dimensionless shape factor of the crystallite,  $\lambda$  is the X-ray wavelength,  $2\theta$  is the peak position,  $B(2\theta)$  is the half-width of the maximum intensity of the peak and  $\theta$  is the Bragg diffraction angle. A round-up value of 1.0 is selected in this study. The mean crystallite size is 35.9 nm, and it indicates that the corresponding grain size is 35.9 nm in the 200 nm BaTiO<sub>3</sub> nanoparticles as shown in Figure 33. Note that the strain measured by the sensors is averaged over a 5mm×0.5mm region (i.e. sensor size). Such sensing area covers approximately 890,000 200nm-particles, or alternatively 70 particles over a 20×20 μm<sup>2</sup> area.

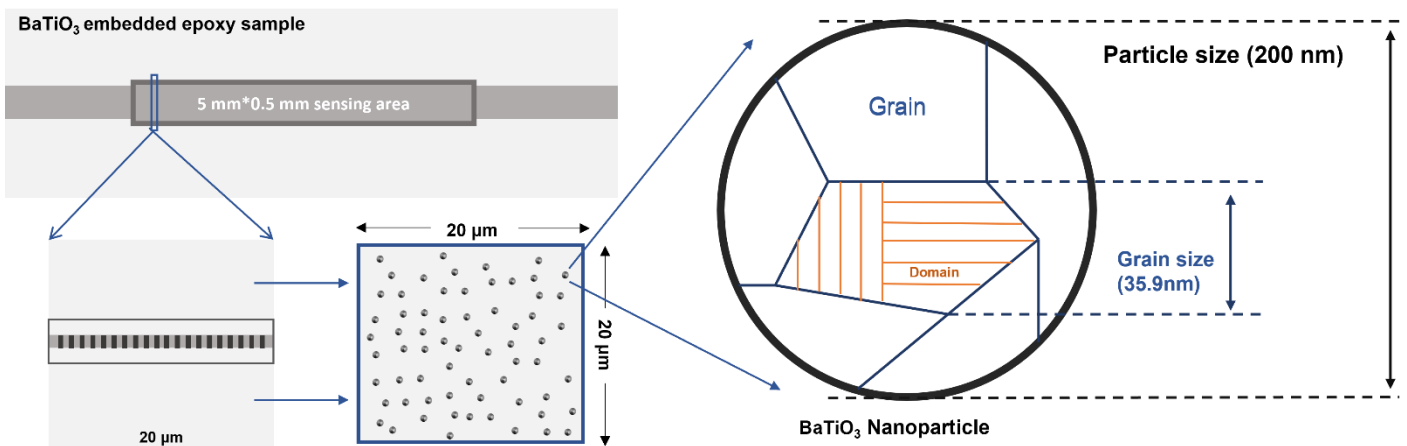


**Figure 33** Nanocrystalline structure of BaTiO<sub>3</sub> nanoparticles well-dispersed within the area over which the extrinsic strains are measured by the FBG sensors.

The difference in the grain size and particle size is an implication of polycrystal structure in the particles. As illustrated, each grain consists of many domains that have different orientations in six possible directions. Therefore, the mechanical response of BaTiO<sub>3</sub> nanoparticles is a collective result from each particle from all possible directions and it is not straightforward to have an explicit prediction of the stress field induced by the DW movements, experimentally, and the extent at which it is possible to alter the stress field tensor direction (for accounting either tensile or compressive) remains unknown.

The black square marks in Figure 30 and Figure 31 represent the theoretically calculated values of linear thermal expansion of the adhesive used for bonding the FBG arrays. It can be observed that the strains in the neat epoxy are slightly lower than those measured by the thermal expansion of the adhesive at an identical temperature. A schematic diagram of the cross-section of an FBG array bonded to the sample is presented in Figure 34. As discussed for Figure 25 and Figure 26, the adhesive exhibits lower interaction with microwave, hence a poorer dielectric heating effect. Thus, when the exposure initiated, the neat epoxy is firstly heated up due to the microwave selective heating based upon its different dielectric loss. The energy is then transferred to the adhesive via heating conduction from the epoxy, which initiates a thermal expansion in the adhesive. However, the epoxy possesses a relatively lower CTE in comparison with that of the adhesive. Consequently, the thermal expanding rates are different due to the mismatch in CTEs. As such, the measured strain in the FBGs is a result of thermal expansion of the adhesive constrained (via bonding) by the epoxy, causing the FBG arrays to bend with increasing temperature and bend back when the temperature drops. This behaviour might also be an explanation of the ‘zig-zag’ step-wise increment observed in Figure 24. When the temperature ramping rate is slower under 100W, the heat transfer between the epoxy and the adhesive is steadier compared with that under 440W. Subsequently, the strain measurements exhibit a clearer step-wise increment under 100W.

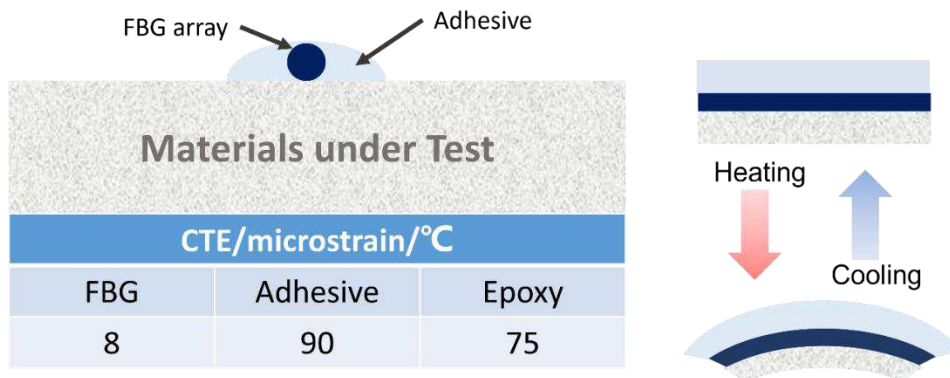


**Figure 34** Schematic diagram of adhesively bonded FBG arrays to the sample’s surface and non-uniform thermal expansion due to mismatch in CTEs.

It is also noteworthy that the unanticipated finding of a ‘sudden drop’ during real-time strain measurement of the middle FBG sensor (presented in Figure 20 and Figure 21) occurs at the beginning of the microwave exposure at 1045 micro-strain under 100W and 1261 micro-strain under 440W, which is a clear implication of existing compressive strain around the middle FBG sensor. The corresponding temperature is under 31°C hence ruled out the possible effects from post-curing shrinkage. Also, the FBG arrays for strain measurements on each sample are adhesively bonded to the surface therefore disposable. The true reason for the occurrence of this phenomenon remains unclear, however since the temperature effects are excluded and the phenomenon is only seen in the nanocomposite (and not in the neat epoxy), such high extrinsic strain variation is strongly attributed to the collective domain wall movements due to the reorientation of dipoles at high frequency in each domain.

#### 8.4 Effect of non-uniformity of the Microwave Cavity

As the microwave travels through the material, the microwave power decays due to the absorption by the material as it penetrates. As a result, the distribution of the microwave field within the material is non-uniform. For the 15 wt.% BaTiO<sub>3</sub>-epoxy nanocomposites, the penetration depth calculated by Equation 70 is approximately 0.86m, based on the measured dielectric properties at 2.5 GHz. This value indicates that approximately 63% of the energy from the incident microwave is dissipated at this distance under the

sample surface. Therefore, for a nanocomposite with 3-mm thickness, it would be a reasonable assumption to make that the microwave fully penetrates the sample. Apart from the non-uniformity caused by the penetration depth of the microwave, there is also another factor that affects the non-uniform electric field distribution in the material, which is the standing waves formed in the microwave oven, extensively studied [138-140]. When the microwave field transmits and reflects within the cavity of the microwave oven, the standing waves form, and the 'hot spot' phenomenon manifests. The distance between two 'hot spots' is half of the wavelength of the incident microwave, which is approximately 60mm. Therefore, the temperature change measured by FBG sensors exhibit different heating rates along with the 130 mm sample.

### 8.5. Effect of absorbed microwave power

The power absorbed by the material is evaluated by the method of the energy balance of the microwave heating effect. At power 100W, the average power per unit area in the 354×338 mm<sup>2</sup> microwave oven is calculated as follows:

$$I = \frac{P}{A} = \frac{100}{0.354 * 0.338} \approx 835.8 \text{ W/m}^2 \tag{80}$$

From Equation 71 and Equation 72, the peak electric field strength  $E_m$  and root-mean-square  $E_{rms}$  of the incident microwave field is:

$$E_m = \left( \frac{2I}{c\epsilon_0} \right)^{1/2} = 793.5 \text{ V/m} \tag{81}$$

$$E_{rms} = \sqrt{E_m^2/2} = 561.1 \text{ V/m} \tag{82}$$

Similarly, for the 440W microwave power level, the peak electric field strength  $E_m$  is  $1.67 \times 10^3$  V/m, and the  $E_{rms}$  is  $1.18 \times 10^3$  V/m. The estimated electric field is the power absorbed by the air. However, it is assumed that when the microwave field generation is initiated by the magnetron, the electric field strength within the microwave oven is assumed to be equivalent to the value of the  $E_{rms}$  as the dimension of the sample (4 cm<sup>3</sup>) is relatively smaller than the cavity size (27520 cm<sup>3</sup>). The energy absorbed as a function of time calculated based on the  $E_{rms}$  calculated above is estimated as follows:

$$P_{estimated} = 2\pi f \epsilon_0 \epsilon'' E_{rms}^2 V t \tag{83}$$

The strain and temperature measurements as a function of energy absorbed in Joules are presented below, under 100W and 440W.

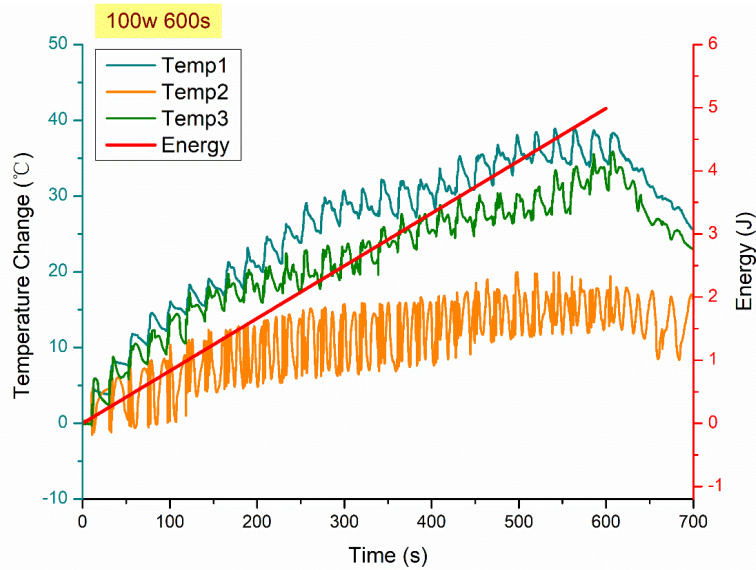


**Figure 35** Temperature change measurements (micro-strain) by FBG sensors (left), and energy absorbed (right) versus time (s) under 100W.

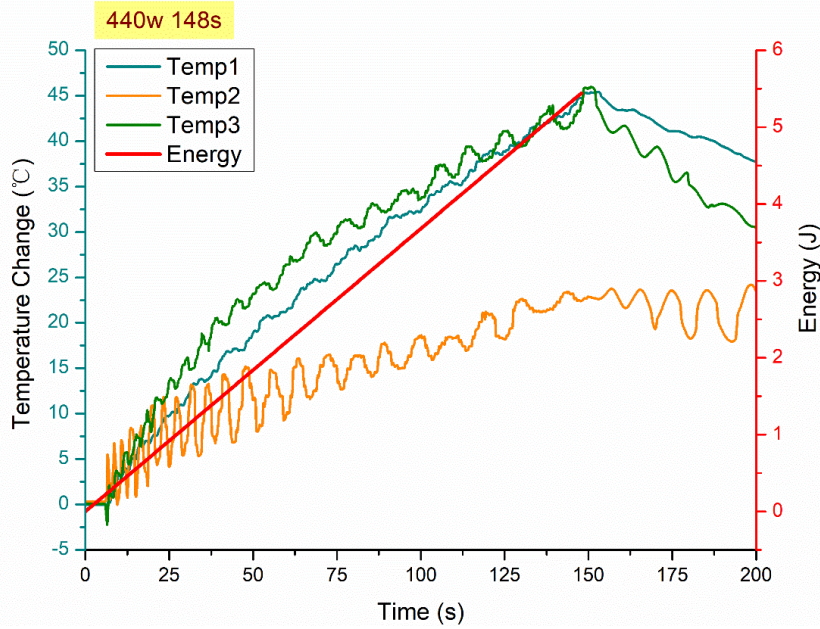


**Figure 36** Temperature change measurements (micro-strain) by FBG sensors (left), and energy absorbed (right) versus time (s) under 440W.

It could be observed from Figure 35 and Figure 36 that, the energy absorption rate is close to the rate of temperature rise in the FBG sensors. At the beginning of the microwave exposure, the temperature rise exhibits a similar rate compared with the energy absorption rate. As the exposure time increases, the temperature rise becomes significantly slower. The 'hot spot' theory due to the non-uniformity of microwave fields is proposed to be the possible explanation of this phenomenon as described formerly.

The internal electric field inside the sample could only be estimated based on the assumption that 100% energy transfers into heat. Therefore, the external electric field of the incident microwave at the surface of the BaTiO<sub>3</sub>/Epoxy sample,  $E_{rms,external}$  is obtained from Equation 75, and employed to be the  $E_{rms}$  to solving the Equation 27 to estimate the eigenstrain of the BaTiO<sub>3</sub>.

$$E_{rms} = \sqrt{\frac{\rho C a \Delta T}{3 \Delta t c \epsilon_0 \xi \Gamma}} \approx 12.1 \times \sqrt{\frac{\Delta T}{\Delta t}} \quad 84$$

where calculated  $\rho$  by given weight and volume is 1.3 g/cm<sup>3</sup>,  $C$  calculated from the DSC spectra is 1.238 J.g<sup>-1</sup>.°C<sup>-1</sup>,  $a$  is sample thickness 3 mm,  $c$  is the speed of microwave ( $3 \times 10^{10}$  cm/s),  $\epsilon_0$  is the permittivity of the free space ( $8.85 \times 10^{-14}$  F/cm), and  $\xi$  and  $\Gamma$  is calculated by Equation 76, Equation 77, as follows:

$$\xi = 1 - e^{-\frac{2a}{d_p}} \approx 0.007 \quad 85$$

$$\Gamma = \frac{4(n_1/n_2)}{[(n_1/n_2) + 1]^2} \approx 0.874 \quad 86$$

Where  $d_p$  is calculated to be 850 mm,  $n_1$  is 1 for air and  $n_2 = \sqrt{\epsilon'} = \sqrt{4.42}$ .

At the beginning of the exposure when the microwave incident the sample at  $t = 10$ s under 100W, the rate of temperature rise  $\frac{\Delta T}{\Delta t}$  is obtained using the linear fit of the temperature change measurements from FBG sensor 1, which is 0.05.

$$E_{rms} = 2.71 \text{ V/cm} \quad 87$$

The eigenstrain of BaTiO<sub>3</sub> nanoparticle movements based on the simplified model of Equation 26 and Equation 27 at 100W,  $\epsilon_{BaTiO_3}$  is:

$$\varepsilon_{100} = \frac{\Delta l_m}{L} = \frac{f_m}{d^2 Y} = \frac{\sqrt{2} P_0 E_m}{d^2 Y} = 65 \times 10^{-6} \quad 88$$

where  $P_0$  is  $0.26 \text{ C/m}^2$ ,  $Y$  is the young's modulus of  $\text{BaTiO}_3$ , which is assumed  $13.6 \times 10^8 \text{ N/cm}^2$  [61].

The domain width  $d$  is highly dependent on the grain/crystallite size, therefore, it is estimated to be  $4 \times 10^{-5} \text{ cm}$  with the crystallite size assumed to be equal to the nanoparticle size  $200 \text{ nm}$  based on the measurements in previous studies [141], and the strain  $\varepsilon_{440}$  at  $t = 7 \text{ s}$  under  $440 \text{ W}$  with the rate of temperature rise of  $0.3$ , is  $144 \times 10^{-6}$ . This value could only represent the approximate amplitude of the induced DW displacement under such electric field that impinges the sample surface.

### 8.6. Post-microwave Residual Effect in the $\text{BaTiO}_3$ /Epoxy Nanocomposites.

As discussed in Section 3, the electric field-induced strain is predominately attributed to the irreversible domain wall movement in multi-domain ferroelectric crystals. Therefore, when the microwave field is removed, a residual stress field is hypothesised, and Raman spectroscopy was employed in this study to probe any possible residual strain effects that originate from microwave field activated  $\text{BaTiO}_3$  nanoparticles. The Raman peaks shift indicated the changes in the atomic spacing of the material, namely the strain information [142]. In the meantime, it was also discovered that the altered stress state surrounding the  $\text{BaTiO}_3$  could introduce a crystal structure change due to the piezoelectricity effect exhibit in ferroelectric materials. Raman data did not indicate a significant difference between the Raman spectra of  $15 \text{ wt.}\%$  nanocomposite samples with and without microwave treatment.

## CONCLUSIONS

The quantitative research on microwave field-nanocomposite interaction was conducted to study the ferroelectric materials' response in high-performance (rigid) epoxy composite that offers reversible microwave activated electro-strains introduced by a second dielectric phase ( $\text{BaTiO}_3$ ). The data presented a pioneering investigation as no investigations have been reported, thus far, on the micromechanical (extrinsic) strain response of rigidly constrained ferroelectric materials in polymer under external electromagnetic fields. Their effect on the surrounding epoxy as the phenomenological strain state was investigated. The research has characterised the thermal and dielectric properties of ferroelectric nanoparticles ( $\text{BaTiO}_3$ ) modified polymer (epoxy) at weight loading up to  $15 \text{ wt.}\%$ , and subsequently investigated the extrinsic strain state induced by the  $\text{BaTiO}_3$  nanoparticles' dipole displacements onto their surrounding epoxy. Silane surface functionalisation of the nanoparticles was utilised to uniformly disperse and improve interfacial particle-matrix bonding quality. FBG sensors-based technique was employed, in-situ with the microwave exposure, for real-time monitoring of the strain and temperature response of the nanocomposite subjected to a  $2.45 \text{ GHz}$  microwave field at controlled exposure power and energy, followed by newly developed theoretical constitutive equations and the remnant extrinsic strain investigations using Raman spectroscopy. The key remarks on the investigations conducted in this article are as follows:

1. A time-dependent strain field is introduced, proportional to the exposure time/energy, in the multi-domain  $\text{BaTiO}_3$  nanoparticles under the stimulation of a microwave field, linearly under  $100 \text{ W}$  and non-linearly under  $440 \text{ W}$ . The strain is theoretically described via development of a novel multi-physics constitutive model of the nanoparticle possessing a multi-domain crystallite based on an estimated electric field strength exhibiting at the geometric boundary of the particle.
2. The principle of virtual work was utilised, phenomenologically for the theoretical development, to estimate the strain within the epoxy matrix embedded with  $\text{BaTiO}_3$  subjected to the microwave exposure, able to underpin the in-situ induced micro-straining performance of the  $\text{BaTiO}_3$ -epoxy nanocomposite.
3. A sudden drop in micro-strain data by the value of  $1000$  compressive micro-strains was observed in the  $\text{BaTiO}_3$ -epoxy composites at the beginning phase of the exposure under the different exposure powers examined. Such phenomenon has not been reported thus far in the existing literature, however investigated herein using different characterisation and theoretical development at micromechanical level. The drop indicated an instantaneously induced compressive strain achieved within a small fraction of a second, which is recovered afterwards with the increasing exposure energy, followed by a gradual increase during the exposure. No arcing in the microwave was observed, and no damage in

any part of the FBG, adhesive, composite and PTFE; The temperature variation due to the exposure was kept well below the  $T_g$ , and the DSC investigations presented a fully cured nanocomposite. The theoretical-experimental study of the response led to the fact that such effect is caused by the DW movement response of the BaTiO<sub>3</sub>-epoxy composite under microwave exposure, which introduced a mechanical compressive field to its surrounding polymer, observed by the in-situ FBG technique.

4. The nanocomposite exhibited linear and highly non-linear strain variations under the 100W and 440W exposure, respectively. Residual compressive strains were developed post 440W exposure, offering an analogous response to the mechanical field pre-straining which takes the strain hardening materials (e.g. polycrystalline) beyond its elastic regime. Such strain hardening response in the case of 440W is attributed to the semi-crystalline phase that BaTiO<sub>3</sub> had introduced to the nanocomposite.
5. To achieve the full benefit from the electro-strain behaviour of the BaTiO<sub>3</sub> fillers, uniform dispersion of the nanoparticles in the epoxy matrix was considered to be the primary determinant factor. Large agglomerates were observed in non-functionalised BaTiO<sub>3</sub>-epoxy nanocomposites due to the attraction between the nano-scale particles, and their intrinsic incompatibility with hydro-carbon epoxy matrix. Uniform dispersion of the surface functionalised BaTiO<sub>3</sub> nanoparticles ensures a uniform application of the domain wall movements triggered stress field to their surrounding epoxy matrix. Furthermore, it also avoids the possible negative attributes from large agglomerations to the mechanical performances, as the aggregation of nanoparticles might act as a weak spot compared with the uniform dispersed nanoparticles. The efficiency of silane functionalisation on the uniform dispersion of BaTiO<sub>3</sub> nanoparticles was demonstrated.
6. A reduced thermal expansion was observed in the BaTiO<sub>3</sub>-epoxy nanocomposite, due to a resultant internal stress field induced from the mismatched nanoparticle-matrix CTEs and the DW movement activated by the electric component from the microwave field.

## ACKNOWLEDGEMENTS

The authors would like to acknowledge the grants received for this research from the UK Engineering & Physical Sciences Research Council (EPSRC), Ref. EP/R016828/1 (Self-tuning Fibre-Reinforced Polymer Adaptive Nanocomposite, STRAINcomp) and EP/R513027/1 (Study of Microstructure of Dielectric Polymer Nanocomposites subjected to Electromagnetic Field for Development of Self-toughening Lightweight Composites). We would also like to express our deepest gratitude to Prof. Vijay Kumar Thakur, Drs. Christine Kimpton, Adrianus Indrat Aria and Junfeng Chen, and Mr. Jim Hurlly, Ben Hopper, Steve Pope and Andrea Giampiccolo, for their continuing support during the research.

## REFERENCES

1. Ozdemir, N.G., et al., *Toughening of carbon fibre reinforced polymer composites with rubber nanoparticles for advanced industrial applications*. Express Polymer Letters, 2016. **10**(5): p. 394-407.
2. Cantwell, W.J. and J. Morton, *The impact resistance of composite materials — a review*. Composites, 1991. **22**(5): p. 347-362.
3. Nezhad, H.Y., et al., *Numerical analysis of low-velocity rigid-body impact response of composite panels*. International Journal of Crashworthiness, 2015. **20**(1): p. 27-43.
4. Camanho, P.P., et al., *Prediction of in situ strengths and matrix cracking in composites under transverse tension and in-plane shear*. Composites Part A: Applied Science and Manufacturing, 2006. **37**(2): p. 165-176.
5. Hernandez, T.P.A., A.R. Mills, and H. Yazdani Nezhad, *Shear driven deformation and damage mechanisms in High-performance carbon Fibre-reinforced thermoplastic and toughened thermoset composites subjected to high strain loading*. Composite Structures, 2021. **261**: p. 113289.
6. Alshammari, B.A., et al., *Comprehensive Review of the Properties and Modifications of Carbon Fiber-Reinforced Thermoplastic Composites*. Polymers, 2021. **13**(15): p. 2474.
7. Ratna, D. and A.K. Banthia, *Rubber toughened epoxy*. Macromolecular Research, 2004. **12**(1): p. 11-21.
8. Ma, J., et al., *Effect of inorganic nanoparticles on mechanical property, fracture toughness and toughening mechanism of two epoxy systems*. Polymer, 2008. **49**(16): p. 3510-3523.
9. Thostenson, E.T. and T.-W. Chou, *Processing-structure-multi-functional property relationship in carbon nanotube/epoxy composites*. Carbon, 2006. **44**(14): p. 3022-3029.
10. Egra, R., K. Janghorban, and H. Daneshmanesh, *Mechanical properties and toughening mechanisms of epoxy/graphene nanocomposites*. Journal of Polymer Engineering, 2015. **35**(3): p. 257-266.

11. Liu, T., et al., *Morphology and fracture behavior of intercalated epoxy/clay nanocomposites*. Journal of Applied Polymer Science, 2004. **94**(3): p. 1236-1244.
12. An, Q., A.N. Rider, and E.T. Thostenson, *Hierarchical Composite Structures Prepared by Electrophoretic Deposition of Carbon Nanotubes onto Glass Fibers*. ACS Applied Materials & Interfaces, 2013. **5**(6): p. 2022-2032.
13. Lin, M.-S., C.-C. Liu, and C.-T. Lee, *Toughened interpenetrating polymer network materials based on unsaturated polyester and epoxy*. Journal of Applied Polymer Science, 1999. **72**(4): p. 585-592.
14. Kinloch, A. and R.J. Young, *Fracture Behaviour of Polymer*. 1983.
15. Kinloch, A.J., et al., *Deformation and fracture behaviour of a rubber-toughened epoxy: 1. Microstructure and fracture studies*. Polymer, 1983. **24**(10): p. 1341-1354.
16. Park, S.-J., F.-L. Jin, and C. Lee, *Preparation and physical properties of hollow glass microspheres-reinforced epoxy matrix resins*. Materials Science and Engineering: A, 2005. **402**(1): p. 335-340.
17. Wu, D.Y., S. Meure, and D. Solomon, *Self-healing polymeric materials: A review of recent developments*. Progress in Polymer Science, 2008. **33**(5): p. 479-522.
18. Low, I.M., *Effects of residual stresses on the failure micromechanisms in toughened epoxy systems*. Journal of Materials Science 1990. **25**(4).
19. Karger-Kocsis, J., et al., *Interphase Engineering with Nanofillers in Fiber-Reinforced Polymer Composites*. 2016, John Wiley & Sons, Inc. p. 71-101.
20. Garg, A.C. and Y.W. Mai, *FAILURE MECHANISMS IN TOUGHENED EPOXY-RESINS - A REVIEW*. Composites Science and Technology, 1988. **31**(3): p. 179-223.
21. Tsai, J.-L., B.-H. Huang, and Y.-L. Cheng, *Enhancing Fracture Toughness of Glass/Epoxy Composites by Using Rubber Particles Together with Silica Nanoparticles*. Journal of Composite Materials, 2009. **43**(25): p. 3107-3123.
22. Singh, R.P., M. Zhang, and D. Chan, *Toughening of a brittle thermosetting polymer: Effects of reinforcement particle size and volume fraction*. Journal of Materials Science, 2002. **37**(4): p. 781-788.
23. Liu, H. and L.C. Brinson, *Reinforcing efficiency of nanoparticles: A simple comparison for polymer nanocomposites*. Composites Science and Technology, 2008. **68**(6): p. 1502-1512.
24. Nezhad, H.Y. and V.K. Thakur, *Effect of Morphological Changes due to Increasing Carbon Nanoparticles Content on the Quasi-Static Mechanical Response of Epoxy Resin*. Polymers, 2018. **10**(10): p. 1106.
25. Bregar, T., et al., *Carbon nanotube embedded adhesives for real-time monitoring of adhesion failure in high performance adhesively bonded joints*. Scientific Reports, 2020. **10**(1): p. 16833.
26. Sprenger, S., *Epoxy resin composites with surface-modified silicon dioxide nanoparticles: A review*. Journal of Applied Polymer Science, 2013. **130**(3): p. 1421-1428.
27. Liu, K.W. and C.W. Macosko, *Can nanoparticle toughen fiber-reinforced thermosetting polymers?* Journal of Materials Science, 2019. **54**(6): p. 4471-4483.
28. Domun, N., et al., *Improving the fracture toughness and the strength of epoxy using nanomaterials - a review of the current status*. Nanoscale, 2015. **7**(23): p. 10294-10329.
29. Vahedi, V., P. Pasbakhsh, and S.-P. Chai, *Toward high performance epoxy/halloysite nanocomposites: New insights based on rheological, curing, and impact properties*. Materials & Design, 2015. **68**: p. 42-53.
30. Awaja, F., et al., *Cracks, microcracks and fracture in polymer structures: Formation, detection, autonomic repair*. Progress in Materials Science, 2016. **83**: p. 536-573.
31. Low, I.M., *Toughening of epoxies by thermal expansion mismatch*. Journal of Applied Polymer Science, 1990. **39**(3): p. 759-762.
32. Kim, N.H. and H.S. Kim, *Toughening method and mechanisms for thermosets*. Journal of Applied Polymer Science, 2005. **98**(4): p. 1663-1667.
33. EVANS, A.G. and A.H. HEUER, *REVIEW—Transformation Toughening in Ceramics: Martensitic Transformations in Crack-Tip Stress Fields*. Journal of the American Ceramic Society, 1980. **63**(5-6): p. 241-248.
34. Evans, A.G. and R.M. Cannon, *Overview no. 48: Toughening of brittle solids by martensitic transformations*. Acta Metallurgica, 1986. **34**(5): p. 761-800.
35. Damjanovic, D., *Contributions to the piezoelectric effect in ferroelectric single crystals and ceramics*. Journal of the American Ceramic Society, 2005. **88**(10): p. 2663-2676.
36. Gerber, P., et al., *Effects of reversible and irreversible ferroelectric switchings on the piezoelectric large-signal response of lead zirconate titanate thin films*. Journal of Applied Physics, 2005. **98**: p. 124101-124101.
37. Kingon, A.I. and S. Srinivasan, *Lead zirconate titanate thin films directly on copper electrodes for ferroelectric, dielectric and piezoelectric applications*. Nature Materials, 2005. **4**(3): p. 233-237.
38. Manbachi, A. and R.S.C. Cobbold, *Development and Application of Piezoelectric Materials for Ultrasound Generation and Detection*. Ultrasound, 2011. **19**(4): p. 187-196.
39. Forrester, W.F. and R.M. Hinde, *Crystal Structure of Barium Titanate*. Nature, 1945. **156**(3954): p. 177-177.
40. Devonshire, A.F., *CIX. Theory of barium titanate—Part II*. The London, Edinburgh, and Dublin Philosophical Magazine and Journal of Science, 2009. **42**(333): p. 1065-1079.

41. Xu, Y., *Ferroelectric materials and their applications*. 1991, Amsterdam; New York; New York, NY, USA: North-Holland ; Sole distributors for the USA and Canada, Elsevier Science Pub. Co.
42. Pramanick, A., et al., *Domains, Domain Walls and Defects in Perovskite Ferroelectric Oxides: A Review of Present Understanding and Recent Contributions*. *Critical Reviews in Solid State and Materials Sciences*, 2012. **37**(4): p. 243-275.
43. Dudhe, C.M., et al., *Study of 90 degrees and 180 degrees Nanodomains in BaTiO<sub>3</sub> Nanoparticles Using Transmission Electron Microscopy*. *Ferroelectrics*, 2014. **471**(1): p. 148-155.
44. Abel, S., et al., *Large Pockels effect in micro- and nanostructured barium titanate integrated on silicon*. *Nature Materials*, 2019. **18**(1): p. 42-47.
45. Jo, W., et al., *Giant electric-field-induced strains in lead-free ceramics for actuator applications - status and perspective*. *Journal of Electroceramics*, 2012. **29**(1): p. 71-93.
46. Jones J.L., N.J.C., Pramanick A., Daniels J.E., *Time-Resolved, Electric-Field-Induced Domain Switching and Strain in Ferroelectric Ceramics and Crystals*. In: Eckold G., Schober H., Nagler S. (eds) *Studying Kinetics with Neutrons*. *Springer Series in Solid-State Sciences*, vol 161. Springer, Berlin, Heidelberg. [https://doi.org/10.1007/978-3-642-03309-4\\_6](https://doi.org/10.1007/978-3-642-03309-4_6). 2009.
47. Gao, J.H., et al., *Recent Progress on BaTiO<sub>3</sub>-Based Piezoelectric Ceramics for Actuator Applications*. *Actuators*, 2017. **6**(3): p. 20.
48. Shen, Z.-Y. and J.-F. Li, *Enhancement of piezoelectric constant  $d_{33}$  in BaTiO<sub>3</sub> ceramics due to nano-domain structure*. *Journal of the Ceramic Society of Japan*, 2010. **118**(1382): p. 940-943.
49. Ren, X.B., *Large electric-field-induced strain in ferroelectric crystals by point-defect-mediated reversible domain switching*. *Nature Materials*, 2004. **3**(2): p. 91-94.
50. Hsiang, H.I. and F.S. Yen, *Effect of crystallite size on the ferroelectric domain growth of ultrafine BaTiO<sub>3</sub> powders*. *Journal of the American Ceramic Society*, 1996. **79**(4): p. 1053-1060.
51. Polotai, A.V., A.V. Ragulya, and C.A. Randall, *Preparation and Size Effect in Pure Nanocrystalline Barium Titanate Ceramics*. *Ferroelectrics*, 2003. **288**(1): p. 93-102.
52. Jacob, J., L.H.L. Chia, and F.Y.C. Boey, *Thermal and non-thermal interaction of microwave radiation with materials*. *Journal of Materials Science*, 1995. **30**(21): p. 5321-5327.
53. Eugene, M.G.W.W.L., *Introduction to Microwaves*, in *Microwaves and Metals*. 2007. p. 1-23.
54. M Green, X.Z., *Recent progress of nanomaterials for microwave absorption*. *Journal of Materiomics*, 2019. **5**(4): p. 503-541.
55. Pertsev, N.A. and G. Arlt, *FORCED TRANSLATIONAL VIBRATIONS OF 90-DEGREES DOMAIN-WALLS AND THE DIELECTRIC-DISPERSION IN FERROELECTRIC CERAMICS*. *Journal of Applied Physics*, 1993. **74**(6): p. 4105-4112.
56. Ma, L. and A.M. Korsunsky, *The principle of equivalent eigenstrain for inhomogeneous inclusion problems*. *International Journal of Solids and Structures*, 2014. **51**(25): p. 4477-4484.
57. Arlt, G., *TWINNING IN FERROELECTRIC AND FERROELASTIC CERAMICS - STRESS RELIEF*. *Journal of Materials Science*, 1990. **25**(6): p. 2655-2666.
58. Nechaev, V.N. and A.M. Roschupkin, *On the generalized expression of the configuration force acting on the interfaces and domain boundaries in ferroelectric polycrystals*. *Ferroelectrics*, 1989. **90**(1): p. 29-34.
59. Pertsev, N.A. and G. Arlt, *INTERNAL-STRESSES AND ELASTIC ENERGY IN FERROELECTRIC AND FERROELASTIC CERAMICS - CALCULATIONS BY THE DISLOCATION METHOD*. *Ferroelectrics*, 1991. **123**(1-2): p. 27-44.
60. Arlt, G. and N.A. Pertsev, *FORCE-CONSTANT AND EFFECTIVE MASS OF 90-DEGREES DOMAIN-WALLS IN FERROELECTRIC CERAMICS*. *Journal of Applied Physics*, 1991. **70**(4): p. 2283-2289.
61. Arlt, G., U. Bottger, and S. Witte, *EMISSION OF GHZ SHEAR-WAVES BY FERROELASTIC DOMAIN-WALLS IN FERROELECTRICS*. *Applied Physics Letters*, 1993. **63**(5): p. 602-604.
62. deWit, R., *Theory of Disclinations: II. Continuous and Discrete Disclinations in Anisotropic Elasticity*. *J Res Natl Bur Stand A Phys Chem*, 1973. **77a**(1): p. 49-100.
63. Lifshitz, E.M., A.M. Kosevich, and L.P. Pitaevskii, *CHAPTER IV - DISLOCATIONS*††This chapter was written jointly with A. M. Kosevich, in *Theory of Elasticity (Third Edition)*, E.M. Lifshitz, A.M. Kosevich, and L.P. Pitaevskii, Editors. 1986, Butterworth-Heinemann: Oxford. p. 108-132.
64. Eshelby, J.D., *The Determination of the Elastic Field of an Ellipsoidal Inclusion, and Related Problems*. *Proceedings of the Royal Society of London Series A*, 1957. **241**: p. 376.
65. Eshelby, J.D. and R.E. Peierls, *The elastic field outside an ellipsoidal inclusion*. *Proceedings of the Royal Society of London. Series A. Mathematical and Physical Sciences*, 1959. **252**(1271): p. 561-569.
66. Sharma, S.C., *Effect of albite particles on the coefficient of thermal expansion behavior of the Al6061 alloy composites*. *Metallurgical and Materials Transactions A*, 2000. **31**(3): p. 773-780.
67. Meng, C. and D. Pollard, *Eshelby's solutions for ellipsoidal inclusion/heterogeneity with applications to localize*. *AGU Fall Meeting Abstracts*, 2011: p. 2428.
68. Mason, W.P., *Micromechanics of Defects in Solids*, by Toshio Mura. *The Journal of the Acoustical Society of America*, 1983. **73**(6): p. 2237-2237.

69. Module 3 Constitutive Equations  
[http://web.mit.edu/16.20/homepage/3\\_Constitutive/Constitutive\\_files/module\\_3\\_with\\_solutions.pdf](http://web.mit.edu/16.20/homepage/3_Constitutive/Constitutive_files/module_3_with_solutions.pdf).
70. Arlt, G., U. Bottger, and S. Witte, *DIELECTRIC DISPERSION OF FERROELECTRIC CERAMICS AND SINGLE-CRYSTALS AT MICROWAVE-FREQUENCIES*. Annalen Der Physik, 1994. **3**(7-8): p. 578-588.
71. Powles, J.G., *Dielectric Properties of Titanates at Ultra-high Frequencies*. Nature, 1948. **162**(4120): p. 614-614.
72. Chen, X., et al., *Electromagnetic characteristics of barium titanate/epoxide resin composites in X and Ku bands*. Journal of Alloys and Compounds, 2008. **453**(1): p. 433-436.
73. Bur, A.J., *Dielectric properties of polymers at microwave frequencies: a review*. Polymer, 1985. **26**(7): p. 963-977.
74. Vadivambal, R. and D.S. Jayas, *Non-uniform Temperature Distribution During Microwave Heating of Food Materials—A Review*. Food and Bioprocess Technology, 2010. **3**(2): p. 161-171.
75. Dibben, D., *Electromagnetics: fundamental aspects and numerical modeling*. Handbook of Microwave Technology for Food Applications, 2001: p. 1-28.
76. Saltiel, C. and A.K. Datta, *Heat and Mass Transfer in Microwave Processing*, in *Advances in Heat Transfer*, J.P. Hartnett, et al., Editors. 1999, Elsevier. p. 1-94.
77. Ayappa, K.G., et al., *Analysis of microwave heating of materials with temperature-dependent properties*. AIChE Journal, 1991. **37**(3): p. 313-322.
78. Mishra, R.R. and A.K. Sharma, *Microwave-material interaction phenomena: Heating mechanisms, challenges and opportunities in material processing*. Composites Part a-Applied Science and Manufacturing, 2016. **81**: p. 78-97.
79. Mgbemena, C.O., et al., *Accelerated microwave curing of fibre-reinforced thermoset polymer composites for structural applications: A review of scientific challenges*. Composites Part A: Applied Science and Manufacturing, 2018. **115**: p. 88-103.
80. Sharma, B., et al., *Microwave-Assisted Rapid Synthesis of Reduced Graphene Oxide-Based Gum Tragacanth Hydrogel Nanocomposite for Heavy Metal Ions Adsorption*. Nanomaterials, 2020. **10**(8): p. 1616.
81. Sanny, S.J.L.W.M.J., *OpenStax University Physics, University Physics Volume 2* Vol. 2. June 2019: OpenStax CNX <http://cnx.org/contents/7a0f9770-1c44-4acd-9920-1cd9a99f2a1e@16.7>.
82. Luo, J., *Analyses of Multimode Forming Process in a Microwave-heating Cavity*. Piers Online, 2007. **3**: p. 801-807.
83. Fu, Y.-C., et al., *An apparatus for on-line measuring electric field intensity during microwave heating: a theoretical consideration*. International Journal of Food Science & Technology, 2005. **40**(7): p. 743-757.
84. Lorrain, P.C.D.R., *Electromagnetic fields and waves*. 1970, San Francisco: W.H. Freeman.
85. Cheng, D.K., *Field and wave electromagnetics*. 1983, Reading, Mass.: Addison Wesley.
86. Balazs, A.C., T. Emrick, and T.P. Russell, *Nanoparticle polymer composites: Where two small worlds meet*. Science, 2006. **314**(5802): p. 1107-1110.
87. Lijima, M., et al., *Surface modification of BaTiO<sub>3</sub> particles by silane coupling agents in different solvents and their effect on dielectric properties of BaTiO<sub>3</sub>/epoxy composites*. Colloids and Surfaces a-Physicochemical and Engineering Aspects, 2009. **352**(1-3): p. 88-93.
88. US Research Nanomaterials, I. <https://www.us-nano.com/inc/sdetail/403>. 2020.
89. Patsidis, A.C. and G.C. Psarras, *Structural transition, dielectric properties and functionality in epoxy resin—barium titanate nanocomposites*. Smart Materials and Structures, 2013. **22**(11): p. 115006.
90. Zhou, T., et al., *Improving Dielectric Properties of BaTiO<sub>3</sub>/Ferroelectric Polymer Composites by Employing Surface Hydroxylated BaTiO<sub>3</sub> Nanoparticles*. Acs Applied Materials & Interfaces, 2011. **3**(7): p. 2184-2188.
91. UK, F.S., <https://www.fishersci.co.uk/shop/products/hydrogen-peroxide-30-water-fisher-bioreagents/10386643#?keyword=hydrogen+peroxide>. 2021.
92. Ambrożewicz, D., et al., *Fluoroalkylsilane versus Alkylsilane as Hydrophobic Agents for Silica and Silicates*. Journal of Nanomaterials, 2013. **2013**: p. 631938.
93. UK, F.S. <https://www.fishersci.co.uk/shop/products/ethanol-absolute-200-proof-molecular-biology-grade-fisher-bioreagents-5/16606002>. 2021.
94. Phan, T.T.M., et al., *Enhancement of polarization property of silane-modified BaTiO<sub>3</sub> nanoparticles and its effect in increasing dielectric property of epoxy/BaTiO<sub>3</sub> nanocomposites*. Journal of Science-Advanced Materials and Devices, 2016. **1**(1): p. 90-97.
95. Sundar, U., Z.C. Lao, and K. Cook-Chennault, *Enhanced Dielectric Permittivity of Optimized Surface Modified of Barium Titanate Nanocomposites*. Polymers, 2020. **12**(4): p. 26.
96. Sideridou, I.D. and M.M. Karabela, *Effect of the amount of 3-methacryloxypropyltrimethoxysilane coupling agent on physical properties of dental resin nanocomposites*. Dental Materials, 2009. **25**(11): p. 1315-1324.
97. Saeed, K., et al., *Planar Microwave Sensors for Complex Permittivity Characterization of Materials and Their Applications*. 2012.
98. Rovensky, T., et al. *Microstrip methods for measurement of dielectric properties in High Frequency area*. in *2015 38th International Spring Seminar on Electronics Technology (ISSE)*. 2015.

99. Bansal, P., E. Vineyard, and O. Abdelaziz, *Advances in household appliances- A review*. Applied Thermal Engineering, 2011. **31**(17): p. 3748-3760.
100. Lin, C.-Y., et al., *Preparation and characterization of organosoluble polyimide/BaTiO<sub>3</sub> composite films with mechanical- and chemical-treated ceramic fillers*. Polymer Journal, 2012. **44**(11): p. 1131-1137.
101. Tomer, V., et al., *Epoxy-based nanocomposites for electrical energy storage. I: Effects of montmorillonite and barium titanate nanofillers*. Journal of Applied Physics, 2010. **108**: p. 074116.
102. K.Dusek, *Epoxy Resins and Composites III*. Advances in Polymer Science. 1986, Berlin: Springer-Verlag Berlin Heidelberg. 166.
103. Pan, Y., et al., *Hybrid Network Structure and Mechanical Properties of Rodlike Silicate/Cyanate Ester Nanocomposites*. Macromolecules, 2008. **41**(23): p. 9245-9258.
104. Zhang, X., et al., *Polyaniline stabilized barium titanate nanoparticles reinforced epoxy nanocomposites with high dielectric permittivity and reduced flammability*. Journal of Materials Chemistry C, 2013. **1**(16): p. 2886-2899.
105. Sun, Y., et al., *Glass transition and relaxation behavior of epoxy nanocomposites*. Journal of Polymer Science Part B: Polymer Physics, 2004. **42**(21): p. 3849-3858.
106. Tian, L.H., et al., *Effect of hydrogenation on the microwave absorption properties of BaTiO<sub>3</sub> nanoparticles*. Journal of Materials Chemistry A, 2015. **3**(23): p. 12550-12556.
107. Cheng, K.C., et al., *Dielectric properties of epoxy resin-barium titanate composites at high frequency*. Materials Letters, 2007. **61**(3): p. 757-760.
108. Ramajo, L., M.S. Castro, and M.M. Reboredo, *Effect of silane as coupling agent on the dielectric properties of BaTiO<sub>3</sub>-epoxy composites*. Composites Part a-Applied Science and Manufacturing, 2007. **38**(8): p. 1852-1859.
109. Popielarz, R., et al., *Dielectric properties of polymer/ferroelectric ceramic composites from 100 Hz to 10 GHz*. Macromolecules, 2001. **34**(17): p. 5910-5915.
110. Schulze, G.J., F. *Ferroelectric Crystals*. ZAMM - Journal of Applied Mathematics and Mechanics / Zeitschrift für Angewandte Mathematik und Mechanik, 1963. **43**(10-11): p. 512-512.
111. Yang, W.H., et al., *A systematic study on electrical properties of the BaTiO<sub>3</sub>-epoxy composite with different sized BaTiO<sub>3</sub> as fillers*. Journal of Alloys and Compounds, 2015. **620**: p. 315-323.
112. Chen, R.-C., et al., *Chemically bonding BaTiO<sub>3</sub> nanoparticles in highly filled polymer nanocomposites for greatly enhanced dielectric properties*. Journal of Materials Chemistry C, 2020. **8**(26): p. 8786-8795.
113. Wendel, L., *Dielectric Measurements at GHz Frequencies*. 2019: Universitätsbibliothek der Universität Stuttgart.
114. Huang, X., et al., *Polyethylene/aluminum nanocomposites: Improvement of dielectric strength by nanoparticle surface modification*. Journal of Applied Polymer Science, 2009. **113**(6): p. 3577-3584.
115. Kok, L.P., M.E. Boon, and H.M. Smid, *The problem of hot spots in microwave equipment used for preparatory techniques—Theory and practice*. Scanning, 1993. **15**(2): p. 100-109.
116. Sun, J., W.L. Wang, and Q.Y. Yue, *Review on Microwave-Matter Interaction Fundamentals and Efficient Microwave-Associated Heating Strategies*. Materials, 2016. **9**(4).
117. Kreuzer, M., *Strain Measurement with Fiber Bragg Grating Sensors*. 2006.
118. Her, S.-C. and C.-Y. Huang, *Thermal Strain Analysis of Optic Fiber Sensors*. Sensors, 2013. **13**(2): p. 1846-1855.
119. Rajesh, S., et al., *Microwave dielectric properties of PTFE/rutile nanocomposites*. Journal of Alloys and Compounds, 2009. **477**(1): p. 677-682.
120. Kirby, R.K., *Thermal Expansion of Polytetrafluoroethylene (Teflon) From - 1900 to +3000 C* Journal of Research of the National Bureau of Standards, 1956. **57**(2): p. Research paper 2696.
121. *PERMABOND® 920 Cyanoacrylate Technical Datasheet, PQCY00035-tds*, P.E. Adhesives, Editor. 2016.
122. Khaleque, T., et al., *Tailoring of Thermo-Mechanical Properties of Hybrid Composite-Metal Bonded Joints*. Polymers, 2021. **13**(2).
123. Chen, X.D., et al., *Microwave absorption properties of barium titanate/epoxide resin composites*. Journal of Physics D-Applied Physics, 2007. **40**(6): p. 1827-1830.
124. Baek, K., et al., *Axial oxygen vacancy-regulated microwave absorption in micron-sized tetragonal BaTiO<sub>3</sub> particles*. Journal of Materials Chemistry C, 2018. **6**(36): p. 9749-9755.
125. Siniscalco, D., et al., *Functionalization of Hydroxyapatite Ceramics: Raman Mapping Investigation of Silanization*. Ceramics, 2019. **2**(2): p. 372-384.
126. Maiwa, H., *12 - Thermal energy harvesting of PLZT and BaTiO<sub>3</sub> ceramics using pyroelectric effects*, in *Nanoscale Ferroelectric-Multiferroic Materials for Energy Harvesting Applications*, H. Kimura, Z. Cheng, and T. Jia, Editors. 2019, Elsevier. p. 217-229.
127. Dvorak, G.J., N. Laws, and M. Hejazi, *Analysis of Progressive Matrix Cracking in Composite Laminates I. Thermoelastic Properties of a Ply with Cracks*. Journal of Composite Materials, 1985. **19**(3): p. 216-234.
128. Talreja, R., *Transverse Cracking and Stiffness Reduction in Composite Laminates*. Journal of Composite Materials, 1985. **19**(4): p. 355-375.

129. Smith, P.A. and J. Wood, *Poisson's Ratio as a Damage Parameter in the Static Tensile Loading of Simple Crossply Laminates*. Composites Science and Technology - COMPOSITES SCI TECHNOL, 1990. **38**: p. 85-93.
130. Bowles, D.E., *Effect of Microcracks on the Thermal Expansion of Composite Laminates*. Journal of Composite Materials, 1984. **18**(2): p. 173-187.
131. Lim, S.G. and C.S. Hong, *Effect of transverse cracks on the thermomechanical properties of cross-ply laminated composites*. Composites Science and Technology, 1989. **34**(2): p. 145-162.
132. Hashin, Z., *Thermal expansion coefficients of cracked laminates*. Composites Science and Technology, 1988. **31**(4): p. 247-260.
133. Herakovich, C.T. and M.W. Hyer, *Damage-induced property changes in composites subjected to cyclic thermal loading*. Engineering Fracture Mechanics, 1986. **25**(5): p. 779-791.
134. Camahort, J.L., E.H. Rennhack, and W.C. Coons, *Effects of Thermal Cycling Environment on Graphite/Epoxy Composites*, J.L. Christian and B.A. Stein, Editors. 1976, ASTM International: West Conshohocken, PA. p. 37-49.
135. Feltham, S.J., B. Yates, and R.J. Martin, *The thermal expansion of particulate-reinforced composites*. Journal of Materials Science, 1982. **17**(8): p. 2309-2323.
136. Zhang, J., et al., *Effect of nanoparticles on interfacial properties of carbon fibre-epoxy composites*. Composites Part A: Applied Science and Manufacturing, 2013. **55**: p. 35-44.
137. Patterson, A.L., *The Scherrer Formula for X-Ray Particle Size Determination*. Physical Review, 1939. **56**(10): p. 978-982.
138. Steyn-Ross, A. and A. Riddell, *Standing waves in a microwave oven*. The Physics Teacher, 1990. **28**: p. 474.
139. Kamol, S., P. Limsuwan, and W. Onreabroy, *Three-dimensional standing waves in a microwave oven*. American Journal of Physics, 2010. **78**(5): p. 492-495.
140. Lincoln, J., *An improved technique for visualizing microwave wavelengths in microwave ovens*. The Physics Teacher, 2019. **57**(4): p. 271-271.
141. Zheng, P., et al., *Grain-size effects on dielectric and piezoelectric properties of poled BaTiO<sub>3</sub> ceramics*. Acta Materialia, 2012. **60**(13): p. 5022-5030.
142. Lei, Z., et al., *An Experimental Analysis of Residual Stress Measurements in Porous Silicon Using Micro-Raman Spectroscopy*. Chinese Physics Letters, 2004. **21**: p. 403.